

UNCLASSIFIED

AD NUMBER

ADB015279

LIMITATION CHANGES

TO:

Approved for public release; distribution is unlimited.

FROM:

Distribution authorized to U.S. Gov't. agencies only; Test and Evaluation; SEP 1976. Other requests shall be referred to Rome Air Development Center, Griffiss AFB, NY.

AUTHORITY

RADC ltr 3 May 1979

THIS PAGE IS UNCLASSIFIED

THIS REPORT HAS BEEN DELIMITED
AND CLEARED FOR PUBLIC RELEASE
UNDER DOD DIRECTIVE 5200.20 AND
NO RESTRICTIONS ARE IMPOSED UPON
ITS USE AND DISCLOSURE.

DISTRIBUTION STATEMENT A

APPROVED FOR PUBLIC RELEASE;
DISTRIBUTION UNLIMITED.

✓
RADC-TR-76-298
Final Technical Report
September 1976



(2)

ADBO15279

FLOW PROPERTIES IN THE NEAR WAKE OF HYPERSONIC
VEHICLES AT LOW ALTITUDES

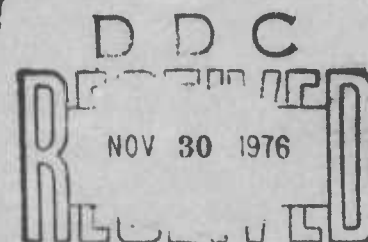
TRW

Defense and Space Systems Group

Distribution limited to U.S. Government agencies only;
Test and Evaluation. September 1976. Other requests
for this document must be referred to RADC/ETEP Hanscom
AFB MA 01731

AD No.
DDC FILE COPY.

ROME AIR DEVELOPMENT CENTER
AIR FORCE SYSTEMS COMMAND
GRIFFISS AIR FORCE BASE NEW YORK 13441



B

"Flow Properties in the Near Wake of Hypersonic Vehicles of Low Altitudes"

Dr. J. T. Ohrenberger is the principal investigator for this contract. John F. Lennon (ETEP) is the RADC Project Engineer.

This report is unclassified and the data presented from classified documents is unclassified consistent with Ballistic Missile Defense Master Plan, General Note on Research Data, Discrimination Sections 1-0 and 1-5. Questions regarding this classification are directed to Mr. M. Hawie, Discrimination Directorate U. S. Army Ballistic Missile Defense Advanced Technology Center, Huntsville, Alabama.

This technical report has been reviewed and approved for publication.

APPROVED:

John F. Lennon
JOHN F. LENNON

Contract Monitor

Microwave Detection Techniques Br.

Electromagnetic Sciences Division

APPROVED:

Allan C. Schell

ALLAN C. SCHELL

Acting Chief

Electromagnetic Sciences Division

FOR THE COMMANDER:

John P. Huss

Plans Office

ADDITIONAL TO	
HTIS	Wallo Section <input type="checkbox"/>
ONE	Self Section <input checked="" type="checkbox"/>
ORAL SURGEON	<input type="checkbox"/>
JUSTIFICATION	
BY	
DISTRIBUTION/AVAILABILITY CODES	
Dist.	AVAIL. AND/OR SPECIAL
B	

unclassified

SECURITY CLASSIFICATION OF THIS PAGE (When Data Entered)

REPORT DOCUMENTATION PAGE		READ INSTRUCTIONS BEFORE COMPLETING FORM	
1. REPORT NUMBER RADC-TR-76-298 ✓	2. GOVT ACCESSION NO.	3. RECIPIENT'S CATALOG NUMBER	
4. TITLE (and Subtitle) FLOW PROPERTIES IN THE NEAR WAKE OF HYPERSONIC VEHICLES AT LOW ALTITUDES.	5. TYPE OF REPORT & PERIOD COVERED Final Report, May 1975- Sept 1976		
6. AUTHOR(s) J. T. Ohrenberger Principal Investigator	7. PERFORMING ORG. REPORT NUMBER TRW-27816-6001-RU-00	8. CONTRACT OR GRANT NUMBER(s) F19628-75-C-0160 new	
9. PERFORMING ORGANIZATION NAME AND ADDRESS TRW - 1 Space Park, Redondo Beach, California 90278	10. PROGRAM ELEMENT, PROJECT, TASK AREA & WORK UNIT NUMBERS 61102F 21530101		
11. CONTROLLING OFFICE NAME AND ADDRESS Deputy for Electronic Technology (RADC/ETEP) Hanscom Air Force Base, Massachusetts 01731 Monitor/John Lennon/ETEP	12. REPORT DATE September 1976		
13. MONITORING AGENCY NAME & ADDRESS (if different from Controlling Office) (12) 132p.	14. SECURITY CLASS. (of this report) unclassified		
15a. DECLASSIFICATION/DOWNGRADING SCHEDULE			
16. DISTRIBUTION STATEMENT (of this Report) Distribution limited to U.S. Government Agencies only; Test & Evaluation. September 1976. Other requests for this document must be referred to RADC/ETEP Hanscom Air Force Base, Massachusetts 01731.			
17. DISTRIBUTION STATEMENT (of the abstract entered in Block 20, if different from Report) Approved for public release; distribution unlimited.			
18. SUPPLEMENTARY NOTES			
19. KEY WORDS (Continue on reverse side if necessary and identify by block number) Hypersonic Flow Turbulent Boundary Layer Turbulent Near Wake Electromagnetic Flow Properties			
20. ABSTRACT (Continue on reverse side if necessary and identify by block number) See next page			

DD FORM 1 JAN 73 1473

EDITION OF 1 NOV 65 IS OBSOLETE

unclassified

SECURITY CLASSIFICATION OF THIS PAGE (When Data Entered)

409637

LB

20.

ABSTRACT

The boundary layer and near base region of three reentry vehicles were calculated under conditions of a turbulent boundary layer and wake. Flow properties affecting the transmission of electromagnetic signals from the base region are presented and include predictions of the charged particle densities and collision frequencies. The possible simulation of a full scale vehicle by a vehicle of smaller size whose heatshield is intentionally seeded with "low ionization potential" materials is investigated and found to be feasible within reasonable engineering limits.

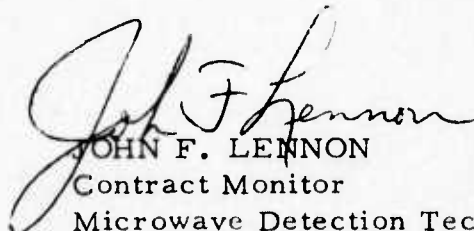
Reentry heating and detailed boundary layer analyses were performed to establish the fluid profiles at the aft station of the vehicles. Boundary layer separation and the near wake flowfield was determined by a self-consistent viscous-inviscid interaction theory. A single non-equilibrium reaction was used to determine the electron concentration profiles above the recirculation region, while equilibrium thermodynamics was applied to determine the neutral and charged species concentrations in the recirculation region.

To assist in evaluating the accuracy of the modeling, similar calculations were performed for a vehicle in which flight measurements of several flow properties were made in the base region during reentry. Favorable agreement with the data was achieved by the analysis.

EVALUATION

This report is the Final Report of Contract F19628-75-C-0160 covering the period May 1975 to September 1976. Low altitude flow properties in the near wake region of hypersonic, slender cones of varying bluntness were calculated. The purpose of this effort was twofold. First the results for an RMV-340 type vehicle were compared to flight test data to provide some understanding of the level of accuracy of the analysis. The primary objective was to compare the flow properties of the full scale vehicle to those of a smaller one with selected levels of easily ionized material seeded in its heat shield, thereby determining whether the seeding technique could simulate full scale electrical wake properties. This work was originally intended to support Task 215301, Interaction of Microwave Radiators in Ionized Flow Fields, in particular, the studies based on the proposal that full scale flight testing programs by SAMSO/ABRES could be supplemented by less expensive tests using smaller, ground-or plane-launched vehicles with seeded heatshields. No additional work in this area is currently under consideration at RADC/ET.

The results tend to indicate that, by appropriate selection of seedant levels, a suitable range of electrical characteristics can be produced in the near wake for testing base mounted antennas. In addition, the calculations for the flight test comparisons may have applications to the continuing research program of the U.S. Army Ballistic Missile Defense Systems Command.



JOHN F. LENNON

Contract Monitor

Microwave Detection Techniques Br.
Electromagnetic Sciences Division

ACKNOWLEDGMENTS

The present report summarizes an application of a turbulent near wake flowfield modeling and associated computer programs developed for the U.S. Army Ballistic Missile Defense Systems Command - Ballistic Missile Defense Advanced Technology Center, Huntsville, Alabama under contract DASG60-76-C-0043.

Additional TRW personnel who technically supported the present study are listed below.

Reentry Heating: Mr. A. J. Steinberger
Boundary Layer Analysis: Mr. A. V. Gomez
Chemical Kinetics: Dr. E. Fishman
Collision Frequency: Mr. H. E. Wohlwill
Computer Analysis Support: Mrs. E. Kampe

TABLE OF CONTENTS

	<u>Page</u>
1. INTRODUCTION	1
2. CONFIGURATIONS AND TRAJECTORIES	2
3. REENTRY HEATING AND ABLATION ANALYSIS	7
3.1 RESULTS OF THE HEATING/ABLATION ANALYSIS	8
4. ELECTRON SOURCES AND CHEMICAL EQUILIBRATION IN COMBUSTING BOUNDARY LAYERS	18
4.1 AFT SHOULDER BOUNDARY LAYER PROPERTIES	21
4.1.1 Full Scale Vehicle Boundary Layer	25
4.1.2 Small Vehicle Boundary Layer	25
5. SHOULDER SEPARATION AND NEAR WAKE ANALYSIS	41
5.1 TURBULENCE MODELING THEORY	47
5.2 IMPOSED CONDITIONS AND WAKE SOLUTION SUMMARY	48
6. WAKE PLASMA ANALYSIS	51
6.1 OUTER WAKE PLASMA EQUATIONS	52
6.2 RECIRCULATION REGION COMPOSITION	54
6.3 COLLISION FREQUENCY	56
7. WAKE FLUID MECHANICS AND PLASMA RESULTS	57
7.1 FULL SCALE VEHICLE WAKE RESULTS	57
7.2 SMALL VEHICLE WAKE RESULTS	58
7.3 RECIRCULATION REGION ELECTRON CONCENTRATIONS	59
8. COMPARISONS WITH FLIGHT MEASUREMENTS	79
8.1 WAKE RESULTS FOR THE RMV-340 VEHICLES	79
8.2 FLIGHT MEASUREMENTS	80
9. CONCLUSIONS	89
REFERENCES	91
APPENDIX I: AEROHEATING, ABLATION, AND BOUNDARY LAYER ANALYSIS. .	93
APPENDIX II: NEAR WAKE FLOW MODEL	104
APPENDIX III: COLLISION FREQUENCY ESTIMATES	114

LIST OF ILLUSTRATIONS

<u>Figure</u>		<u>Page</u>
1	Full Scale and Small Vehicle Configurations	4
2	RMV-340 Configuration	5
3	Full Scale and Small Vehicle Trajectories	6
4	Reentry Heating and Ablation Analysis Procedures	9
5	Surface Integrated Mass Loss Histories	13
6	Frustum Surface Temperature Distributions	14
7	Frustum Mass Flux Distributions	15
8	Edge-of-Boundary Layer Velocity Distribution	16
9	Full Scale Vehicle - 5.92 km - Aft Station Velocity, Temperature and Density Profiles	27
10	Full Scale Vehicle - 5.92 km - Aft Station Charged Particle Profiles - Non-equilibrium Na Ionization	28
11	Full Scale Vehicle - 5.92 km - Aft Station Charged Particle Profiles - Equilibrium Na Ionization	29
12	Full Scale Vehicle - 4.58 km - Aft Station Velocity, Temperature, and Density Profiles	30
13	Full Scale Vehicle - 4.58 km - Aft Station Charged Particle Profiles - Non-equilibrium Na Ionization	31
14	Full Scale Vehicle - 4.58 km - Aft Station Charged Particle Profiles - Equilibrium Na Ionization	32
15	Full Scale Vehicle - 1.53 km - Aft Station Velocity, Temperature, and Density Profiles	33
16	Full Scale Vehicle - 1.53 km - Aft Station Charged Particle Profiles - Equilibrium Na Ionization	34
17	Small Vehicle - 6.16 km - Aft Station Velocity, Temperature, and Density Profiles	35
18	Small Vehicle - 6.16 km - Aft Station Charged Particle Profiles - Non-equilibrium Na Ionization	36
19	Small Vehicle - 6.16 km - Aft Station Charged Particle Profiles - Equilibrium Na Ionization	37

LIST OF ILLUSTRATION (Continued)

<u>Figure</u>		<u>Page</u>
20	Small Vehicle - 4.54 km - Aft Station Velocity, Temperature, and Density Profiles	38
21	Small Vehicle - 4.54 km - Aft Station Charged Particle Profiles - Non-equilibrium Na Ionization	39
22	Small Vehicle - 4.54 km - Aft Station Charged Particle - Equilibrium Na Ionization	40
23	Elements of the Near Wake Flowfield	42
24	Qualitative Behavior of the Near Wake Solution	44
25	Full Scale Vehicle - 5.92 km - Near Base Flowfield	61
26	Full Scale Vehicle - 5.92 km - Near Base Pressure Distributions	62
27	Full Scale Vehicle - 5.92 km - Near Base Temperature Distributions	63
28	Full Scale Vehicle - 5.92 km - Near Base Electron Density Distributions - Outer Flow Region	64
29	Full Scale Vehicle - 5.92 km - Near Base Collision Frequency Distributions	65
30	Full Scale Vehicle - 4.58 km - Near Base Flowfield	66
31	Full Scale Vehicle - 4.58 km - Near Base Electron Density Distributions - Outer Flow Region	67
32	Full Scale Vehicle - 4.58 km - Near Base Collision Frequency Distributions	68
33	Small Vehicle - 6.16 km - Near Base Flowfields	69
34	Small Vehicle - 6.16 km - Near Base Pressure Distributions	70
35	Small Vehicle - 6.16 km - Near Base Temperature Distributions	71
36	Small Vehicle - 6.16 km - Near Base Electron Density Distributions - Outer Flow Region	72
37	Small Vehicle - 6.16 km - Near Base Collision Frequency Distributions	73
38	Small Vehicle - 4.54 km - Near Base Flowfield	74
39	Small Vehicle - 4.54 km - Near Base Electron Density Distributions - Outer Flow Region	75

LIST OF ILLUSTRATIONS (Continued)

<u>Figure</u>		<u>Page</u>
40	Small Vehicle - 4.54 km - Near Base Collision Frequency Distributions	76
41	Recirculation Region Electron Density - 6 km Nominal Altitude - Full Scale and Small Vehicles	77
42	Recirculation Region Electron Density - 4.6 km Nominal Altitude - Full Scale and Small Vehicles	78
43	RMV-340 Vehicle - 25 km - Near Base Flowfield	82
44	RMV-340 Vehicle - 25 km - Near Base Pressure Distributions	83
45	RMV-340 Vehicle - 25 km - Near Base Temperature Distributions	84
46	RMV-340 - 25 km - Near Base Electron Density Distribution - Outer Flow Region	85
47	RMV-340 -- 25 km - Near Base Collision Frequency Distributions	86
48	RMV-340 Recirculation Region Ion Concentration -- Comparison of Prediction with Values Deduced from Flight Measurements	87
49	RMV-340 -- Comparison of Predicted Base Pressure with Flight Measurements	88

1. INTRODUCTION

A theoretical analysis of the boundary layer and near wake of three hypersonic slender vehicles of small and moderate bluntness have been performed corresponding to low altitude conditions where the boundary layer and wake are turbulent. Predictions are made of those properties of the flow in the base region, such as electron density and collision frequency distributions, which affect the transmission of electromagnetic signals from the base region.

A small scale vehicle and a full scale vehicle with carbon phenolic heatshields and graphite nose tips are analyzed at two altitudes under conditions of nominal alkali metal contamination (50 ppm equivalent Na). In addition, to explore the possibility of near base plasma simulation with the large vehicle, intentional seeding of the small vehicle heatshield is investigated. Seeding levels of 500 ppm and 1000 ppm equivalent Na are assumed. The heat transfer and ablation histories of the two vehicles during reentry are also calculated to provide the rate of mass loss and surface temperature distributions needed for the detailed boundary layer and wake calculations subsequently performed at the two altitudes of interest.

A third vehicle is analyzed which corresponds to an RMV-340 type vehicle with a silica phenolic heatshield and graphite nose tip. Analogous boundary layer and wake calculations are performed for this vehicle at one altitude. In order to provide some understanding of the level of accuracy of the analysis, a comparison of the predicted electron density levels in the base recirculation region and of the base pressure are made with existing flight measurements for this vehicle.

The ensuing sections will concentrate on the results of these analyses along with the appropriate input conditions and critical assumptions made. More detailed descriptions of the analyses are discussed in the Appendices, although for the most part these have been presented in the open literature.

2. CONFIGURATIONS AND TRAJECTORIES

The geometry of the spherically tipped conical vehicles analyzed here is presented in Figures 1 and 2. Geometrical specifics and material data are presented in Table 1 below.

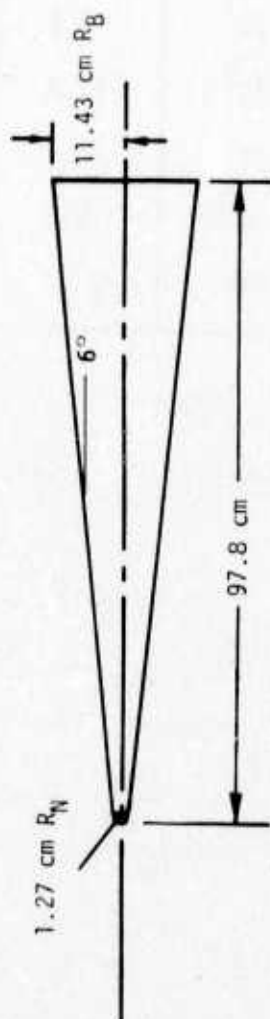
TABLE 1 VEHICLE CONFIGURATIONS			
Properties	Small Scale Vehicle	Full Scale Vehicle	RMV-340 Vehicle
Nose radius(R_N)	0.5 in/1.27 cm	2 in/5.08 cm	0.1 in/0.25 cm
Base radius(R_B)	4.5 in/11.43 cm	12 in/30.48 cm	24 in/61 cm
Length	38.5 in/97.8 cm	78.9 in/200.4 cm	170 in/432 cm
Bluntness Ratio (R_N/R_B)	0.11	0.17	0.004
Frustum Half Angle	6.0 degrees	7.4 degrees	8.0 degrees
Frustum Material	Carbon Phenolic	Carbon Phenolic	Silica Phenolic
Nose Material	ATJ-S Graphite	ATJ-S Graphite	ATJ-S Graphite
Equivalent Na Level on the Heatshield	50,500,1000 ppm	50 ppm	50 ppm [*]
* Alkali metal contamination measurements were made for the RMV-340 vehicle and are reported in Reference 1.			

The imposed flight trajectories of the small scale and full scale vehicles are presented in Figure 3. Beginning at about 20 kft the trajectories are nearly parallel with the small vehicle velocity running about 1000 ft/sec less than that of the full scale vehicle. The trajectory of the RMV-340 vehicle is not shown but is presented in Reference 2. Boundary layer and wake analyses were conducted for conditions corresponding to the 6 km and 4.6 km altitudes for the small and full scale vehicles and to the 25 km altitude for the RMV-340 vehicle. The actual flight conditions are summarized in Table 2 below.

TABLE 2 FLIGHT CONDITIONS ANALYZED				
	Altitude kft/km	Velocity kfps/kmps	Reynolds Number $\rho_{\infty} U_{\infty} 2R_B / \mu_{\infty}$	Mach Number U_{∞} / a_{∞}
Small Vehicle	20.2/6.16	12.3/3.75	3.5×10^7	11.9
	14.9/4.54	11.5/3.51	3.8×10^7	10.9
Full Scale Vehicle	19.4/5.92	14.2/4.32	1.1×10^8	13.7
	15.0/4.58	12.8/3.91	1.1×10^8	12.1
	5.0/1.53*	9.2/2.82	1.0×10^8	8.4
RMV-340	82/25	22.0/6.71	2.3×10^7	22.7

*Sodium ionization calculated by equilibrium chemistry only.

SMALL VEHICLE



FULL SCALE VEHICLE

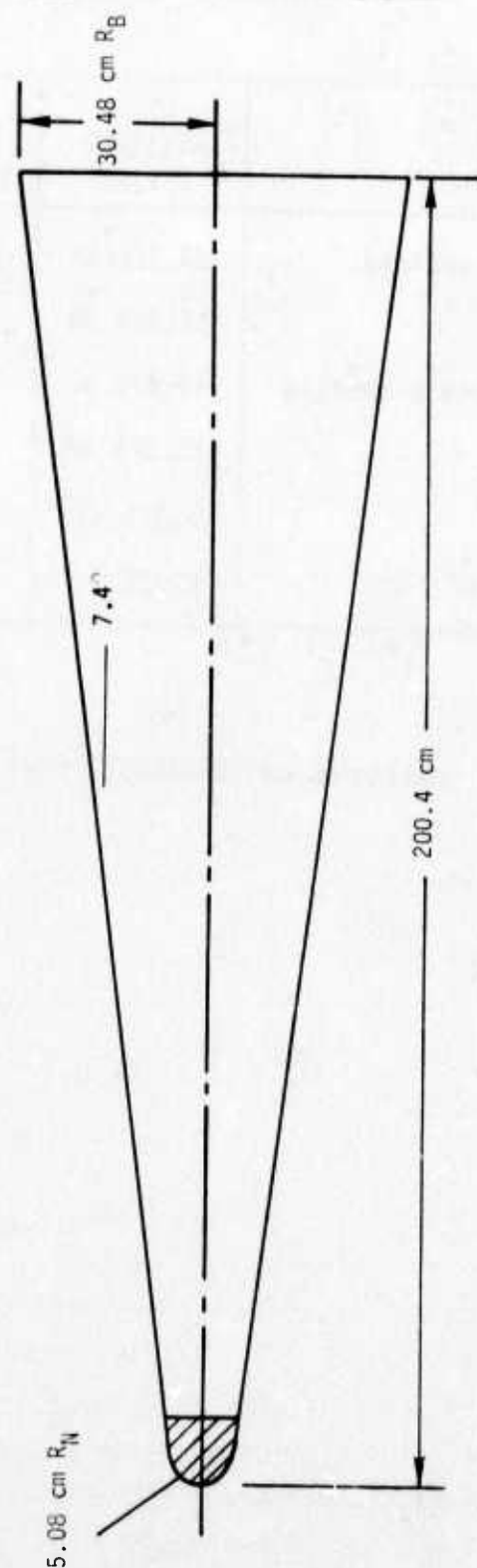


Figure 1. Full Scale and Small Vehicle Configurations

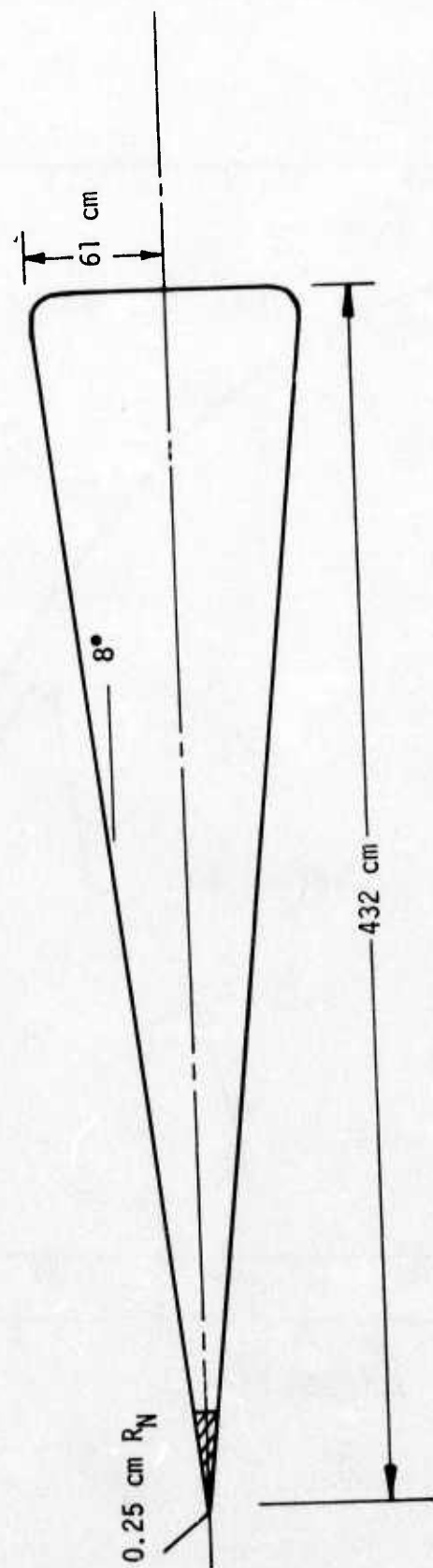


Figure 2. RMV-340 Configuration

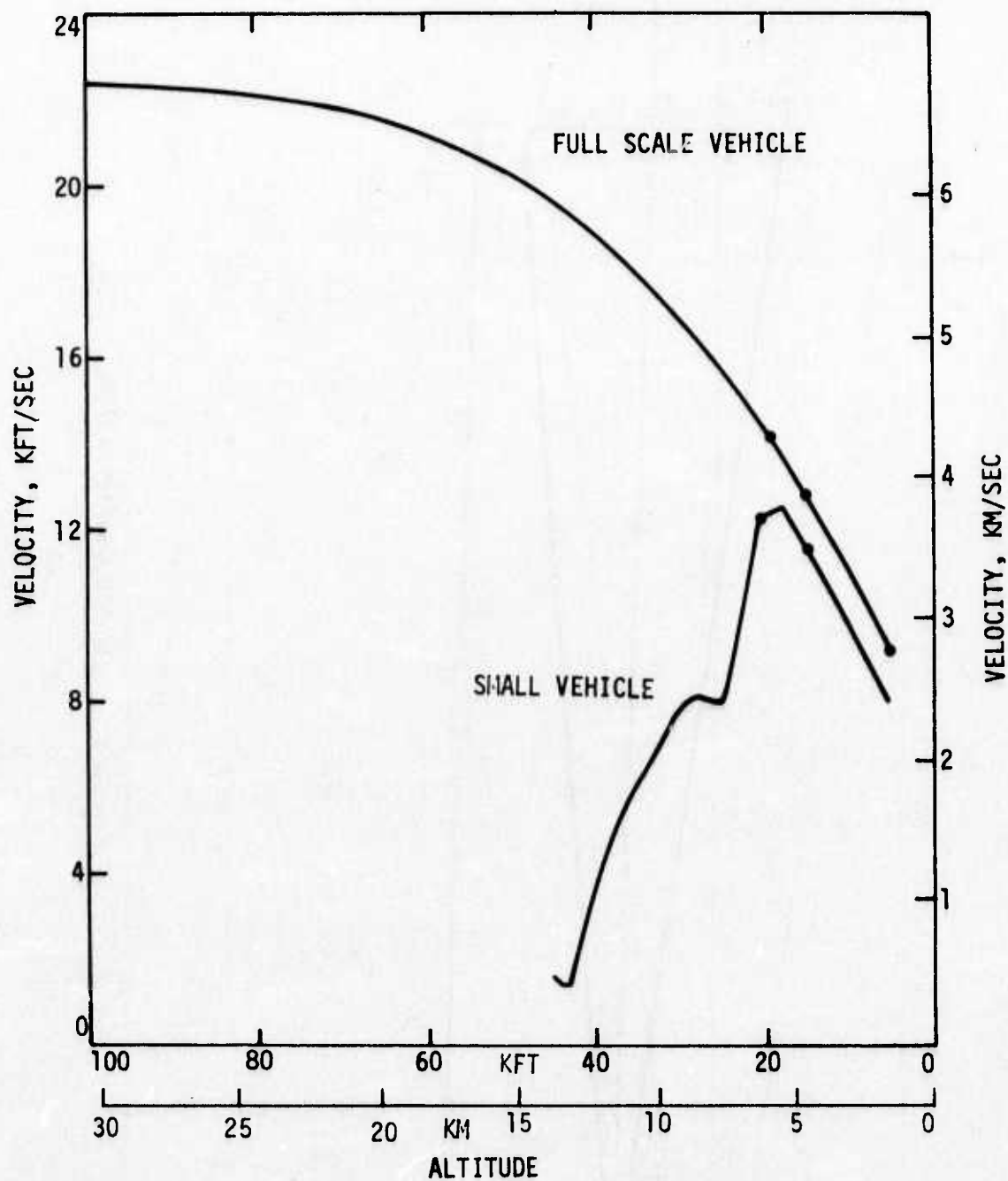


Figure 3. Full Scale and Small Vehicle Trajectories

3. REENTRY HEATING AND ABLATION ANALYSIS

The fluid mechanical and plasma properties of the near wake are strongly dependent on the fluid mechanical and chemical profiles occurring within the boundary layer at the aft station of the vehicle. Consequently, the detailed development of the boundary layer on the vehicle must be calculated to provide initial conditions for the subsequent wake calculation at the trajectory time points of interest. The analysis of the chemically reacting boundary layer utilizes a sophisticated computer code (KBLIMP) whose application requires knowledge of the surface state (wall temperature and ablation), vehicle shape, shock shape and boundary layer edge conditions. These parameters vary throughout the reentry trajectory as the vehicle responds to the changing reentry environment. Their determination necessarily requires an interactive calculation between boundary layer heating and surface heat absorption. Procedures followed in the present application are now described.

The reentry heating/vehicle response analysis consists of two parts. First, a no-blowing (no ablation) heating environment is calculated parametrically for various wall temperatures for the entire entry trajectory. This calculation is performed using engineering correlations for the shock shape and the boundary layer heating and skin friction. Entropy swallowing effects are accounted for by an integral matching of the mass flow in the boundary layer with that crossing the shock. Second, the ablation materials in-depth response at selected spatial points on the vehicle surface is calculated using the non-blown heating environment solutions. For low conductivity ablative materials, e.g., carbon-phenolic, graphite, etc., the in-depth material response can be modeled by one-dimensional analysis without a significant loss in accuracy relative to the computed vehicle shape change. The in-depth thermal conduction and virgin material decomposition are calculated numerically. The surface phenomena that include the surface chemistry, the heat blocking effect due to blowing, and the ablation fluxes are determined simultaneously. If excessive shape-change of the vehicle surface is computed, additional iterations on the non-blown heating environment solutions are performed.

An alternative and simpler procedure for obtaining accurate solutions for the R/V shape-change and wall temperatures in the nose region can be found under the steady-state ablation assumption, viz., the time-rate-of-change of the energy stored within the heatshield is considered negligible in comparison with the convective heating rate to the wall and corresponding energy loss due to radiation and ablation mass loss mechanisms. Generally this alternate method will predict higher wall temperatures and larger ablation loss rates than in the previous method where the in-depth thermal response is analyzed.

A schematic diagram of the calculations loop leading to a detailed boundary layer calculation is given in Figure 4. A capsule description of the computer programs employed is given in Table 3. The first two blocks in the main loop correspond to the approximate treatment and the third and final part corresponds to detailed boundary layer analysis. The iteration back-loop (dashed lines in Figure 4) represents the calculations path when excessive shape change is encountered. This loop was unnecessary in the present application to the small scale and full scale vehicles.

A more detailed description of each of the components of the aerodynamic heating and ablation analysis is presented in Appendix I.

3.1 RESULTS OF THE HEATING/ABLATION ANALYSIS

The surface integrated mass loss rate for the three vehicles is presented in Figure 5 as a function of altitude. Compared to the small vehicle, the full-scale vehicle displays considerably larger mass loss rates due to its larger size (about 6-times the surface area), larger velocities, and shallower entry angle. For the full scale vehicle, the onset of boundary layer transition was determined from the Martellucci³ correlation and found to be at 24.4 km. The forward movement of transition was determined using a Reynolds number - Mach number criterion established from Minuteman flight data but shifted so as to agree with the predicted onset altitude. Full turbulence on the frustum occurs slightly above 18 km. For the small vehicle, transition was found to begin at an axial station less than 11.5 cm from the tip at altitudes above 9 km, and at an axial station less than 1.2 cm from the tip at the lower altitudes.

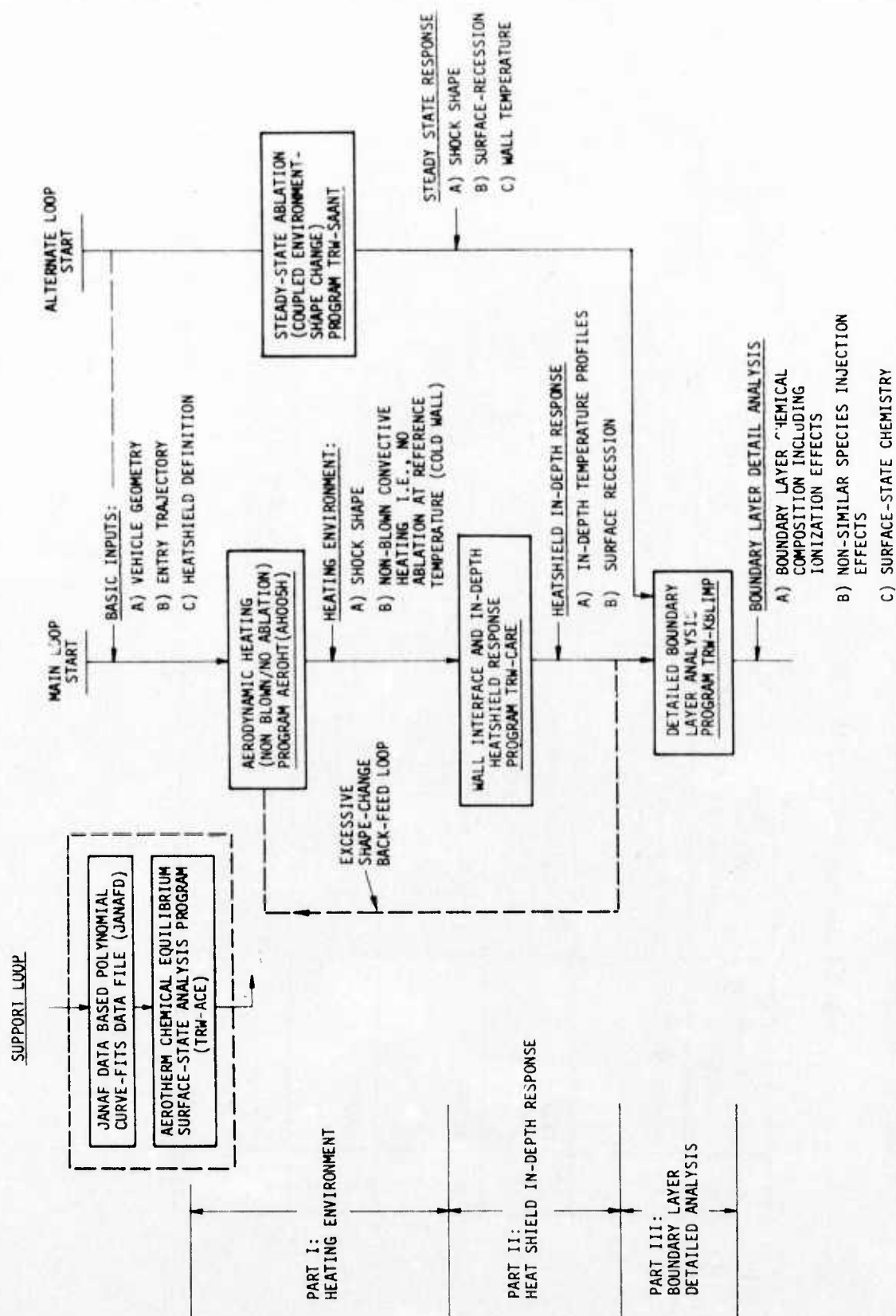


Figure 4. Keentry Heating and Ablation Analysis Procedures

TABLE 3
COMPUTER PROGRAMS EMPLOYED TO ANALYZE THE R/V HEATING AND ABLATION PERFORMANCE
A) 1-D IN-DEPTH RESPONSE COMPUTER PROGRAMS (MAIN LOOP)

ITEM NO.	PROGRAM NAME OR ACRONYM	PROGRAM TITLE OR CAPSULE DESCRIPTION	PROGRAM OBJECTIVES	FUNCTION LOOP
1	AH005H (AEROHT)	TRW Aerodynamic Surface Heating Program	Calculate non-blown (no ablation) heating environment, i.e., shock shape, convective heating and/or heating film coefficients	Main
2	CARE	TRW Coupled Conduction, Ablation, Reaction, and Erosion Program	Calculate in-depth response, i.e., in-depth temperatures, surface recession (shape change), etc.	Main
5	BLIMPK	Aerotherm Nonequilibrium Chemistry Boundary Layer Integral Matrix Procedure.	Calculate boundary layer detail chemical species composition (including ionization) with up to 7 non-equilibrium chemical species.	Main
6	JANAFD	JANAF Data Based Polynomial Curve-Fits Data File (1,100 Species)	Chemical species thermochemical properties data base.	Support Loop
7	ACE	Aerotherm Chemical Equilibrium Analysis Program.	Equilibrium Chemistry Surface-State, Open-System, analysis.	Support Loop

TABLE 3 (Continued)

B) STEADY-STATE ABLATION COMPUTER PROGRAM (ALTERNATE LOOP)

ITEM NO.	PROGRAM NAME OR ACRONYM	PROGRAM TITLE OR CAPSULE DESCRIPTION	PROGRAM OBJECTIVES	LIMITATIONS
1	SAANT	Steady-State Analysis of Ablating Nostips (obtained from Aerothem)	R/V nostips are analyzed with a very generalized treatment of the wall chemistry.	Steady-state ablation, i.e., no in-depth transient response

The mass loss rates for the RMV-340 vehicle are considerably larger than for the other vehicles because of the large size and very high vehicle velocities. These ablation rates were calculated at TRW during the course of an earlier study and are reported in Reference 1. The Minuteman transition criteria was used. The predictions were found to lie within the error bounds of the flight measured mass loss rates. At an altitude of 25 km, there is significant char removal as well as pyrolysis, suggesting that the steady state ablation assumption may be made to a good approximation (Section 3). This assumption was imposed in the present case using the analysis built into the KBLIMP computer code, and the result is also shown in Figure 5. The predicted value also lies within the error bounds of the flight measurement.¹ In addition, a surface temperature of 2700°K was predicted which was in full agreement with the value deduced from on-board flight experiments.¹ A transition location consistent with the flight measured transition location was imposed on the calculation (at a distance of about 100 cm aft of the tip).⁴

Heatshield surface temperature and mass flux distributions for each vehicle are presented in Figures 6 and 7 for the altitudes outlined in Table 2. The surface temperature of the full-scale vehicle is about 550°K higher than that of the small vehicle. These temperatures have a strong affect on the degree of sodium ionization occurring near the wall, and hence on the electron concentration. The mass flux distributions are ordered in the same manner as the surface integrated mass flow values of Figure 5.

The velocity distribution at the edge of the boundary layer for the three vehicles is presented in Figure 8. The variation in edge-of-boundary-layer velocity for the small and full scale vehicles is due to the presence of a thick shock-generated entropy layer into which the boundary layer is growing. The entropy layer is the product of shock curvature and its importance scales with the nose bluntness ratio R_N/R_B . Clearly, the entropy layer is not entrained into the boundary layer before the end of the vehicle is reached for $R_N/R_B > 0.11$ (Table 1). In contrast, the RMV-340 vehicle is sharp ($R_N/R_B = 0.004$) and the entropy layer

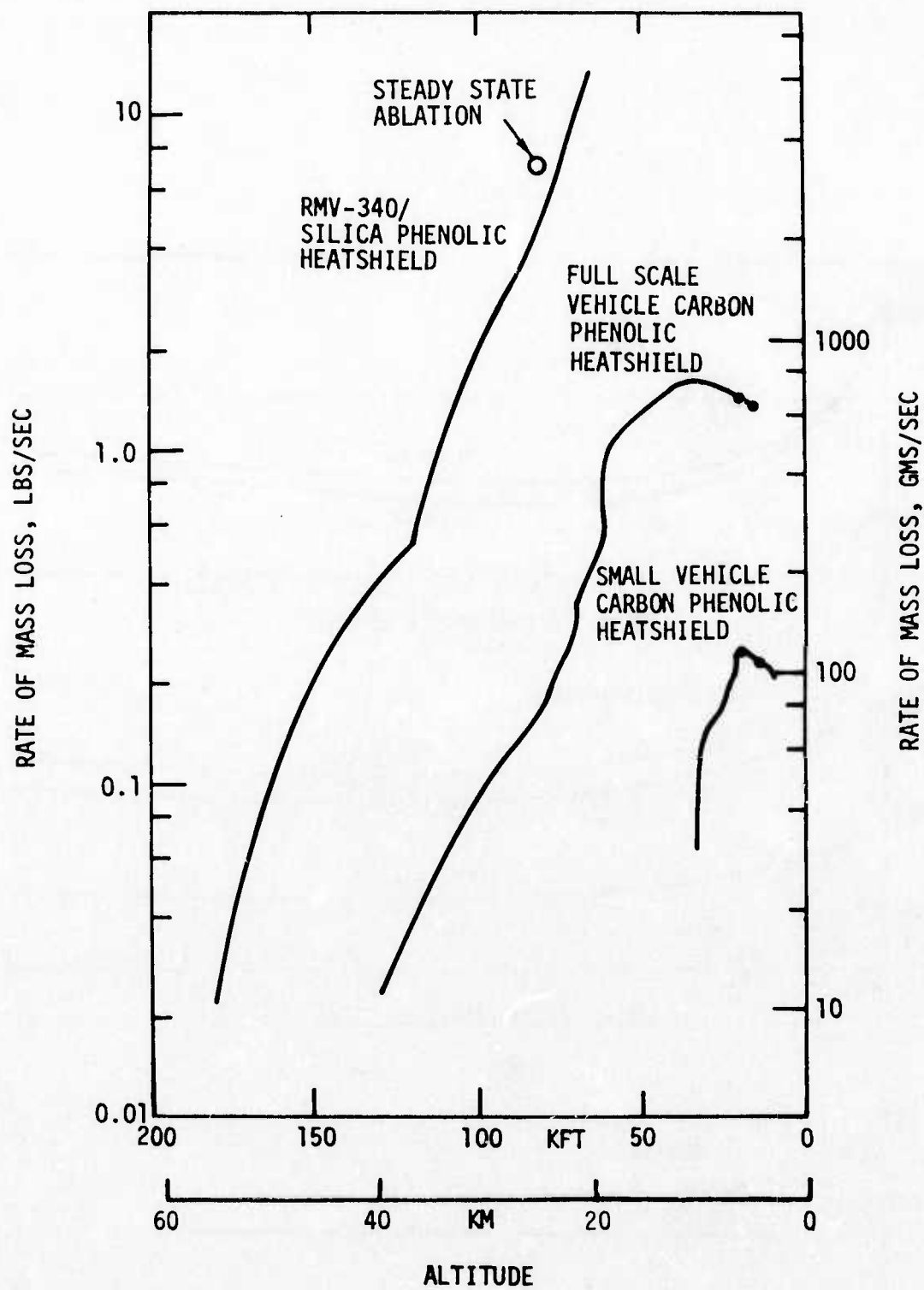


Figure 5. Surface Integrated Mass Loss Histories

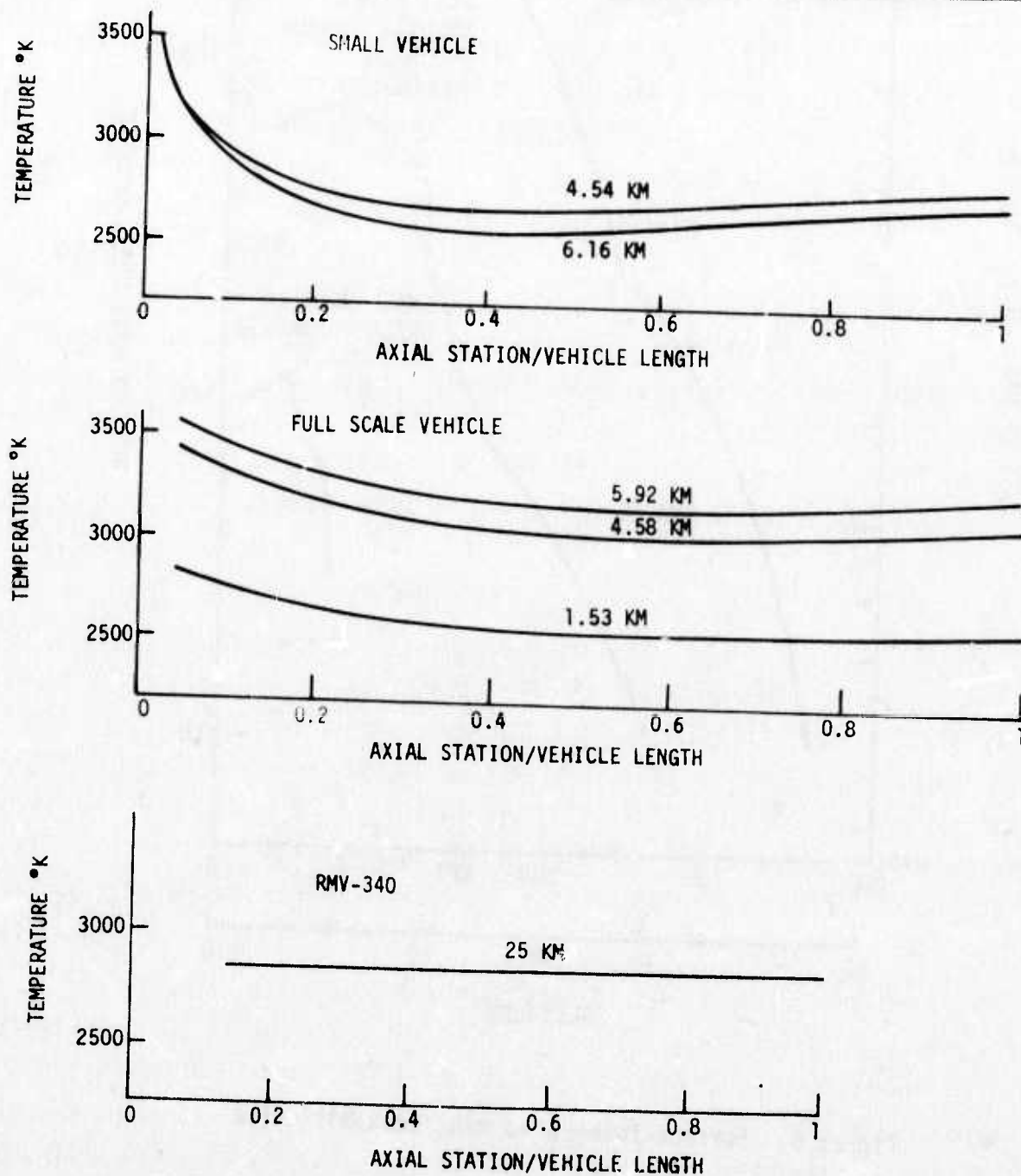


Figure 6. Frustum Surface Temperature Distributions

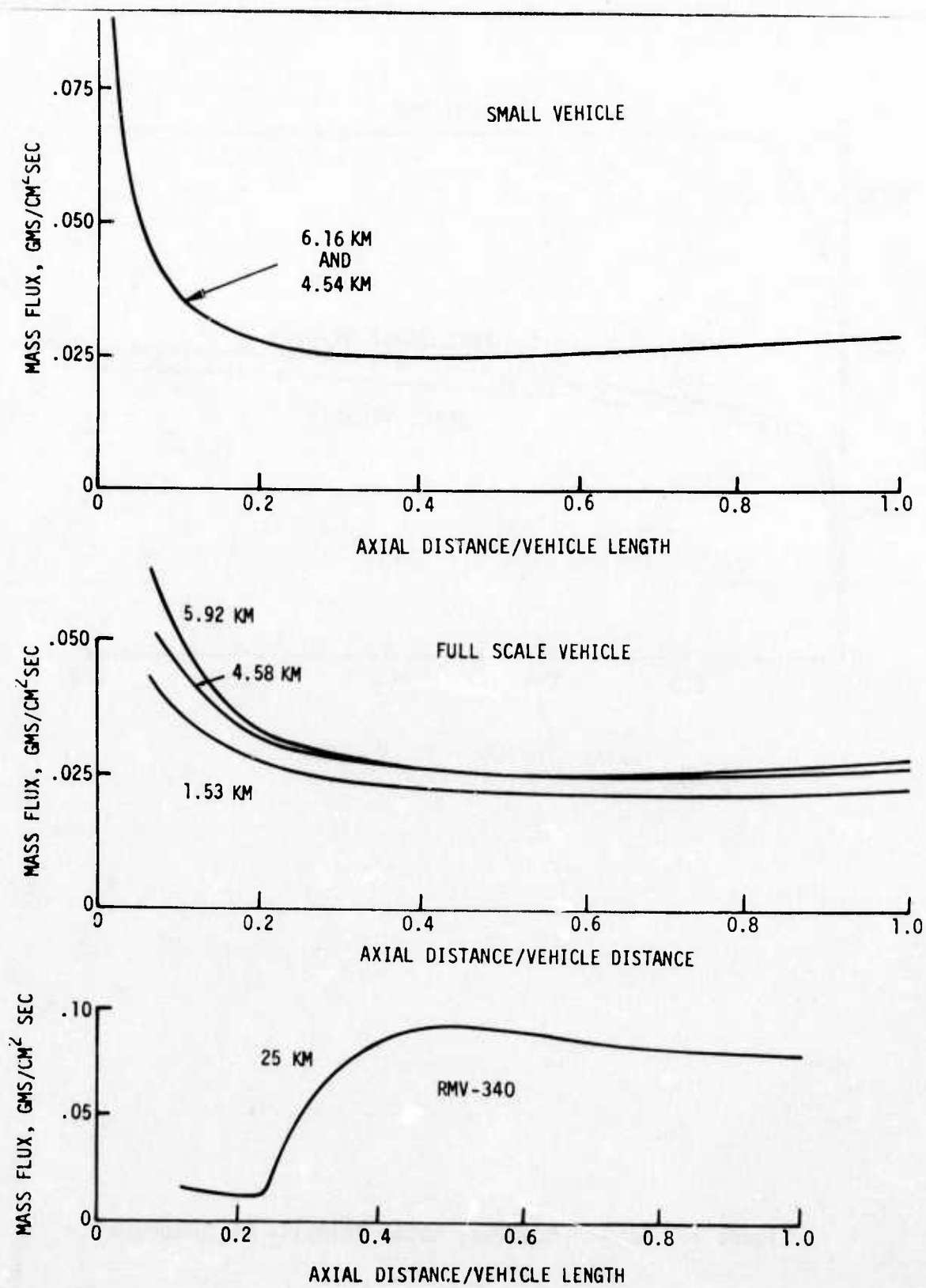


Figure 7. Frustum Mass Flux Distributions

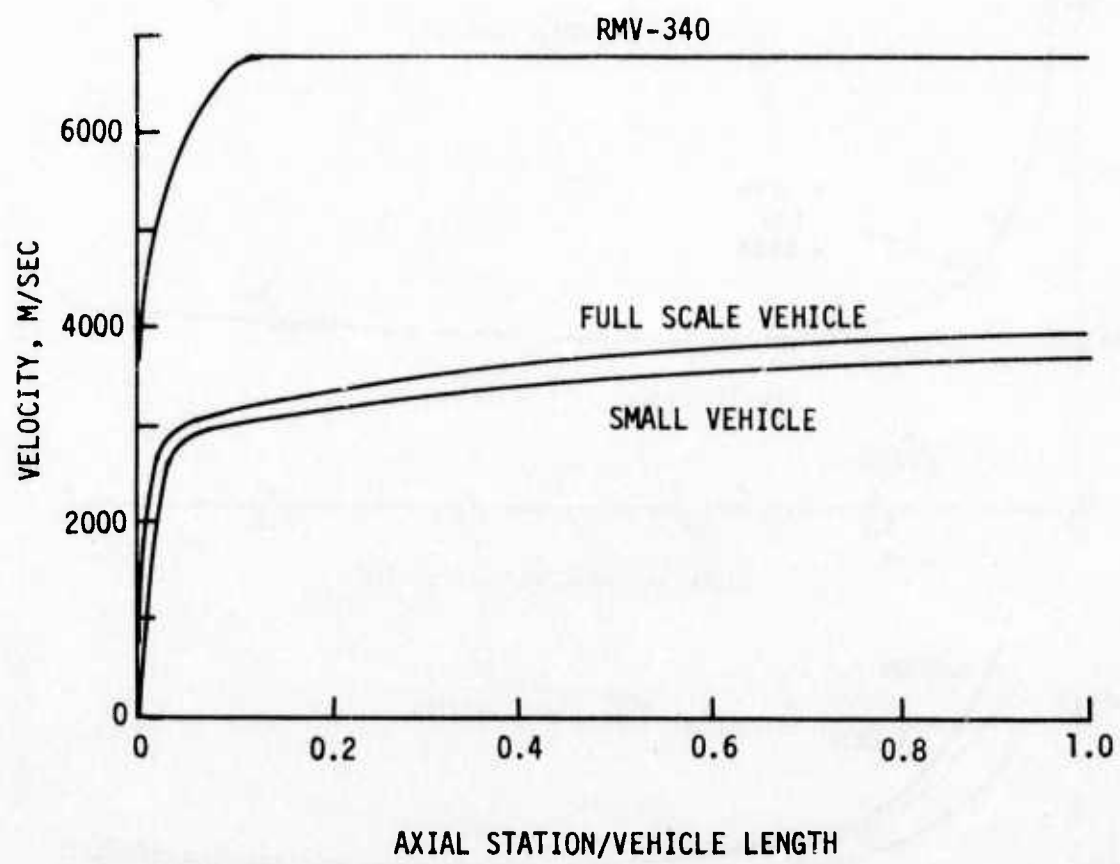


Figure 8. Edge-of-Boundary Layer Velocity Distribution

produced in the nose region is quickly swallowed by the boundary layer aft of the tip. The fluid at the edge of the boundary layer on the frustum has come through the asymptotic straight portion of the conical portion of the bow shock and the edge properties are therefore uniform.

The pressure on the frustum of each vehicle rapidly becomes uniform aft of the tip. Values of pressure ratio on the conical afterbodies are given in Section 4.1.

A strong temperature variation will accompany the velocity variation at the edge of the boundary layer since the stagnation enthalpy ($H = h + U^2/2$) is constant within the shock layer and equal to the free stream stagnation enthalpy ($H = H_\infty = h_\infty + U_\infty^2/2$).

4. ELECTRON SOURCES AND CHEMICAL EQUILIBRATION IN COMBUSTING BOUNDARY LAYERS

In the case of non-ablating hypersonic blunt cones, there are two principle sources of electrons in the boundary layer. Electrons are generated in the nose region of a blunted cone due to shock heating. The shock-heated air expands and flows around the nose onto the conical portion of the body where entrainment into the boundary layer occurs. Recombination of electrons before entrainment can only occur through a slow three-body reaction and does not, therefore, tend to be equilibrated at the reduced temperatures and concentrations accompanying the expansion. Once in the boundary layer, the swallowed electrons diffuse to the wall where recombination occurs thereby diminishing the streamwise flux of electrons from the nose region. This effect, combined with the increasing flow area of the developing conical boundary layer, leads to a net reduction of peak electron concentration with wetted distance along the conical surface. A second source of electrons is the ionization of air directly within the boundary layer due to the high temperatures present caused by viscous dissipation of kinetic energy.

In the case of ablating phenolic heatshields, electrons are present through the release of low "ionization potential" impurities or seedant materials. The major products of ablation (C , C_2 , CO , CO_2 , H , H_2 , OH , H_2O) characteristically have high ionization potentials so they tend not to contribute in an important way to the electron density. Pure air ionization in the boundary layer tends to be small because of the involvement of oxygen in the combustion of the ablation products. Thus the primary factors affecting electron density around an ablating vehicle are pure air ionization due to the nose bluntness effects and the introduction of low ionization-potential ablation impurities or seedants into the boundary layer.

In past analyses,⁽¹⁾ the combustion of hydrocarbons ablated into the high temperature boundary layer has been assumed to occur primarily through reactions with atomic oxygen at rates which are weakly dependent on temperature. These rates tend to be rapid compared to the rates of formation

of atomic oxygen by dissociation of molecular oxygen. Thus, oxygen dissociation was the controlling mechanism for equilibrium of the combustion reactions in the ablating boundary layer, unless sufficient oxygen atoms were already present from the high temperature nose region due to the decomposition of air through the bow shock wave. The combustion chemistry thus tended to be in equilibrium for blunted cones more so than for sharp cones where the equilibration of oxygen dissociation took place only after transversal of a sufficient distance along the conical afterbody. This distance for pure air dissociation equilibrium can be estimated by an analysis similar to that of Levenski and Fernandez⁽⁵⁾ for ionization where it is shown that the pertinent parameter is PX/V_∞ where P is the cone pressure, X the wetted length, and V_∞ the vehicle velocity. For $V_\infty \approx 15$ kft, $P \approx 1.5$ atm, and $X = 1$ ft, the parameter is $PX/V_\infty = 10^{-4}$ atm-sec, and this value corresponds to conditions approaching equilibrium. Values corresponding to full equilibrium lie between 10^{-4} and 10^{-3} atm-sec depending on the boundary layer temperature (high altitude values are below 10^{-6} atm-sec).

These arguments ignore possible important additional mechanisms which diminish the distance to combustion equilibration in the boundary layer on a sharp cone. One is the reaction of the free radicals with molecular oxygen and the other is surface catalysis for the dissociation of the oxygen. Taking these in order, the oxygen dissociation is slow because of the higher energy of the O-O bond (118,000 cal/mole) and the fact that no bonds are formed in the course of the reaction. Hence, the activation energy for reaction is at least as large as the bond energy, and the probability of a collision with joint kinetic energy exceeding 118,000 cal/mole, even at 3500°K is very low. This situation is altered because the high temperature ablation of phenolic is likely to yield a few stable molecules (H_2 , CH_4 , C_2H_2 , C_2H_4 , C_2H_6 , CH_2O) and a large number of atoms and free radicals (e.g., C_n , O, N, H, OH, CH_3 , CH_2 , C_2H_5 , HCO, etc.). The reaction of an oxygen molecule with a free radical, where two stable products are formed, may proceed with very low activation energy, as, for example, $CH_3 + O_2 \rightarrow CH_2O + HO$, for which the activation energy is close to zero. A comparison of rate constants⁽¹⁾ follows.

Reaction	$k(\text{cm}^3 - \text{mole}^{-1} \text{sec}^{-1})(\text{approximately})$
$\text{CH}_3 + \text{O}_2 \rightarrow \text{CH}_2\text{O} + \text{HO}$	10^{11}
$\text{CH}_4 + \text{O} \rightarrow \text{CH}_3 + \text{HO}$	10^{12}
$\text{CH}_3 + \text{O} \rightarrow \text{H}_2\text{CO} + \text{H}$	10^{13}
$\text{C}_2\text{H}_5 + \text{O}_2 \rightarrow \text{C}_2\text{H}_5\text{O}_2$	10^{12}
$\text{CN} + \text{O}_2 \rightarrow \text{NCO} + \text{O}$	10^{12}

From this table, it can be seen that free radicals (CH_3 , C_2H_5 and CN) react with O_2 with rates comparable to, or within, one or two orders of magnitude of the rates of stable molecules reacting with O (given as 10^{12} or $10^{13} \text{ cm}^3 \text{ mole}^{-1} \text{ sec}^{-1}$).⁽¹⁾ It is not known what the ratio of free radicals is to stable molecules in the ablation process. Certainly the percentage is high and this mechanism, reaction with O_2 molecules, might well promote a rapid attainment of combustion equilibrium. Failure to observe this in computer modelling in the past is not significant as there are only about 4 rate constants in the literature for reaction between free radicals and O_2 molecules.

The second factor, surface catalysis, is again speculative. There is a vast literature on catalytic oxidation of hydrocarbons observed at temperatures from ambient to about 1000°K ; however the objective has been to control the oxidation in order to produce a favorable product rather than carry out complete combustion. There, a catalyst is usually a transition metal (Pt) or metallic oxide (V_2O_5 , CrO_2), which promotes the formation of atomic oxygen on the surface and then readily transfers this O to the hydrocarbon. At 3500°K , a charred phenolic surface might well hasten the establishment of an equilibrium O level by lowering the activation energy for the $\text{O}_2 + \text{M} \rightarrow \text{O} + \text{O} + \text{M}$ reaction. An oxygen molecule striking the surface would tend to form $-\text{C} \equiv \text{O}$ bonds, indeed may do so part of the time, gradually eroding the surface to form carbon monoxide and oxygen atoms. It may only partly form the carbon oxygen triple bond but weaken the oxygen-oxygen bond, lowering the activation energy for the formation of oxygen atoms, and greatly accelerate that process. Under boundary layer conditions,

oxygen molecules collide with other gas phase molecules about 10^{28} times per sec per cm^3 of gas, but wall collisions occur 10^{27} times per sec per cm^2 of wall. Hence, if the wall lowered the activation energy for dissociation from 118,000 cal/mole to about 40,000 cal/mole, this would produce O atoms 10^5 more rapidly, easily maintaining the equilibrium as the combustion reactions proceed.

Considering that pure O_2 dissociation would lie close to equilibrium under the conditions of interest here, and that other mechanisms exist which would enhance equilibration of the combustion process, the assumption of chemical equilibrium within the boundary layer will be made in the present analysis.

On the other hand, the ionization of impurity or seedant materials also ablated into the boundary layer may not be an equilibrium process. The reaction kinetics for ionization of these impurity or seedant materials are temperature dependent, and hence are dominated by ablation products through the temperatures which result from the combustion processes in the boundary layer. The boundary layer tends to be weakly ionized so that ignoring the energy involved in the ionization reactions yields only small errors in the thermal and density distributions. For this reason, the boundary layer growth and the major species profiles can be approximated by considering only the hydrocarbon combustion process.

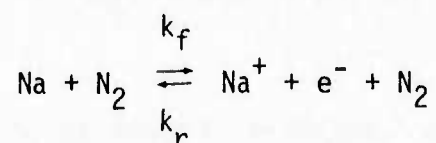
Thus, the charged species are treated as trace species whose distribution throughout the boundary layer depends on turbulent diffusion and finite rate chemistry as determined from the temperature and major species concentrations of the equilibrium boundary layer.

4.1 AFT SHOULDER BOUNDARY LAYER PROPERTIES

The KBLIMP computer program presented in Table 3 and discussed in Appendix I was applied to the present cases with carbon or silica phenolic ablation products undergoing equilibrated combustion processes in the boundary layer. Low ionization potential impurities or seedant materials accompanying the ablation process were also assumed to be equilibrated at

the wall but were allowed to undergo non-equilibrium reaction kinetics in the boundary layer. These materials were represented by an effective sodium atom concentration in the heatshield at levels previously discussed.

The ionization of sodium in the boundary layer was assumed to occur through a collisional interchange with diatomic nitrogen, with a rate constant determined from the data of Hollander, et al ⁽⁶⁾. The reverse reaction rate was determined from knowledge of the equilibrium constant determined in KBLIMP from the JANAF thermodynamics tables. Thus,



$$k_f = 1.2 \times 10^{16} T^{0.5} e^{-59,400/T} \quad (\text{cm}^3/\text{mole sec})$$

(T in degrees Kelvin)

To determine the degree to which sodium ionization has approached equilibrium, the boundary layer calculations for some cases were repeated under the conditions of full equilibration of sodium ionization throughout the boundary layer.

The elemental composition of the nose cap and frustum materials used in the calculation is presented in Table 4. Sodium was assumed present only in the frustum heatshield material at equal ppm levels in both the ablated char and pyrolysis materials.

Properties of the boundary layer at the aft end of the frustum of each of the three vehicles are now presented. A rather complete set of graphically formatted data showing the development of the boundary layer along the entire body of each vehicle has been delivered to the contracting agency as supplementary information.

A summary of the velocity, temperature, and pressure at the edge of the boundary layer at the end of the frustum of each vehicle at the altitude calculated is presented in Table 5.

Table 4 . Elemental Composition By Mass of Ablation Materials

NOSE-CAP		FRUSTUM	
ATJ-GRAPHITE (ALL VEHICLE)		CARBON-PHENOLIC SMALL VEHICLE/FULL SCALE VEHICLE	SILICA PHENOLIC RMV-340
		PYROLYSIS	CHAR
HYDROGEN	1.00	.093	.023
CARBON		.547	.878
NITROGEN		.019	.010
OXYGEN		.341	.089
SILICON		.000	.000
			.050
			.368
			.000
			.416
			.165
SODIUM (SEEDANT)	.0	.000050	.000050
		.000500*	.000500*
		.001000*	.001000*

* Small vehicle only.

Table 5. Aft Station Edge-of-Boundary Layer Properties and Boundary Layer Thickness

	ALTITUDE KM	TEMPERATURE °K	PRESSURE ATM	VELOCITY MPS	BOUNDARY LAYER THICKNESS* CM
Small Vehicle	6.16	547	1.27	3752	.25
	4.54	506	1.42	3508	.21
Full Scale Vehicle	5.92	1667	1.68	3996	.95
	4.58	1889	2.33	3477	1.07
	1.53	911	2.17	2678	.73
RMV-340	25.0	800	0.416	6710	5.1

* $\frac{u}{u_e} \cong 0.99$

4.1.1 Full Scale Vehicle Boundary Layer

A figure showing the velocity, temperature, and density profiles, and a separate figure showing the ion/electron concentration profiles for both non-equilibrium and equilibrium sodium ionization at the aft station of the frustum are presented in Figures 9 through 16 for the three altitudes of 5.92, 4.58, and 1.53 km.

These results show that sodium is the primary source of ions/electrons in the boundary layer. Ions from the combustion process and NO^+ were included as equilibrated species and their contributions were found to be negligible.

Both at 5.92 and 4.58 km, the equilibrium Na^+ (or e^-) profiles first increase away from the wall and then decrease by over an order-of-magnitude through the boundary layer. These profiles coincide with the temperature profile which also displays a strong decrease in the outer portion of the boundary layer. In contrast, the non-equilibrium electron profiles decrease relatively more slowly from the wall with their maximum value occurring at the wall. Thus, in the non-equilibrium case, electrons are formed at the wall and rapid diffusion combined with slow recombination leads to higher concentration levels in the outer boundary layer than exist in the equilibrium case.

The differences between the equilibrium and non-equilibrium profiles decreases so significantly between 5.92 and 4.58 km that the calculation of the electron profile at 1.53 km is expected to be acceptably approximated by the condition of chemical equilibrium, consequently a non-equilibrium calculation was not performed for this case.

4.1.2 Small Vehicle Boundary Layer

Velocity, temperature, and pressure profiles, and electron concentration profiles are shown for the aft station for the two altitudes of 6.16 and 4.54 km in Figures 17 through 22. The non-equilibrium electron concentration profiles are considerably flatter than those observed for the full scale vehicle. In addition, larger differences between the equilibrium and non-equilibrium electron profiles are observed in the outer portion of the boundary layer for the small vehicle.

The electron concentration levels for the small vehicle are considerably smaller near the wall than those observed for the large scale vehicle. Both profiles are based on a 50 ppm sodium concentration level in the heat-shield. Additional calculations for seeding levels of 500 and 1000 ppm were performed for the small vehicle. A comparison of resulting electron concentrations will be presented later with the wake results (Section 7).

Boundary layer profile data for the RMV-340 vehicle will also be presented in a separate section devoted to this vehicle (Section 8).

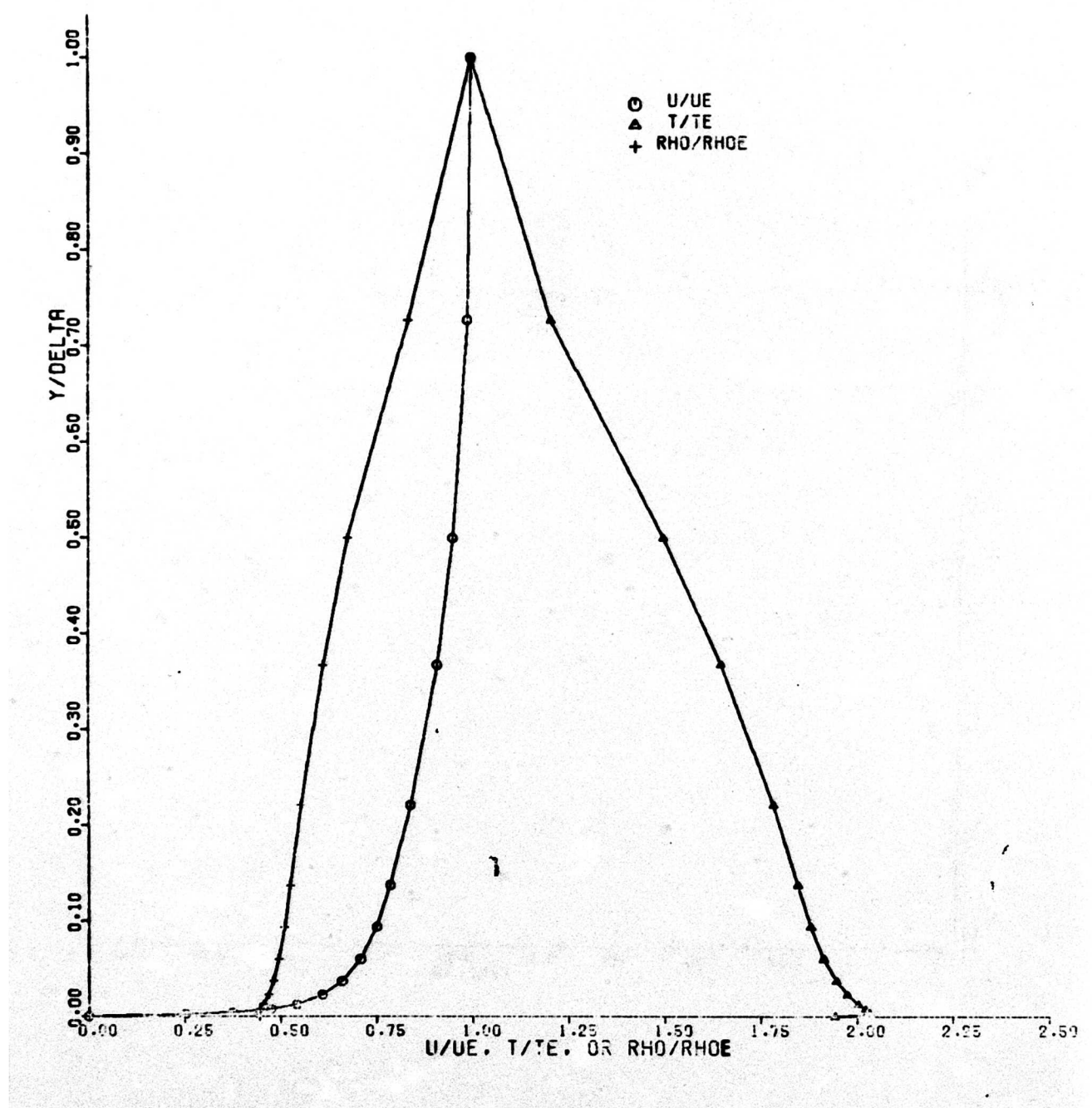


Figure 9. Full Scale Vehicle - 5.92 km - Aft Station Velocity, Temperature, and Density Profiles

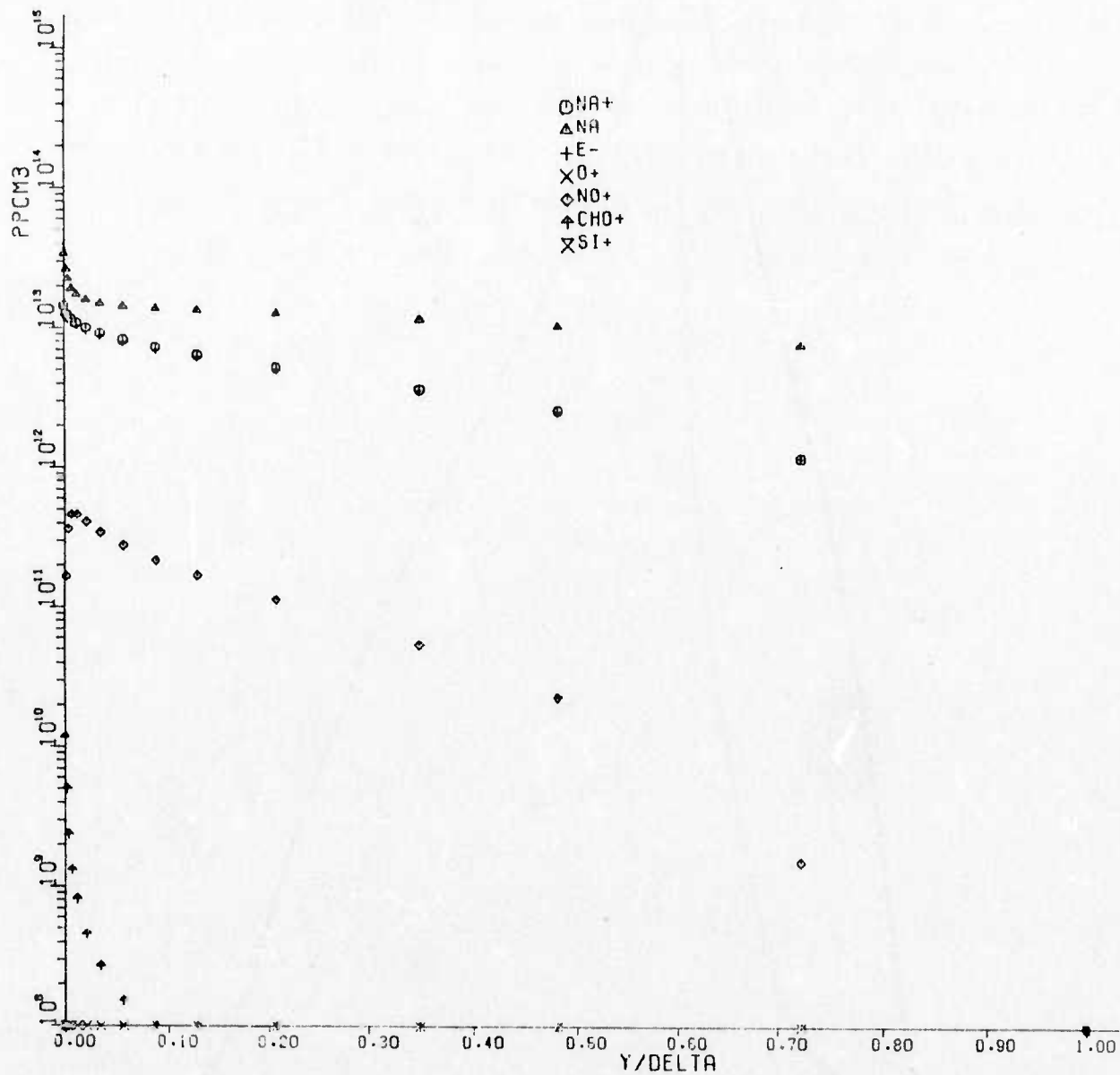


Figure 10. Full Scale Vehicle - 5.92 km - Aft Station Charged Particle Profiles - Non-Equilibrium Na Ionization

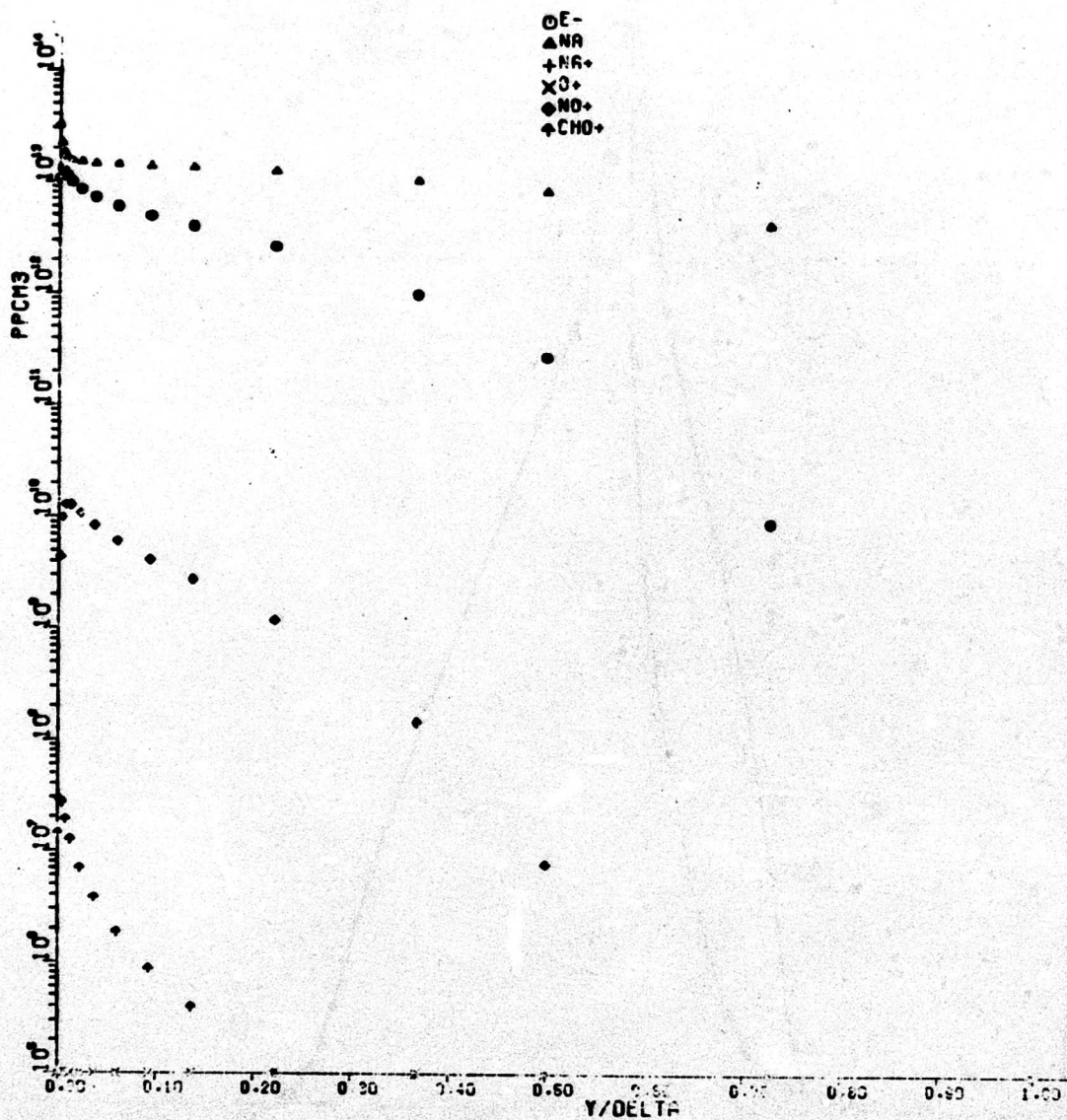


Figure 11. Full Scale Vehicle - 5.92 km - Aft Station Charged Particle Profiles - Equilibrium Na Ionization

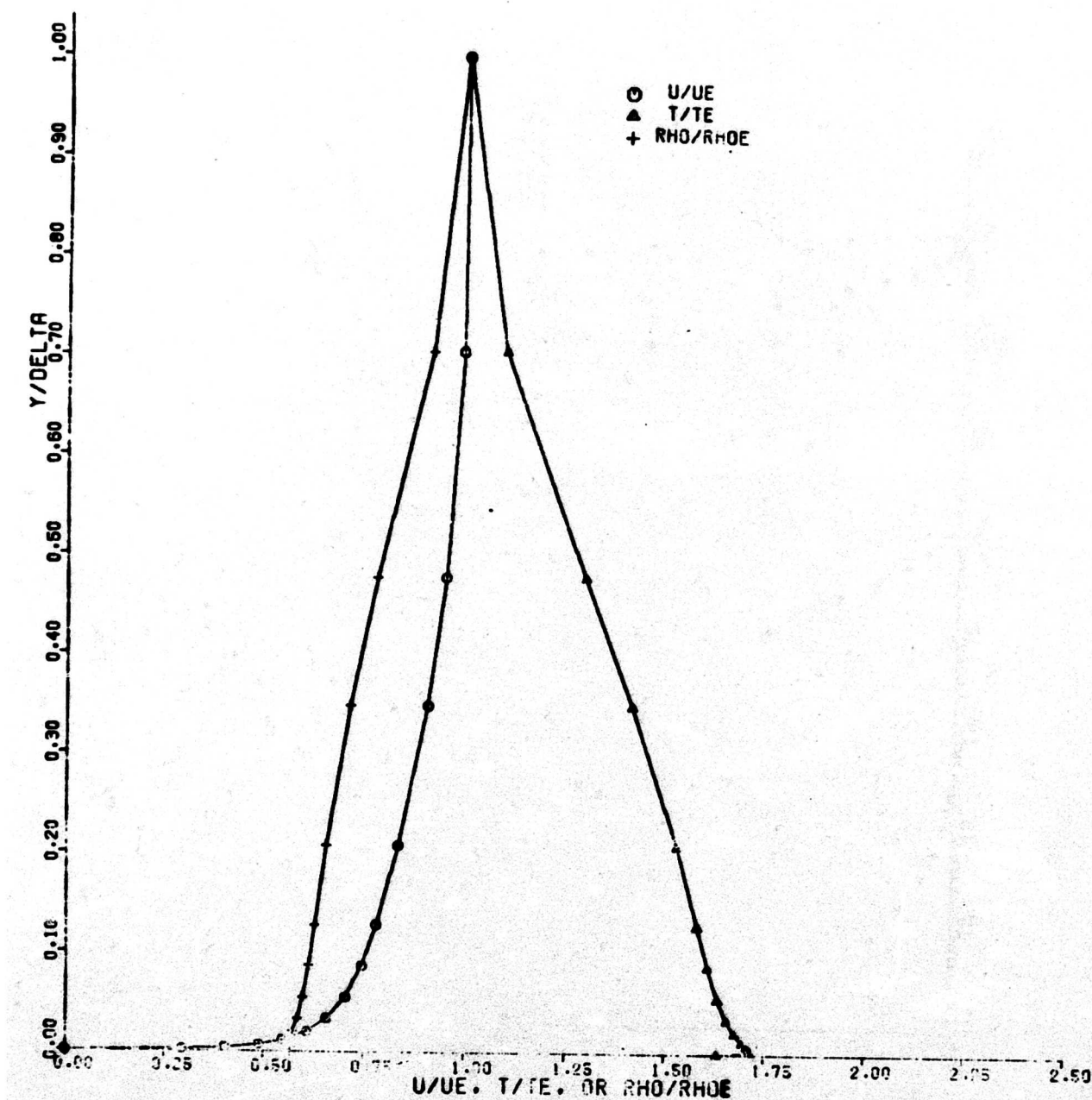


Figure 12. Full Scale Vehicle - 4.58 km - Aft Station Velocity, Temperature, and Density Profiles

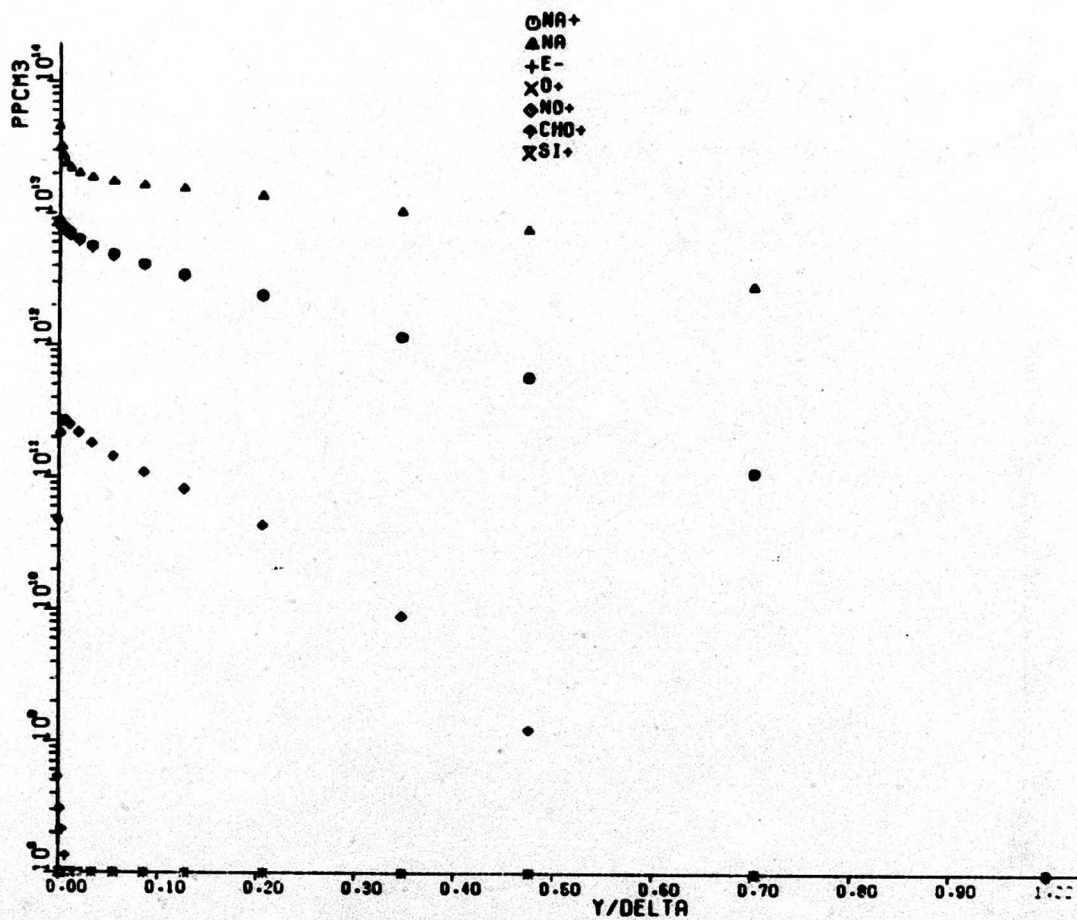


Figure 13. Full Scale Vehicle - 4.58 km - Aft Station Charged Particle Profiles - Non-Equilibrium Na Ionization

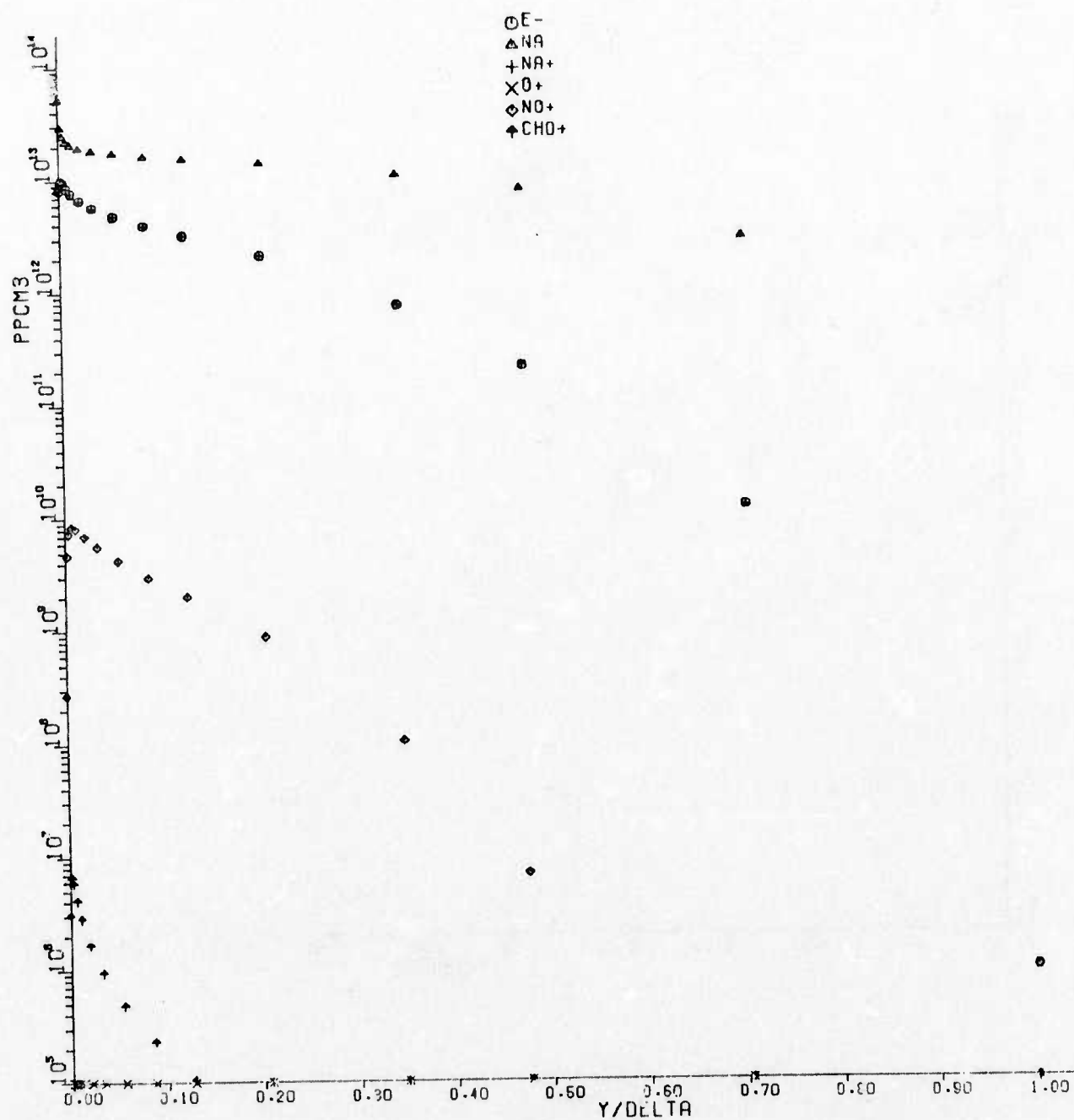


Figure 14. Full Scale Vehicle - 4.58 km - Aft Station Charged Particle Profiles - Equilibrium Na Ionization

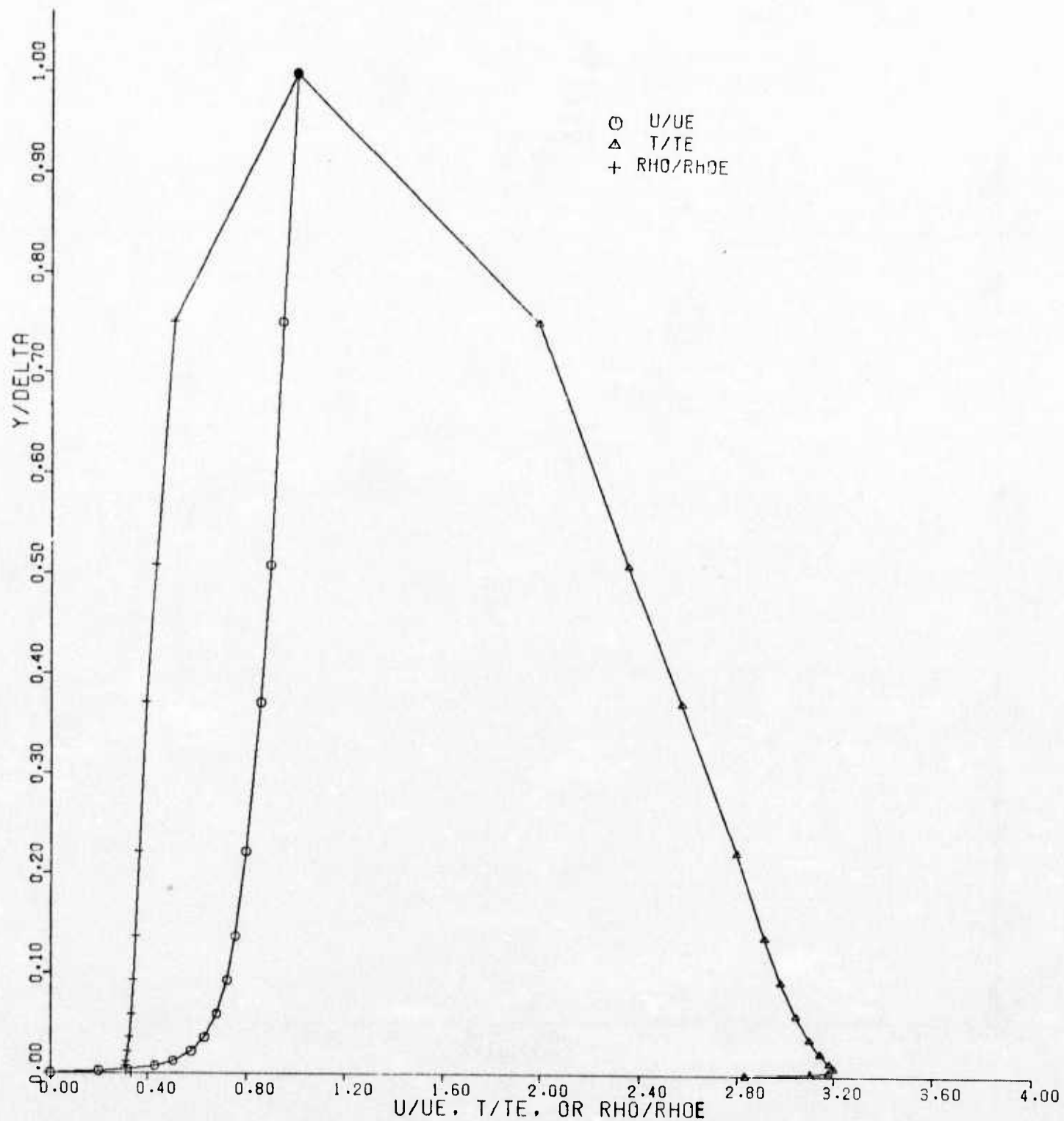


Figure 15. Full Scale Vehicle - 1.53 km - Aft Station Velocity, Temperature, and Density Profiles

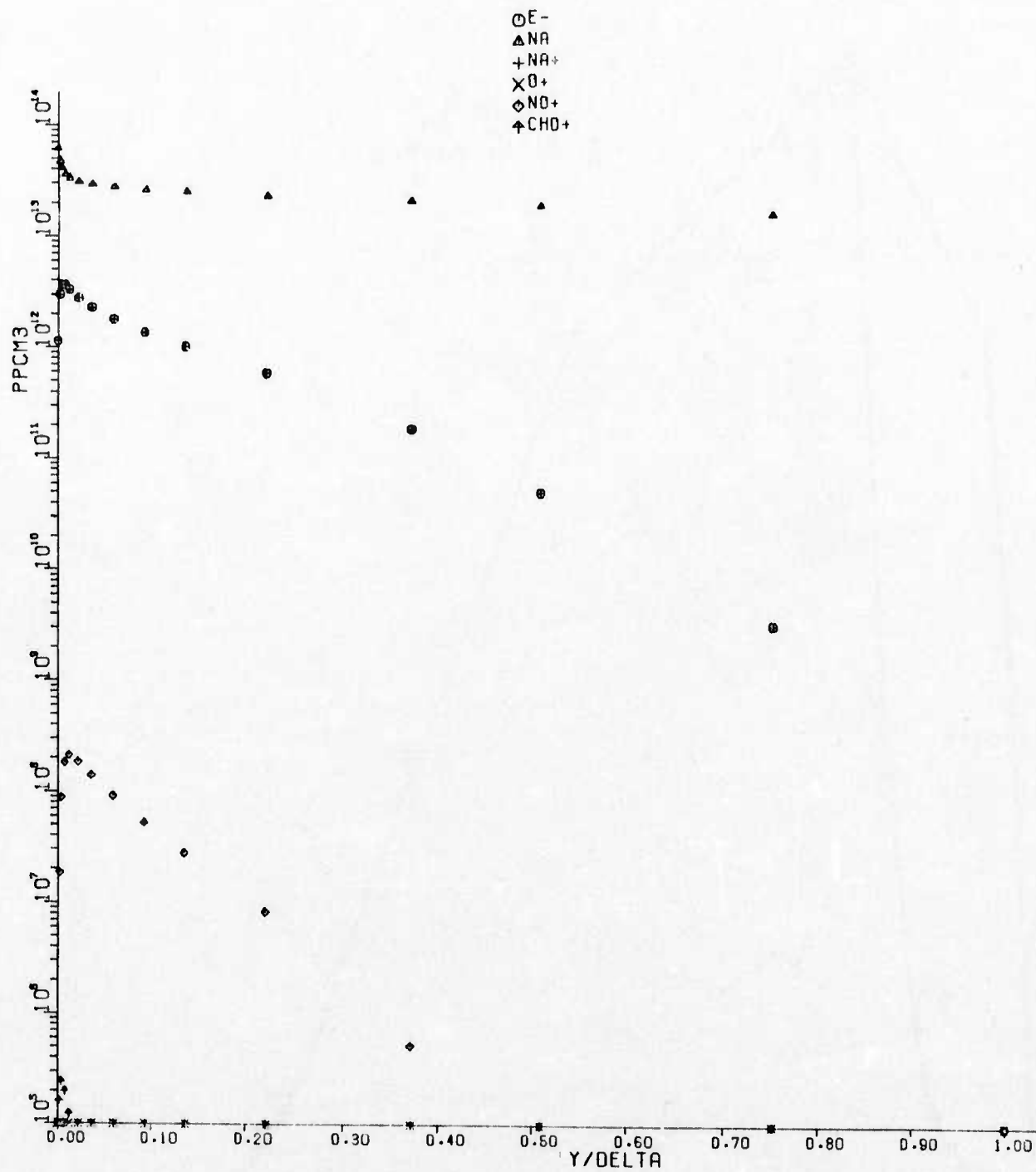


Figure 16. Full Scale Vehicle - 1.53 km - Aft Station Charged Particle Profiles - Equilibrium Na Ionization

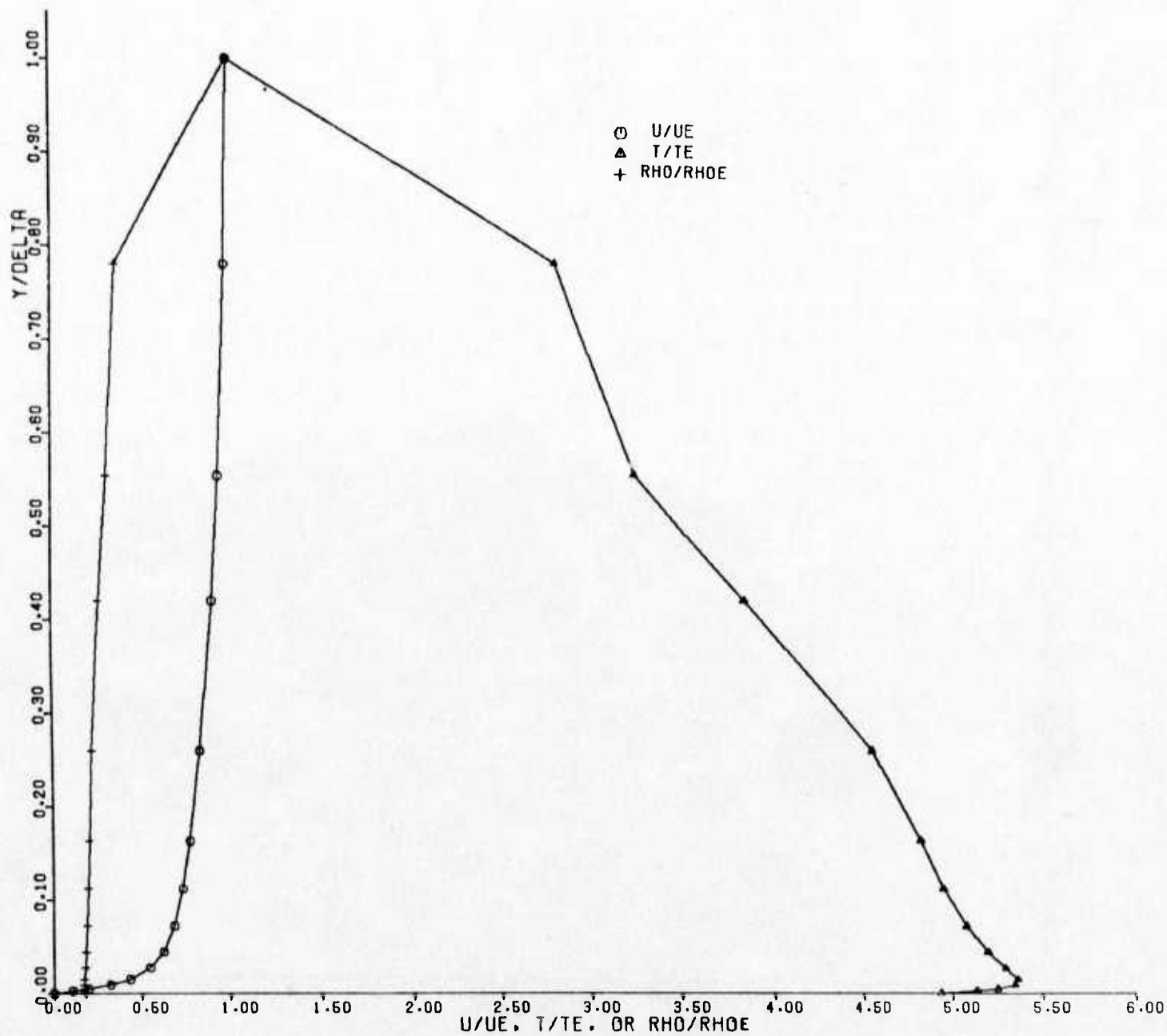


Figure 17. Small Vehicle - 6.16 km - Aft Station Velocity, Temperature, and Density Profiles

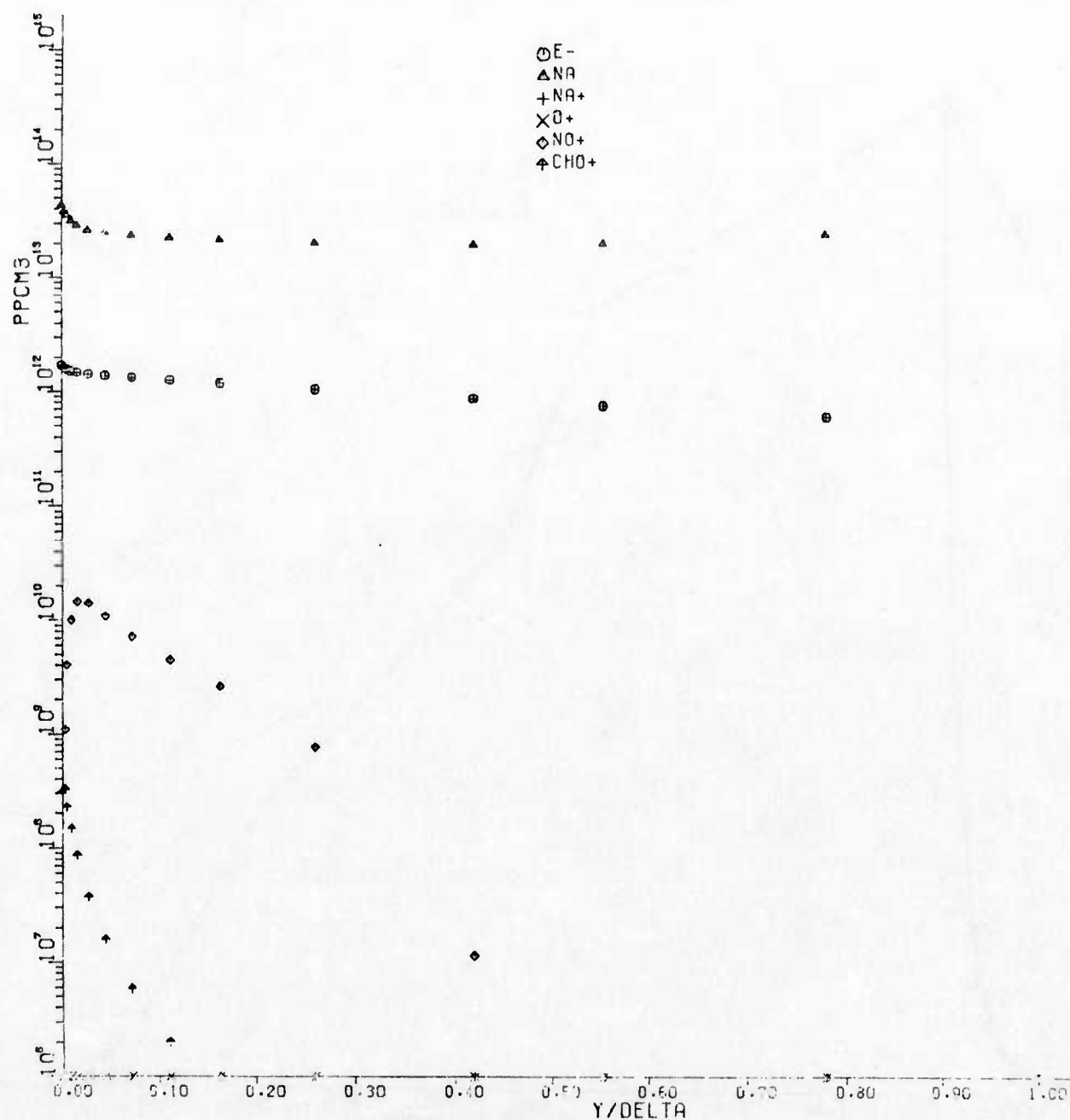


Figure 18. Small Vehicle - 6.16 km - Aft Station Charged Particle Profiles - Non-equilibrium Na Ionization

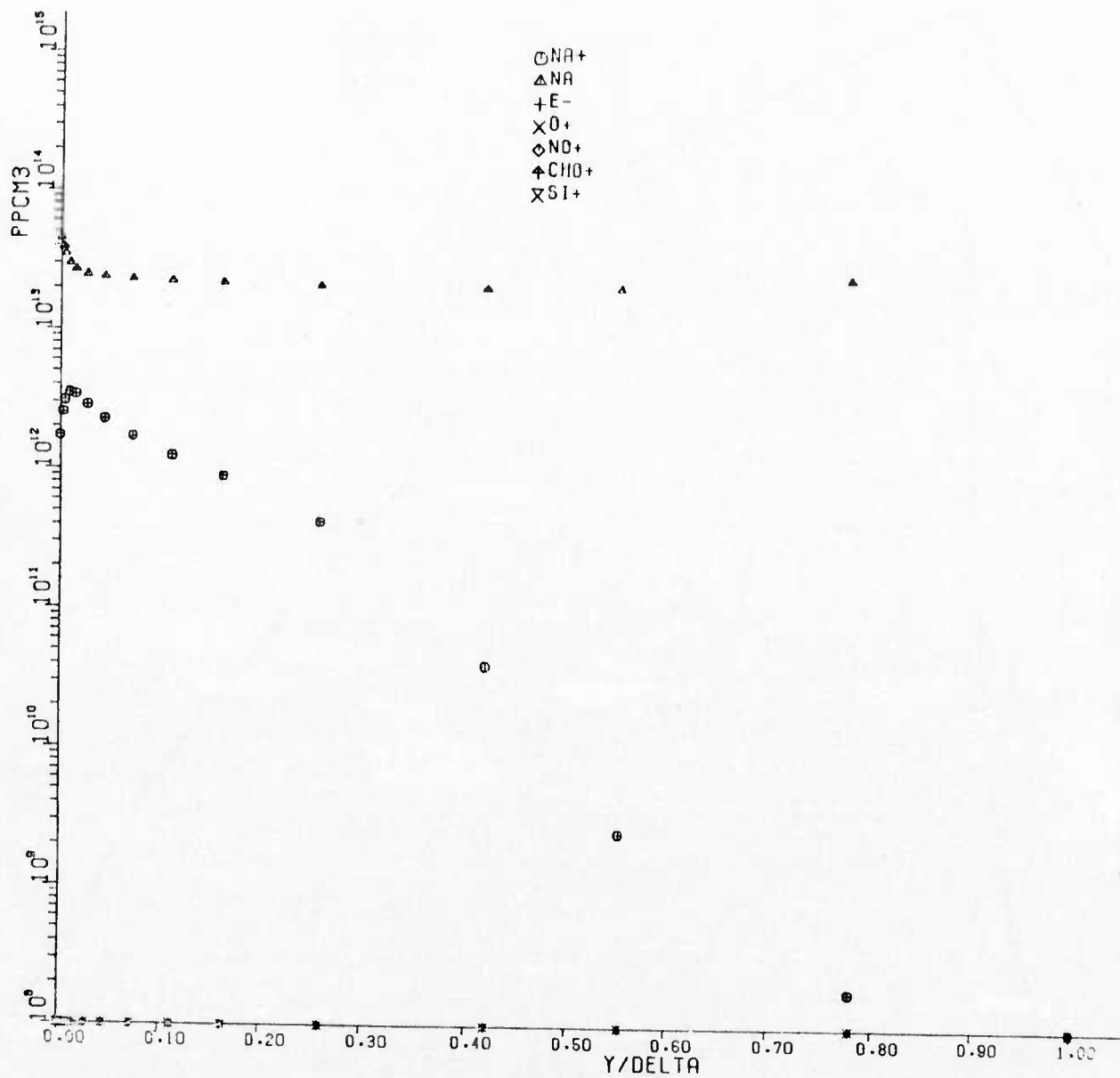


Figure 19. Small Vehicle - 6.16 km - Aft Station Charged Particle Profiles - Equilibrium Na⁺ Ionization

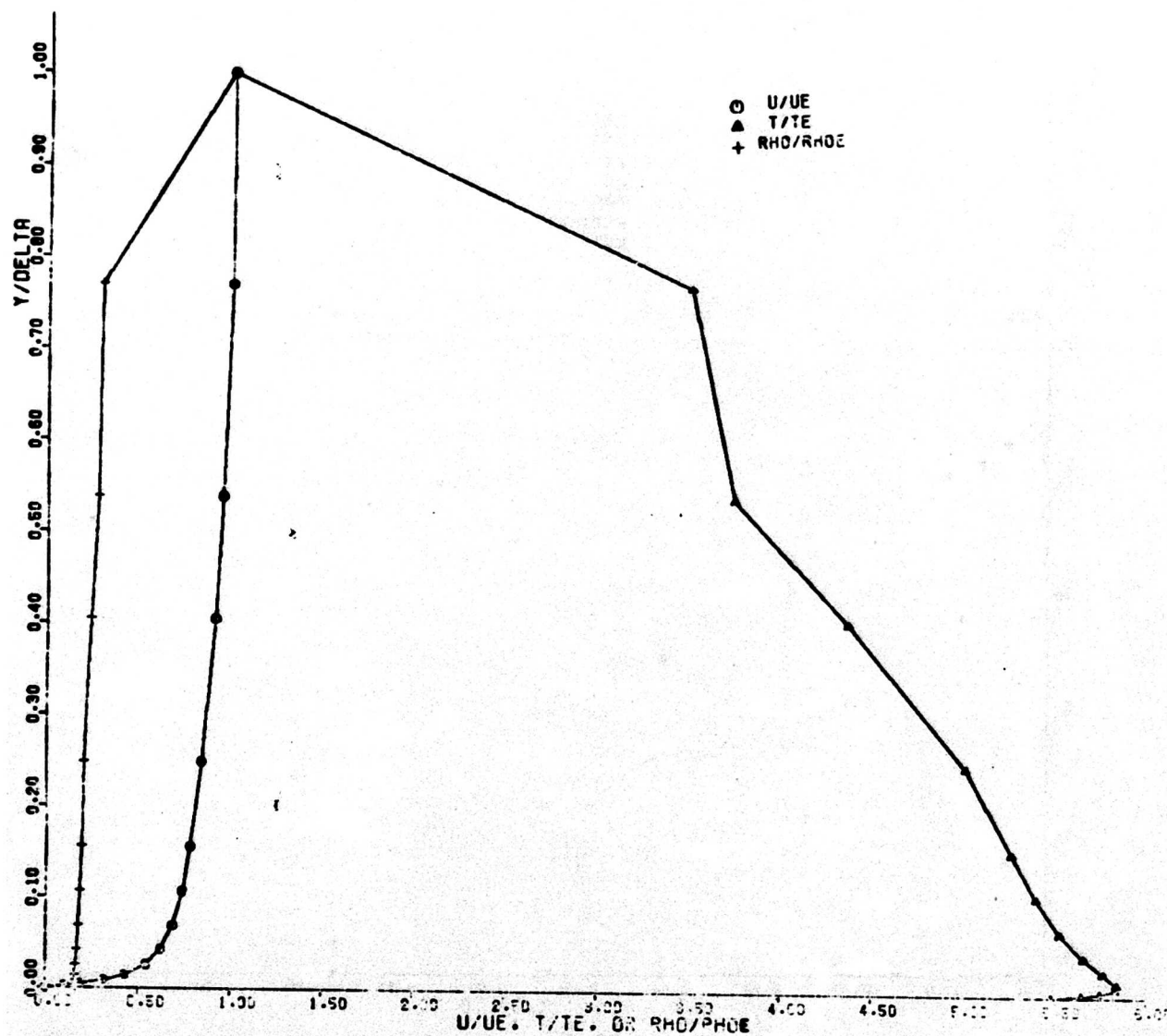


Figure 20. Small Vehicle - 4.54 km - Aft Station Velocity, Temperature, and Density Profiles

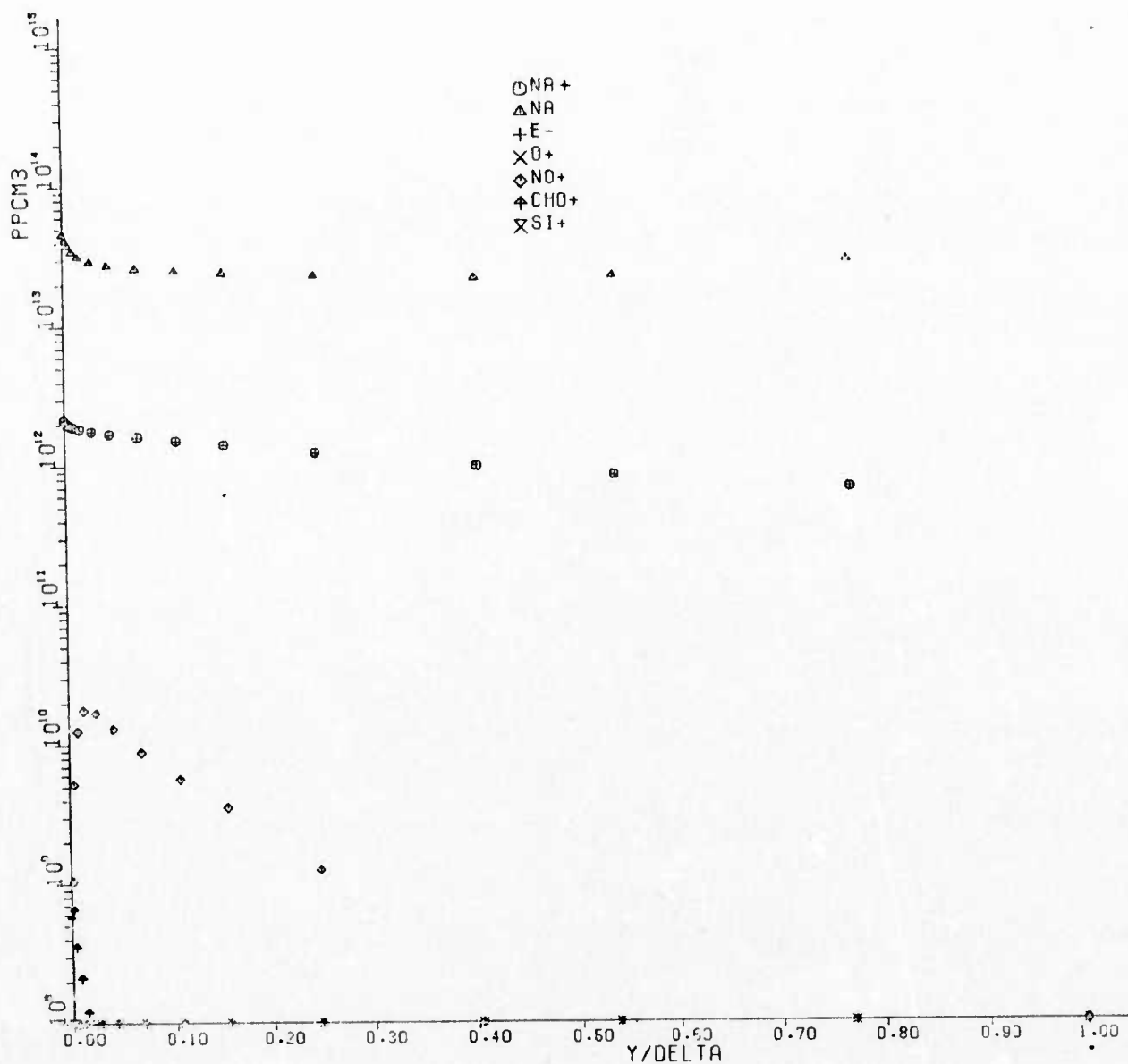


Figure 21. Small Vehicle - 4.54 km - Aft Station Charged Particle Profiles - Non-equilibrium Ionization

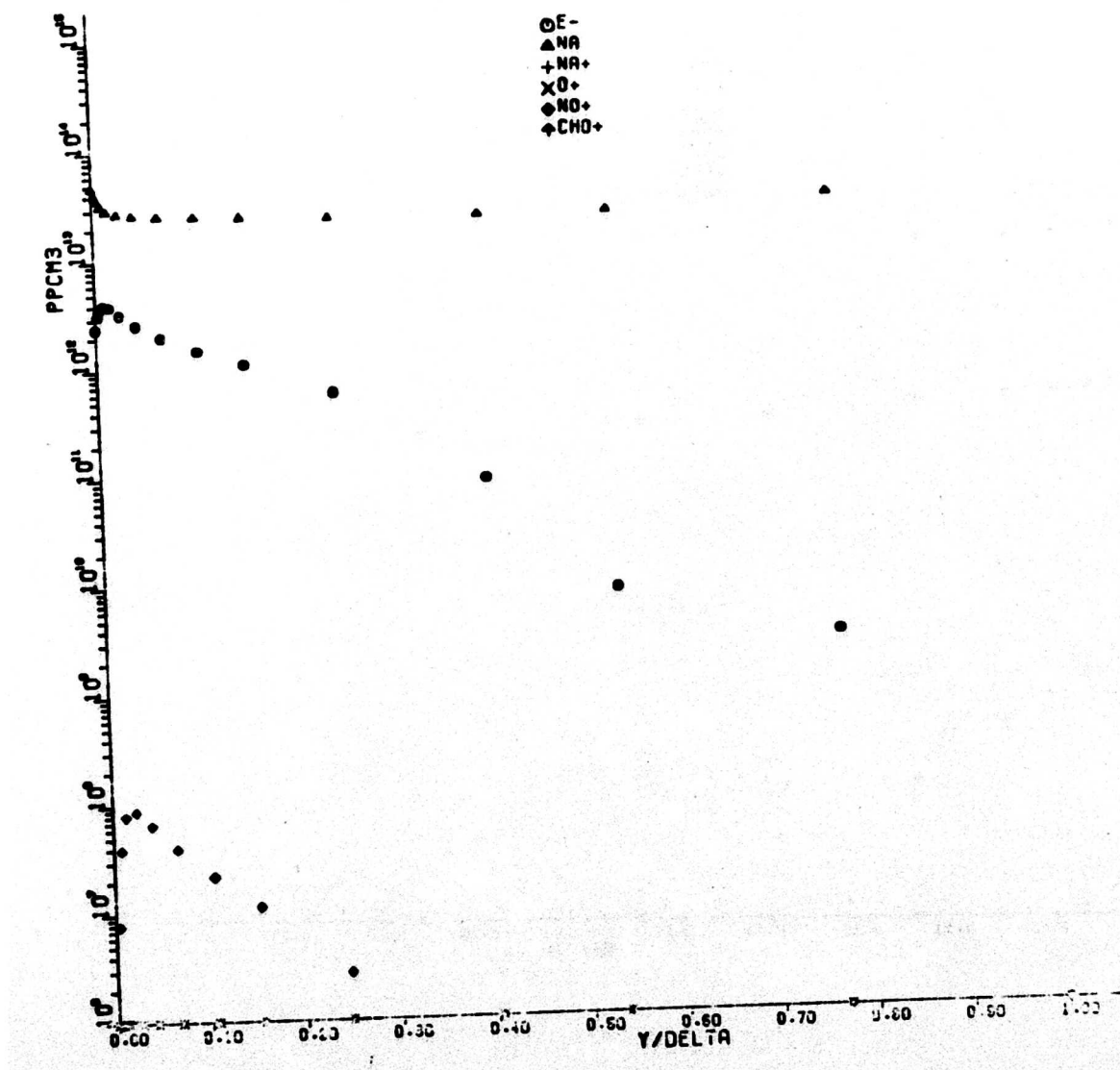


Figure 22. Small Vehicle - 4.54 km - Aft Station Charged Particle Profiles - Equilibrium Na Ionization

5. SHOULDER SEPARATION AND NEAR WAKE ANALYSIS

The flow adjacent to the base of a hypersonic vehicle is characterized by a number of features which include a recirculation region attached to the base over which the flow from the boundary layer passes after leaving the body. A shear layer develops and grows between the shed boundary layer and recirculation region which drives the recirculation region flow. As the boundary layer fluid coalesces (or implodes) on the axis-of-symmetry, the pressure near the axis rises and acts to turn the flow downstream. This process leads to the formation of a wake shock wave. These and other features of the flow are illustrated in Figure 23. Note also that as the boundary layer fluid expands into the near wake, the original edge-of-boundary layer streamline turns only gradually after separation, while the inner streamlines turn at the larger angles to fill the near wake. The separation process itself requires a pressure rise along the surface of the aft shoulder, and this rise initiates a weak compression wave which can be enhanced by the reflection of waves from the nearly constant pressure region adjacent to the recirculation zone. This often leads to the formation of a so called lip shock wave shown in Figure 23.

A crucially significant property of the near wake region is the presence of a large subsonic flow region adjacent to base. This includes most of the recirculation region and a narrow strip of flow lying about the axis downstream of the recirculation zone. This narrow strip eventually closes on the axis where the axis Mach number becomes unity. Within this region the downstream flow can communicate and have an influence on the upstream flow. Thus, the point along the shoulder of the vehicle at which the boundary layer separates is related directly to the base pressure which in turn depends on the subsequent downstream pressure disturbances, created and imposed on the subsonic region during the convergence and subsequent turning of the streamlines downstream of the recirculation zone.

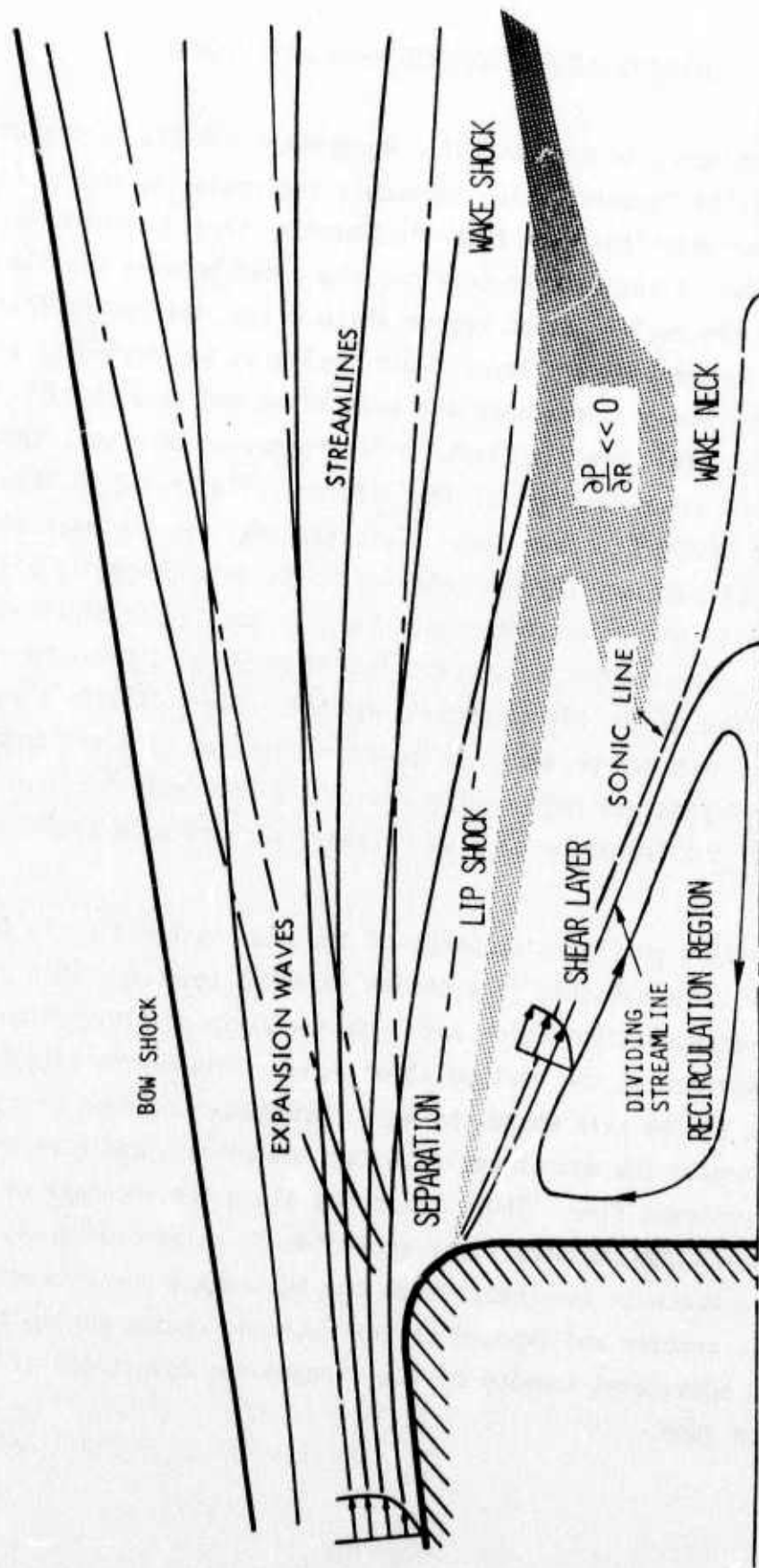


Figure 23. Elements of the Near Wake Flowfield

The mathematical treatment of the subsonic region and the adjacent supersonic flow in a steady-state formulation using the Navier-Stokes equations is, consistent with the expected importance of upstream influences, a boundary value problem. However, at sufficiently high Reynolds number it is not unreasonable to neglect streamwise diffusive transport and if the additional assumption is made that transverse pressure gradients can be neglected in subsonic flow regions, the mathematical character of the resulting equations becomes nominally that of an initial value problem. The upstream propagation of information when this problem is formulated as an initial value problem occurs through a resulting eigenvalue character of the governing equations.

Different eigenvalue behaviors are found for boundary layers and wakes. In the case of a boundary layer, a subsonic region always exists near the wall to provide a channel for the propagation of upstream information. Retaining the transverse momentum equation, and the displacement interaction with the outer supersonic flow leads to two types of divergent solutions about a singular envelope solution which represents the usual boundary-layer solution with viscous-inviscid flow interaction effects accounted for. An example of pressure distributions for the envelope solution and the two types of divergent solutions are shown in Figure 24 on the rounded shoulder of a body prior to separation. In one case, the pressure drops rapidly below that of the envelope solution. In the other case, the pressure rises above that of the envelope solution with a corresponding decrease in wall shear, resulting eventually in separation. These solutions can be generated by imposing infinitesimal perturbations on the initial profiles upstream on the vehicle. It has been found that all solutions yielding separation at a given point are essentially indistinguishable, regardless of the nature of the initial perturbation. Consequently, each separation point location characterizes a single distinct upstream solution. The proper one, of the infinitude of possible separation point locations, is determined by downstream flow conditions. Therefore the separation point location, and hence base pressure, takes on the characteristics of an eigenvalue.

The method of determining the proper separation point location becomes clear when the character of the solutions downstream of the

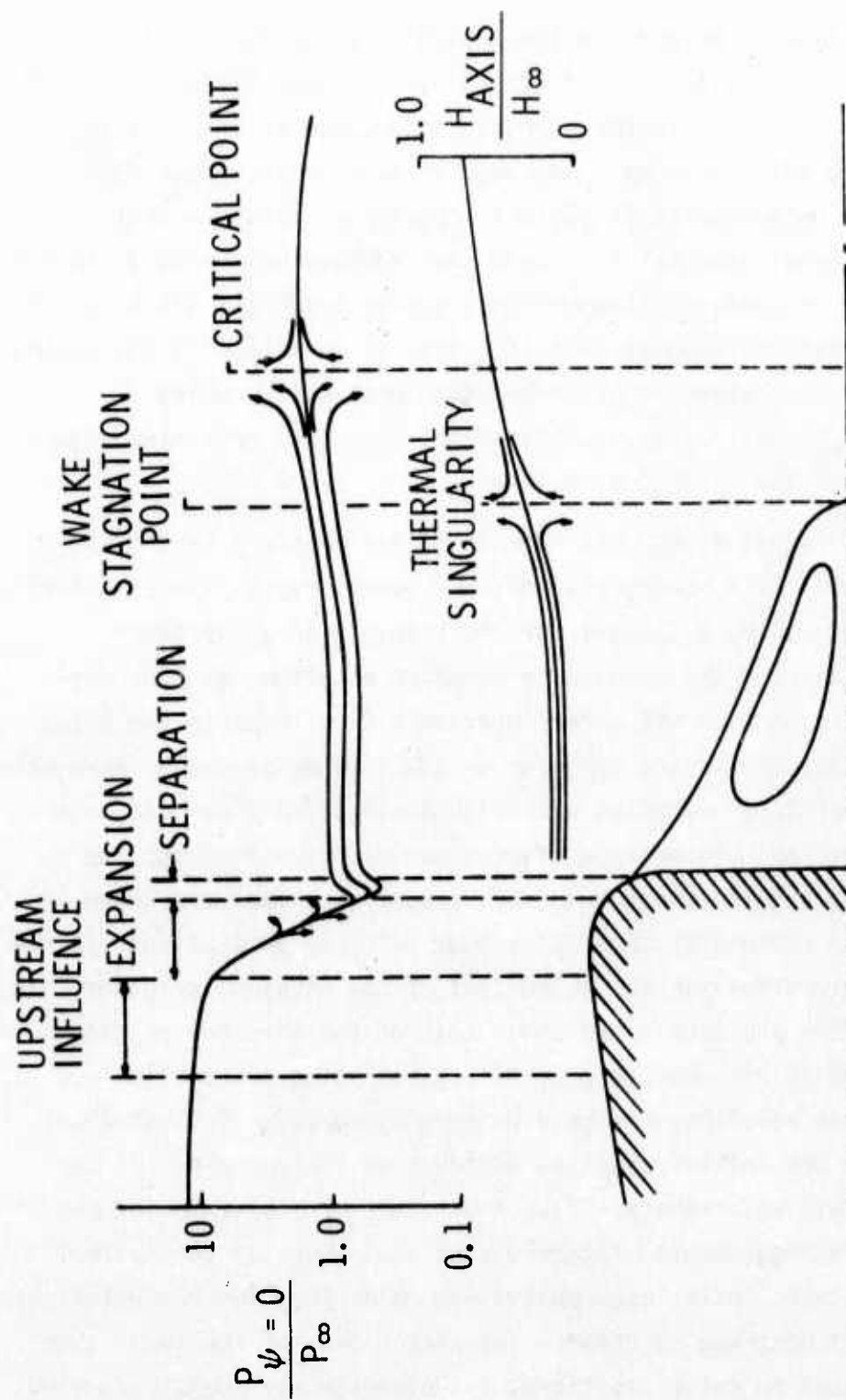


Figure 24. Qualitative Behavior of the Near Wake Solution

recirculation region is examined. Depending on the initial conditions, these solutions exhibit two types of behavior, neither of which is wake-like. One family of solutions is characterized by a centerline velocity which reaches a peak downstream of the recirculation region, then decreases until a second stagnation point is reached (the source solutions). The other is characterized by a rapidly accelerating rate of velocity increase on the centerline, with the calculation terminating as the rate approaches infinity (the sink solution). This behavior is due to the presence of a saddle point singularity in the wake neck region, and is depicted by the axis pressure distributions in the wake of the body shown in Figure 24. The singular solution which passes through the saddle point bounds the two non-wake families, and produces the only wake-like solution where the velocity on the centerline continues to increase downstream of the wake stagnation point. The role of this "wake critical point" in determining a unique base flow solution in a steady-state formulation has been thoroughly studied by a number of investigators, starting with Crocco and Lees.⁽⁷⁾ In the present problem, the unique separation solution and associated base pressure correspond to the wake solution which passes through the critical point.

The formulation also treats the flow within the recirculation region as an initial value problem, and this leads to an eigenvalue behavior of the solution for the thermal properties of the recirculation region. Clearly, the temperature of the recirculating flow near the base depends on heat transfer to the recirculation region further from the base. This upstream influence manifests itself in the form of a saddle point singularity at the wake stagnation point in the present initial value formulation (also depicted in Figure 24). The eigenparameter is the axis temperature near the base, and its proper value is that which yields a solution which passes through the singularity. The present formulation thus produces both the base pressure and recirculation region thermal properties during the course of the calculation for the body and flight conditions at hand.

The interacting boundary layer and near wake flow analysis applied here has been described in detail in several references.^(8,9) For this reason only a brief qualitative discussion will be presented here.

However, for completeness, a detailed description is presented in Appendix II.

The analysis divides the near wake flow into two regions which are, respectively, interior and exterior to a streamline which lies adjacent to the recirculation region and to the wake axis downstream of the recirculation region. The inner region is described by an integral method in which the conservation equations are integrated from the axis to the "matching streamline" separating the two regions. The outer region is described by a finite difference method, using conservation equations which retain both the inviscid terms and cross-streamline diffusion terms. A strict matching of essential flow properties is maintained between the two regions.

The equations governing the finite differences region are given in Appendix II. These same equations are used to calculate the boundary layer flow just prior to separation. Since these equations include only the cross-streamline diffusion terms, they can be applied only where streamwise diffusion would be unimportant. This excludes the application of the analysis to flows about sharp corners and hence some rounding of the aft shoulder of the vehicle is required. A rounding equivalent to five or six times the thickness of the subsonic portion of the boundary layer is normally imposed. The aft shoulder of the RMV-340 vehicle is already rounded (see Figure 2) and additional rounding is unnecessary. Artificial rounding of the aft shoulder of the small scale and full scale vehicle is required to the degree shown in the subsequent presentation of the results.

The governing equations are written in a coordinate system consisting of streamlines and normals to streamlines. This is a particularly appropriate coordinate system for the boundary layer-wake problem because of the large changes in flow direction experienced by the streamlines in the near wake region. It is because of this coordinate system that the results to be presented subsequently, are given along normals to streamlines in the outer flow, i.e. in the finite differences region.

5.1 TURBULENCE MODELING THEORY

The present initial value method is applicable to the turbulent near wake since the principle exchanges of momentum and energy via turbulence continue to occur normal to streamlines. The only new requirement is the addition of a method for determining the turbulent diffusivity. The classical method of replacing the laminar viscosity with an eddy viscosity based upon a mean flow velocity difference and a characteristic turbulence diffusion thickness is difficult to apply to the near wake. Regions of large shear in the turbulent near wake (such as the mixing layer and near axis wake downstream of the wake stagnation point) normally grow into the highly vortical remnant of the separated boundary layer thus making a consistent definition of the diffusion thickness difficult on the basis of mean flow profiles. In addition, the boundary layer remnant contains turbulence from the original attached boundary layer which interacts and influences the turbulence, and hence turbulent diffusivity, in the mixing layer and wake. The accounting for this effect and for the effect of large changes in pressure characteristic of the near wake requires a more detailed modeling of the turbulence (based upon consideration of the structure of the turbulence) than is provided by the classical technique.

The ability to predict the changing turbulence structure in the near wake lies within the framework of modern higher order theoretical analyses of non-homogeneous fully-developed turbulence which have appeared in the literature during the past several years. The turbulence is characterized by two independent variables often consisting of the turbulent kinetic energy due to the fluctuations, e , and a mean macroscopic or integral scale length of the turbulence, ℓ . The Reynolds stresses are usually represented by the product of an eddy diffusivity, which from dimensional arguments is proportional to $e^{1/2}\ell$, and a mean flow strain rate. The turbulence variables, and hence the eddy viscosity, are treated as field variables whose distribution depends on the mean flow and whose values are obtained from the solution of two diffusion-type equations which represent the convection, growth, decay, and diffusion of turbulence in the flow. Beginning with known mean flow and turbulence properties in the boundary layer before separation, this modeling permits accounting for a variety of effects such as the changing turbulent structure in the boundary layer remnant

during the expansion into the wake (including possible dissipative effects which have a tendency to relaminarize the remnant flow), the production of turbulence in the mixing layer and wake, the effect of the pressure rise across the shock waves on the turbulence, the influence of turbulence in the recirculation region, and the effect on the diffusivity of the strong pressure rise in the vicinity of the wake stagnation point.

The change in turbulent structure in the present analysis is based upon a model equation for the turbulent kinetic energy, e , and a second model equation for the dissipation rate of turbulence, $\epsilon_d = C_d e^{3/2} / \lambda$ where C_d is a constant. Modeled forms of the turbulent kinetic energy equation have been applied with reasonable success to a variety of flows by numerous investigators, beginning with Bradshaw.⁽¹⁰⁾ However, lesser experience exists in the application of the second turbulence equation. Consideration of several equations in comparative boundary layer calculations performed at TRW⁽¹¹⁾ showed the dissipation rate equation used here to yield the best agreement with the experiment.

The turbulence modeling theory used in the present analysis is being published in the open literature⁽⁹⁾ and is also described in Appendix II.

The analysis of the turbulent near wake requires the formulation of an integral theory for the turbulent properties within the recirculation region consistent with the integral theory describing the mean flow. Thus, integral forms of the turbulent energy and dissipation rate equations were developed for the region from the axis to the matching streamline, and profiles of the turbulence variables were assumed. These equations are solved in conjunction with the outer flow turbulence equations in a manner analogous to that used for the mean flow. Details of the integral analysis for the turbulence properties are presented in Reference 12.

5.2 IMPOSED CONDITIONS AND WAKE SOLUTION SUMMARY

The boundary layer profiles at the aft station of each vehicle presented in Section 4.1 were used to initiate the shoulder separation solutions. The velocity and temperature profiles from KBLIMP were spline fit to produce second order smooth profiles which could be used in the shoulder boundary

layer and wake analysis. This procedure is necessary because of the high resolution required to describe the shoulder and wake flowfields. In contrast to the 15 mesh points used to calculate the boundary layer on the vehicle, the shoulder and wake solutions required 150 mesh points. The latter lie on streamlines which are continuously followed.

The thermodynamic properties in the wake analysis are presently restricted to those of a perfect gas with constant specific heat and molecular weight. This proved to be an acceptable condition in the case of the full scale and small vehicles because the reacting boundary layer solutions displayed a convenient uniformity in specific heat and molecular weight across the boundary layer; a variation of about ten percent was noted. The largest changes in thermodynamic properties was observed to occur at the boundary layer edge. However, not accounting for this effect has little consequence on the near wake flow as will be discussed below. The RMV-340 vehicle displayed large variations in specific heat and molecular weight across the boundary layer. Since it is the flow near the wall in the boundary layer which fills the near wake directly behind the vehicle, the choice of thermodynamic properties was made from this portion of the boundary layer. The particular values of specific heat, molecular weight, and hence specific heat ratios, γ , used to obtain each solution are presented in Table 6.

The edge-of-boundary layer streamline was chosen as the outer domain of the calculation. This is permissible because in the present application the interest lies in the very near base region within one base diameter from the base. Here, the edge-of-boundary-layer streamline is turned only slightly by the expansion fan from the vehicle shoulder. In addition, the characteristics running inwards from this streamline lie at small angles to the streamline because of large Mach numbers associated with the "edge" flow. As a result of these effects, information from the edge streamline cannot propagate into the near base region to affect the subsonic base flow. It is therefore possible to impose as a boundary condition on the edge streamline an approximate relation between pressure and flow angle without affecting the near wake solution in the region of interest here. The Prandtl-Meyer relation valid for two-dimensional flow was imposed in the present cases.

A table which summarizes the input thermodynamic properties, and the eigenvalue parameters of base pressure, P_b , and non-reacting recirculation region gas temperature, T_b , obtained from the wake solutions for the five cases calculated here is given below. The uncertainty values for each eigenvalue reflects the degree to which the respective wake and thermal saddlepoint singularities were bracketed.

Table 6. Calculated Base Pressure and Non-reacting Recirculation Temperatures Region

Vehicle	Alt. (Km)	C_p (Cal/gm °K)	Mol.Wt.	γ	P_b (Atm)	T_b^* °K
Full Scale	5.92	0.334	27.2	1.282	.0497 \pm .0020	5084 \pm 83
Full Scale	4.58	0.332	27.7	1.278	.1200 \pm .0016	4628 \pm 94
Small	6.16	0.338	27.8	1.27	.0298 \pm .0015	3952 \pm 41
Small	4.54	0.338	27.8	1.27	.0399 \pm .0020	4048 \pm 51
RMV-340	25.0	0.362	22.8	1.32	.0079 \pm .0003	6560 \pm 80

*Reaction corrections to these non-reacting ideal gas temperatures are presented in Section 7.

Isotherms will be presented later to show the temperature distribution near the base in the recirculation region. The calculated values presented in Table 6 represent the temperature of the fluid returning to the vehicle base from that point in the recirculation region farthest removed from the base, i.e., from the wake stagnation point. The present analysis does not account for the base plate boundary layer. Consequently, the return flow temperatures calculated from the present theory are those that would exist at the edge of the base plate boundary layer, and for that matter over a considerable portion of the recirculation region close to the base.

6. WAKE PLASMA ANALYSIS

The electron density and temperature along streamlines from the boundary layer decreases rapidly as the pressure drops through the expansion into the wake. Electron generation ceases and electron decay begins primarily by three-body ion capture with a neutral particle as the third body. The three-body reaction time varies inversely with the rate constant, the ion concentration level, and the neutral species concentration, i.e., $\tau_{3B} = 1/k_{3B}[C_{M+}][C_X]$, while the near wake flow time of the expanding flow is $\tau_{ex} = D/V_\infty$, where D is the body base diameter and V_∞ the body velocity. The rate constant for three-body recombination is weakly dependent on temperature^{*}, and hence, the major effect of the expansion on the reaction time is through the reduction in concentration of the ion and neutral species. For vehicles with $D \approx 30$ cm and $V_\infty \approx 4,500$ m/sec, the near wake flow time is of the order of 10^{-4} sec. With temperatures reduced to 1200°K through the expansion to pressures of 0.05 atms, the three-body reaction time becomes $\tau_{3B} \approx 10^{-9}/f_{M+}$ where f_{M+} is the ion mole fraction. Thus, for the physically reasonable value of $f_{M+} = 10^{-6}$, the reaction time is ten times larger than the flow time. The loss of electrons in the near wake through three-body recombination is therefore expected to be a non-equilibrium process.

Other mechanisms for the depletion of electrons such as electron capture with O_2 , and by three body recombination with NO^+ are not important because of negligible concentrations of these species.

In contrast to the frozen like state of the electrons in the flow above the recirculation region, the chemical composition within the recirculation region is expected to be dominated by equilibrium chemistry. This becomes evident when the flow time is found by dividing the mass by the mass flux within the recirculation region, hence, $\tau_{fr} = \rho_r V_r / \dot{m}_r$ where V_r is the volume and ρ_r the density of the recirculation region. The mass flow may be approximated by the mass flow in the shear layer below the

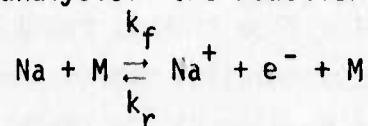
^{*}For three body recombination of Na, Jensen⁽¹³⁾ data suggests $k_{3B} = 1.5 \times 10^{-20} T^{-2} (\text{cm}^6/\text{part}^2/\text{sec})$

dividing streamline; thus $\dot{m} = 2\pi(D/4)(\delta/2)(V_\infty/4) \rho_r$ where D is the base diameter, δ is the shear layer thickness at the point where the dividing streamline is about half a base radius from the axis, V_∞ is essentially the velocity at the outer edge of the shear layer. It follows that $\tau_{fr} = (D/V_\infty)/(\delta/D)$, which says that the flow time in the recirculation region is longer by the ratio D/δ than the flow time in the outer wake. Since $\delta/D \approx 0.1$ (or less), the flow time for one cycle in the recirculation region is at least an order of magnitude longer. The flow times in the recirculation region and chemical times in the outer wake are therefore comparable. With the higher temperatures in the recirculation region, the chemical times are at least an order of magnitude shorter than the cyclic flow time in the recirculation region. The equilibrium condition thus appears to prevail in the recirculation region.

The diffusional interchange of momentum, energy, and species occurs between the outer expanding flow and the recirculation region in the shear layer. The shear layer temperatures are therefore larger than in the expanding flow which is in the direction of stimulating electron formation kinetics. However, the electron concentration level in the shear layer is more likely to be dominated by diffusion of electrons from the recirculation region assuming that the high temperatures associated with the recirculation region make it a strong source of electrons. Thus, because of the relatively cooler temperatures, the recombination kinetics are expected to prevail over the formation kinetics in part of the shear layer. This effect is not accounted for in the present analysis.

6.1 OUTER WAKE PLASMA EQUATIONS

The calculation of ion/electron concentration on streamlines from the boundary layer into the wake is performed on the basis of a one-dimensional or streamtube analysis. One reaction is assumed,



with rate constants determined from the experiments of Hollander⁽⁶⁾ and Jensen⁽¹³⁾ i.e.,

$$k_f = 1.2 \times 10^{16} T^{1/2} e^{-59,400/T} \left(\frac{\text{cc}}{\text{mole sec}} \right)$$

$$k_r = 54 \times 10^{26} / T^2 \frac{\text{cc}^2}{\text{mole}^2 \text{ sec}}$$

Let ϵ represent the degree of reaction and α the total atom mole fraction of Na; α is constant on streamlines since the major species constituency is assumed frozen on streamlines. Thus,

$$\epsilon = [\text{Na}^+] / ([\text{Na}^+] + [\text{Na}])$$

$$\alpha = ([\text{Na}^+] + [\text{Na}]) / n$$

where $[] \equiv \text{moles/cc}$ and n is the molar density of the gas mixture, i.e.,

$$n = P/RT$$

The change in the degree of reaction along a streamline is found from the streamtube expression,

$$\frac{d\epsilon}{ds} = \frac{n}{u} [k_f (\epsilon_e - \epsilon) - \alpha n k_r (\epsilon^2 - \epsilon_e^2)]$$

Here, ϵ_e is the degree of reaction under equilibrium conditions and is obtained from a solution to the equation

$$k_f (1 - \epsilon_e) - \alpha n k_r \epsilon_e^2 = 0$$

The rate constants depend on the local temperature and the molar density depends on the local temperature and pressure.

The above equations were solved numerically about the shoulder and in the wake for selected streamlines. The value of α and the initial values of ϵ were determined from the KBLIMP solutions for the Na^+/e^- concentrations in the boundary layer at the aft station of the bodies calculated. The electron concentration distribution in the outer wake is presented in a later section for each case, and is determined from the relation

$$n_{e^-} = \alpha n_e L \text{ (electrons/cc)}$$

where L is Avogadro's number.

6.2 RECIRCULATION REGION COMPOSITION

Determining the equilibrium composition in the recirculation region, which includes the electron density, requires specification of the elemental composition and two thermodynamic variables such as enthalpy and pressure. The consistent elemental composition is determined rather easily within the framework of the present analysis. The element continuity equations are obtained from the species continuity equation by summing the latter over all species containing the element, accounting for the appropriate element mass weighting within each species. Assuming then, equality for the diffusivity of all species (a reasonable assumption in turbulent flow), the element continuity equation has the form $\rho \vec{V} \cdot \nabla C_i = \nabla(\rho D_T \nabla C_i)$ where C_i is the mass fraction of element i (O, N, H, C, Na, etc. here), and D_T is the turbulent diffusivity. This equation does not contain source or sink terms since elements are neither created nor destroyed. In addition, it is identical in form to the total enthalpy energy equation (H replacing C_i) when the Prandtl number and Schmidt number are both one (also a reasonable assumption in turbulent flow). The boundary conditions for both variables H and C_i are also identical in the wake since their values along the original edge-of-boundary layer streamline are known and constant during the inviscid expansion into the wake, and the zero gradient wake boundary condition is applied to both variables along the axis. Diffusion, i.e., second derivative in the streamwise direction, is ignored in the analysis so only upstream initial conditions need be specified. A similarity thus exists between H and C_i of the form $C_i = aH + b$ where a and b are constants which can be evaluated from the initial wake profiles, i.e., from the boundary layer, and from the edge conditions. Thus

$$\frac{C_i - C_{iw}}{C_{ie} - C_{iw}} = \frac{H - H_w}{H_e - H_w}$$

where C_{iw} and H_w are wall values in the boundary layer at separation, and C_{ie} and H_e are known (and constant) edge values for the boundary layer and wake. Hence, the element composition is known in terms of the stagnation enthalpy in the recirculation region.

The near wake solutions produce values of temperature in the recirculation region, under non-reacting conditions. The non-reacting values are very high and are consequently unrealistic since considerable reaction would occur at these temperatures to decompose the assumed non-reacting gas constituency. In effect much of the heat predicted as sensible heat under the non-reacting gas assumption is absorbed by the reaction processes at the higher temperatures. A more practical approach to determining the recirculation region temperature is to use the non-reacting values of temperature to determine the static enthalpy of the gas mixture in the recirculation region. The constituency and temperature are then obtained by specifying the static enthalpy instead of the temperature in the equilibrium chemical analysis.

The static and stagnation enthalpies in the recirculation region are essentially equal since the recirculation region velocities are small, while the temperature is high. At the constant C_p conditions of the analysis, the enthalpy is found from the non-reacting gas temperature by the simple relation $H = C_p T + h_{ref}$. This relation also applies to the wall enthalpy, i.e., $H_w = C_p T_w + h_{ref}$. The edge-of-boundary-layer stagnation enthalpy, H_e , follows from the relation $H_e = C_p T_e + U_e^2/2 + h_{ref}$. Knowledge of H , H_w , and H_e allow for the determination of the element constituency. The reference enthalpy, h_{ref} , is not required since differences in enthalpy are required.

The reference enthalpy is needed in the chemical equilibrium analysis. As before the static enthalpy is written as $h = C_p T + h_{ref}$, but it is more convenient to split h_{ref} such that $h = C_p (T - T_{ref}) + h_{ref}^f$; the quantity h_{ref}^f refers to a chemical formation enthalpy at the reference temperature. The reference parameters, T_{ref} and h_{ref}^f , can be found from the reacting boundary layer solution. The atom constituency in the recirculation region also exists in the boundary layer at the end of the vehicle at that point where the ratio $(H - H_w)/(H_e - H_w)$ has a value equivalent to that determined

for the recirculation region from the wake solution. The temperature and chemical formation enthalpy at this point are the desired reference parameters, and are directly obtainable from the KBLIMP solutions. This procedure is followed for all cases and comparison of the electron concentration levels under conditions of frozen major species composition and using the enthalpy approach discussed here will be presented.

6.3 COLLISION FREQUENCY

The electron-neutral collision frequency is important to the transmission of electromagnetic signals through the base region, and so distributions of this quantity will be presented for each case. Following the arguments and discussion presented in Appendix III, a formula recommended by Baskett⁽¹⁴⁾ is used in present analysis. It has the form

$$\nu_{\text{eff}} = 3 \times 10^{11} p(\text{atm}) (\text{sec}^{-1})$$

The uncertainty in this relation is a factor of 3 in either direction. However, the value of 3×10^{11} chosen for the coefficient does match recent experimental results obtained from transmission measurements through an ionized portion of the wake of ablating conical projectiles fired under simulated reentry conditions.

7. WAKE FLUID MECHANICS AND PLASMA RESULTS

Results of the wake and plasma calculations for the full scale vehicle and the small vehicle are summarized here. The RMV-340 vehicle will be discussed in Section 8.

7.1 FULL SCALE VEHICLE WAKE RESULTS

The streamline which bounds the recirculation region and seven streamlines representing the flow of the boundary layer into the wake are presented for the full scale vehicle for the 5.92 km altitude condition in Figure 25. These results show how streamlines from the innermost portion of the boundary layer turn to fill the region immediately behind the base, while the outer streamlines turn more gradually. The outermost streamline shown is the original edge-of-boundary layer streamline. A line denoted as a "minimum pressure line" crosses many of the streamlines and represents the lateral extent of the influence of the inner flow on the expanding boundary layer. The pressure along streamlines crossing this line subsequently rises. Two isotherms are shown in the recirculation region to illustrate the near constant temperature zone near the base. The values of temperature shown are corrected for chemical reactions.

The distributions of pressure along the designated contours, which are normal to streamlines, are presented in Figure 26. Station 1 refers to the initial constant pressure profile across the boundary layer just upstream of the shoulder. Station 2 corresponds to the position of separation of the boundary layer from the shoulder. The remaining stations are in the wake. The streamline which bounds the recirculation region is called the dividing streamline (DSL). Properties given in the figures at DSL and AXIS refer to axial locations lying directly below the intersection of Streamline A and the normal contour at the station at hand. The pressure decrease along the outer streamlines as Stations 1 through 6 are traversed is evident. In contrast, the pressure on the inner region of the flow is nearly constant from Stations 2 through 5 but has undergone a large increase at Station 6.

Analogous temperature profiles are shown in Figure 27. The temperatures along the outer streamlines decrease through the expansion. However, at Stations 3 through 5 the temperature increases inward of Streamline B because of the "hot" recirculation region and shear layer. The increased pressure on the inner streamlines at Station 6 (Figure 28) leads to a corresponding temperature increase. The temperatures on the DSL and AXIS shown in Figure 27 are the consistent non-reacting gas temperatures in contrast to those shown in the flowfield map which are "corrected" for reacting gas effects.

The electron concentration distributions for the streamlines only are given in Figure 28. Values in the recirculation region will be presented separately. A strong decrease in electron concentration is observed to occur in the wake due primarily to the decrease in density. The concentration reaches a constant value of about 4.5×10^{11} particles/cc at Stations 3, 4, and 5 along Streamline B. The values shown for Streamline A are anticipated to be low because the analysis does not account for an increased concentration due to diffusion from the recirculation region. Thermal diffusion effects from the recirculation region are evident on Streamline A in Figure 25, and species diffusion processes are comparable.

The collision frequency distributions are shown in Figure 29. The results are qualitatively the same as those for pressure. The flowfield map, electron concentration distributions, and collision frequency distributions are presented in Figures 30, 31, and 32, respectively, for the full scale vehicle at 4.58 km. These results are qualitatively the same as those discussed at the higher altitude.

7.2 SMALL VEHICLE WAKE RESULTS

The flowfield map, and pressure and temperature distribution in the boundary layer and wake of the small vehicle at 6.16 km altitude are presented in Figure 33, 34, and 35, respectively. Both the temperature and pressure values in the expanding flow and recirculation region are significantly lower than those observed for the full scale vehicle at the comparable altitude. The pressure in the recirculation region near the base is about 0.03 atms compared to 0.05 atms for the full scale vehicle.

The outer streamline temperatures lie in the range from 800 to 1200⁰K for the small vehicle, and from 1200⁰K to 1700⁰K for the full scale vehicle. The recirculation region temperature is also larger for the full scale vehicle (4400⁰K compared to 3260⁰K).

The electron wakes of the small vehicle were studied for three heat-shield sodium seeding levels corresponding to a nominal value of 50 ppm and two intentional values of 500 and 1000 ppm. The electron concentration distributions through the boundary layer and in the wake for these three cases are shown in Figure 36. Increasing the seeding level by a factor of 10 and 20 leads to an increase in electron concentration in the boundary layer of slightly over 3 and 4, respectively. The increase thus appears to scale with the square root of the seeding level. For the outer streamlines (B through F), the full scale vehicle produced from 10^{11} to 10^{12} electrons/cc and this appears to be reasonably reproduced by the small vehicle only at a seeding level of 1000 ppm. A seeding level of between 1500 and 2000 ppm would bring them into closer agreement on the basis of a square root scaling.

The collision frequency distributions for the small vehicle are presented in Figure 37. The values appear to lie about a factor of 1.5 to 2 lower than those of the full scale vehicle in comparable regions of the flow.

The flowfield map, electron concentration distributions at three seeding levels, and the collision frequency are presented in Figures 38, 39, and 40, respectively, for the small vehicle at 4.54 km altitude. A comparison of these results with those for the full scale vehicle at 4.58 km leads to conclusions analogous to those for the comparison at the higher altitude.

7.3 RECIRCULATION REGION ELECTRON CONCENTRATIONS

Interpreting the wake thermal solutions in terms of enthalpy rather than directly as temperature, as outlined in Section 6.2, has two effects. The recirculation region temperature is decreased, and ionization of species other than sodium may contribute to the electron concentration. Table 7 shows the temperature change resulting from the reaction correction for each case.

Table 7: Reacting Gas Temperature Correction

Vehicle	Alt (KM)	Temperature	
		Non-Reacting	Reacting
Full Scale	5.92	5084 ⁰ K	4400 ⁰ K
Full Scale	4.58	4628 ⁰ K	3870 ⁰ K
Small	6.16	3952 ⁰ K	3260 ⁰ K
Small	4.54	4048 ⁰ K	3240 ⁰ K

The temperature decrease due to reaction chemistry is seen to be in the range of 700 to 800⁰K. This effect influences the electron concentration due to sodium ionization in two opposing ways. Decreasing temperature increases the overall particle concentration, but can decrease the degree of the ionization reaction. In Figure 41, the electron concentration in the recirculation region is shown for the full scale and small vehicles for the higher altitude case studied. The non-corrected points represent sodium ionization at the non-reacting gas temperature. For the small vehicle with 50 ppm Na, the ionization reaction is complete ($\epsilon_e \approx 1$) and the reaction correction has the effect of increasing the electron concentration slightly. However, with 500 and 1000 ppm Na, the effect of reducing temperature is to reduce the degree of reaction, with the net effect of reducing the electron concentration.

Applying the reaction correction to the full scale vehicle has the effect of introducing a new source of electrons from the ionization of NO. The contribution due to NO⁺ is, in fact, about 2.5 larger than the Na⁺ contribution.

The results of Figure 41 show that electron levels comparable to those in the recirculation region of the full scale vehicle are achievable for the small vehicle at seeding levels below 500 ppm Na.

Analogous results for the full scale and small vehicles occur at the lower altitude studied as is demonstrated in Figure 42.

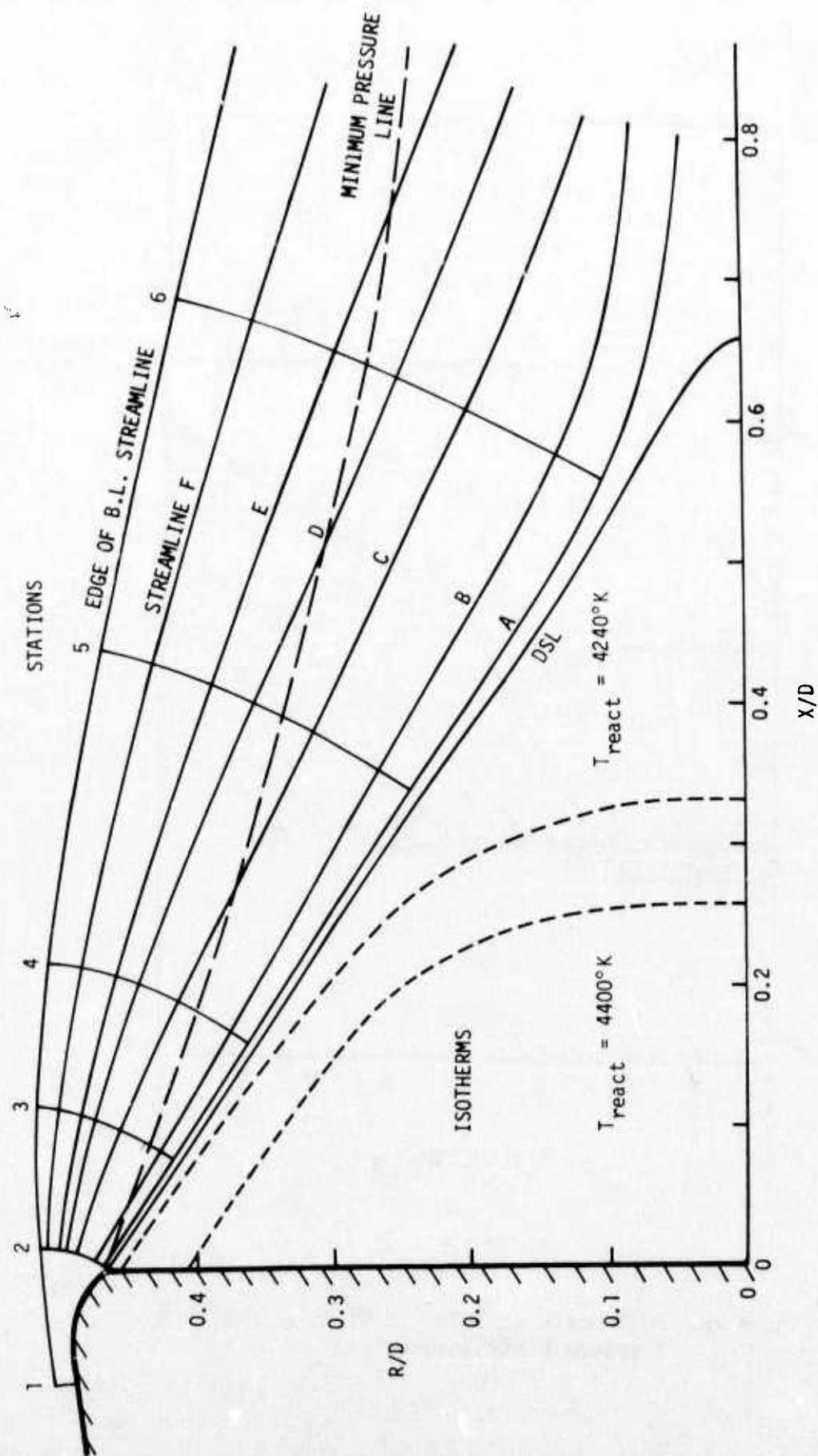


Figure 25. Full Scale Vehicle - 5.92 Km - Near Base Flowfield

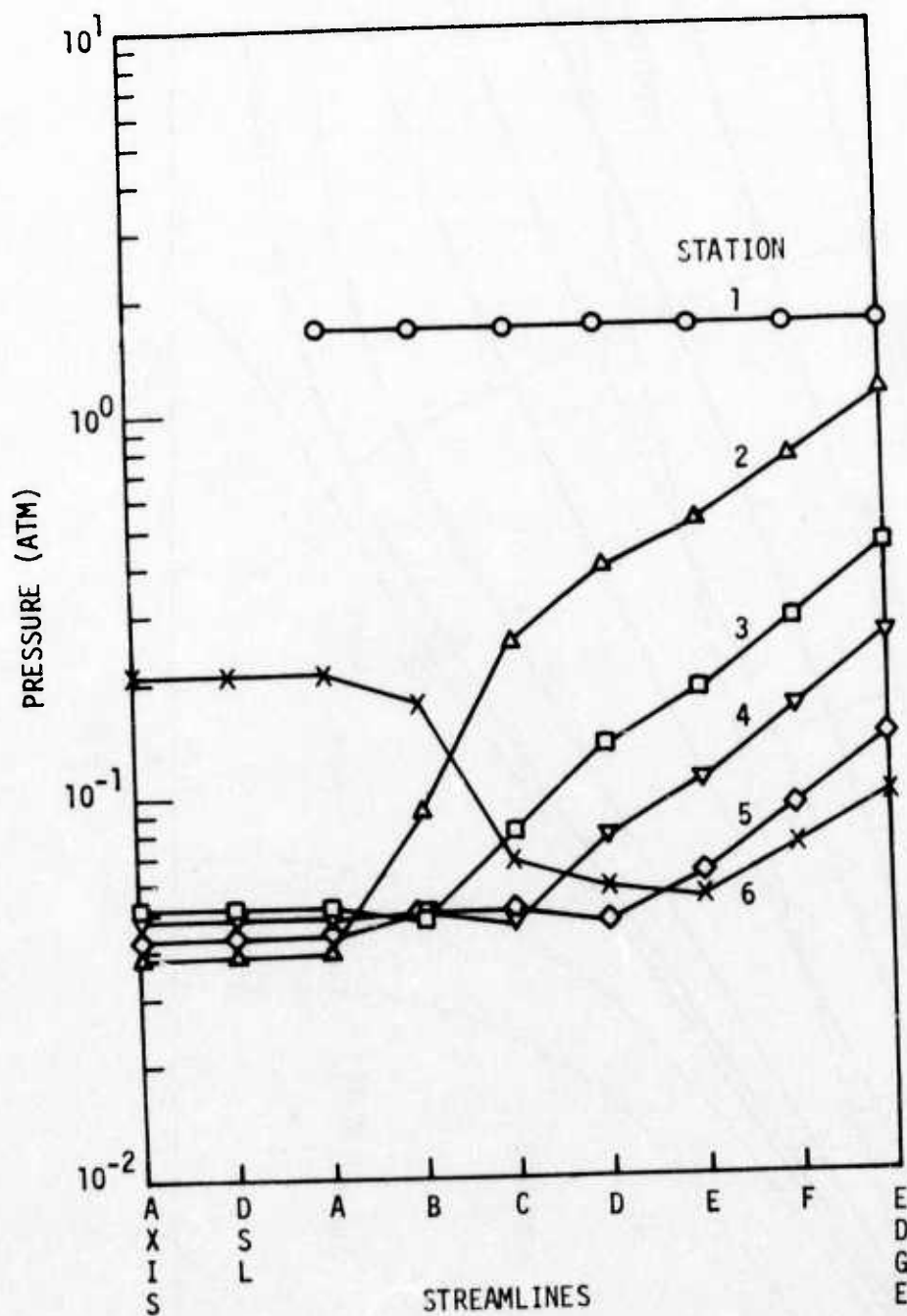


Figure 26. Full Scale Vehicle - 5.92 Km - Near Base Pressure Distributions

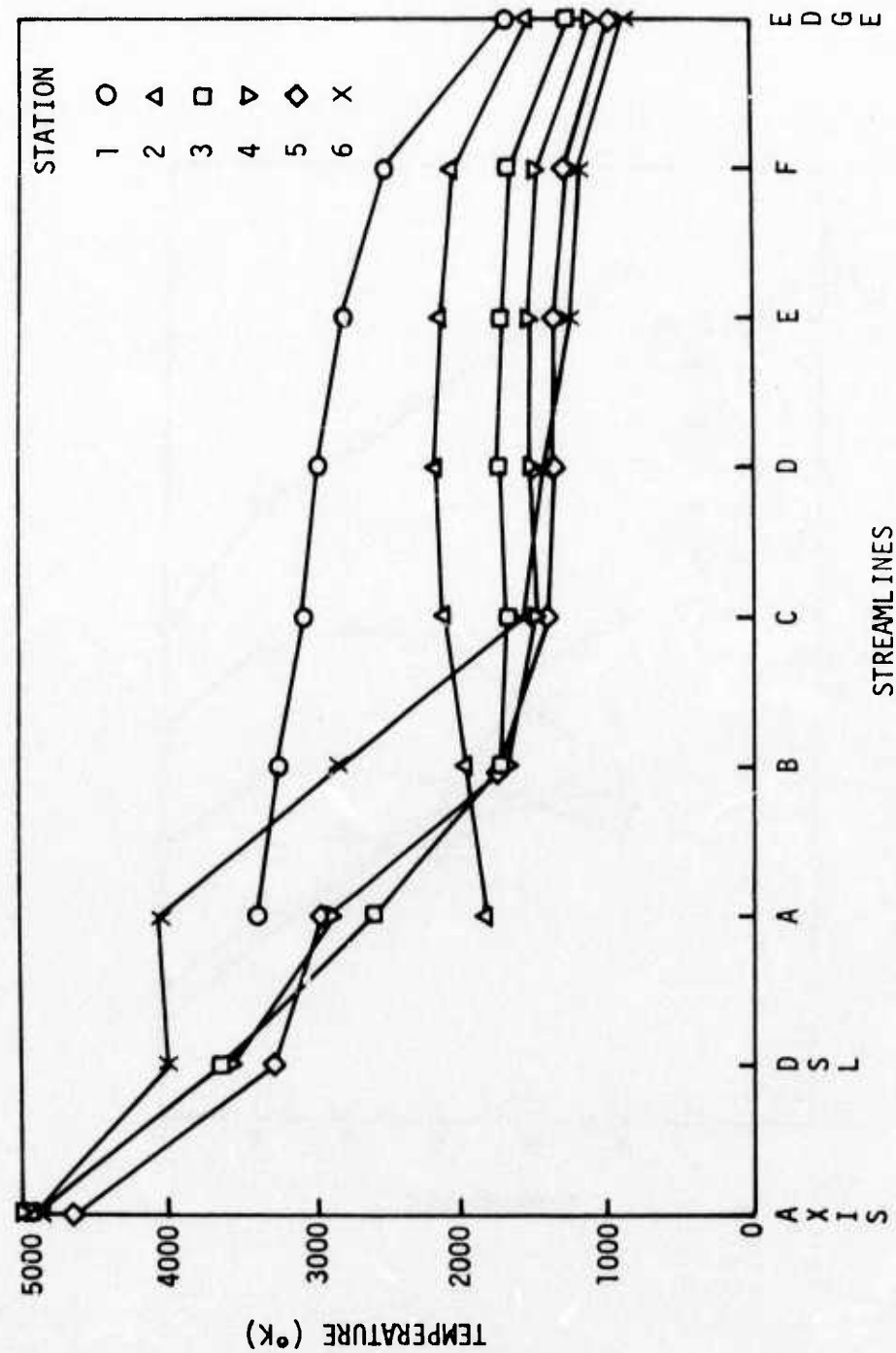


Figure 27. Full Scale Vehicle - 5.92 Km - Near Base Temperature Distributions

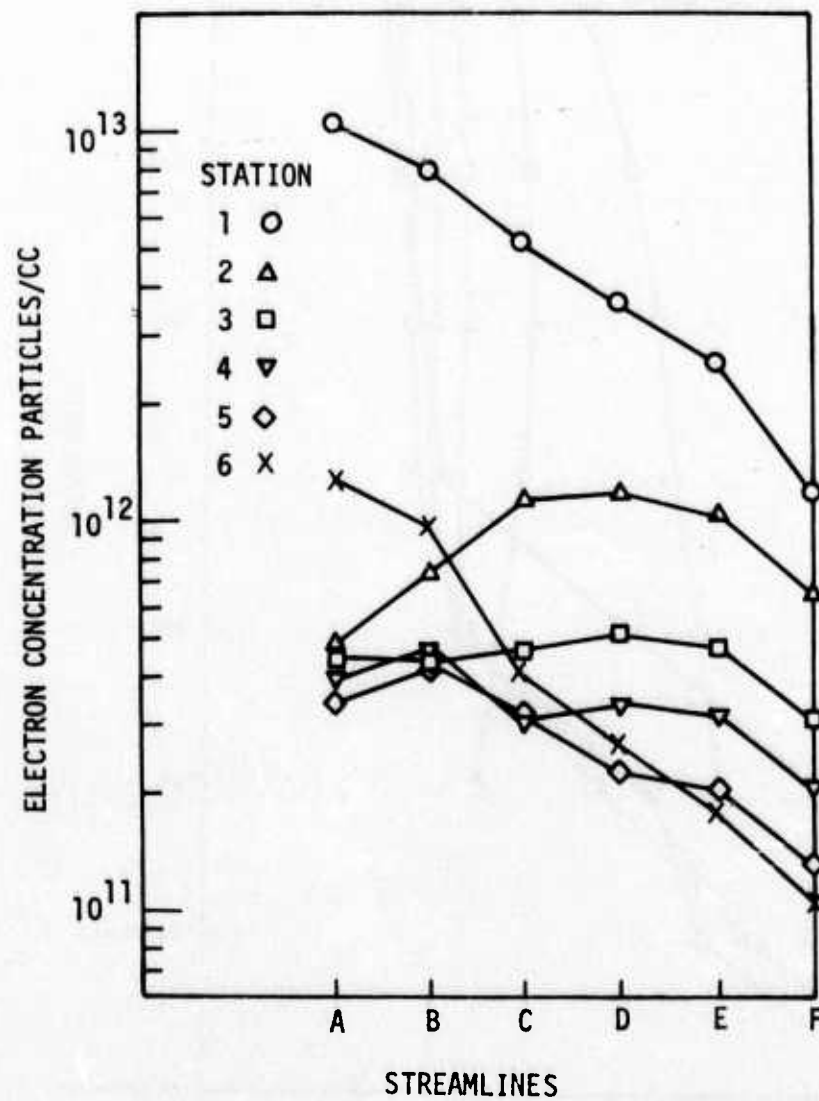


Figure 28. Full Scale Vehicle - 5.92 Km - Near Base Density Distribution - Outer Flow Region

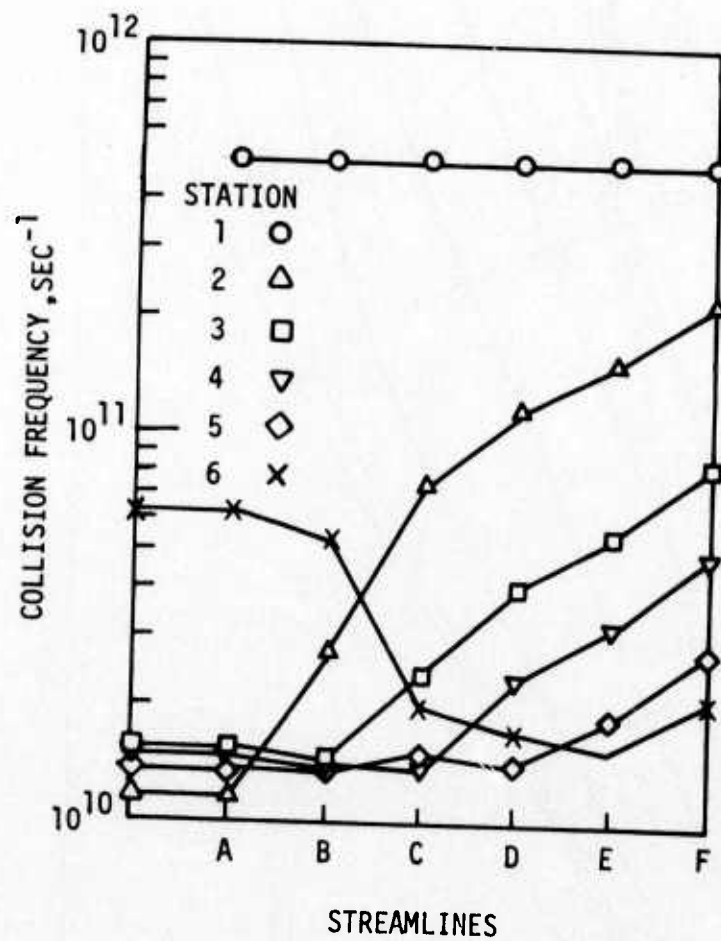


Figure 29. Full Scale Vehicle - 5.92 Km - Near Base Collision Frequency Distribution

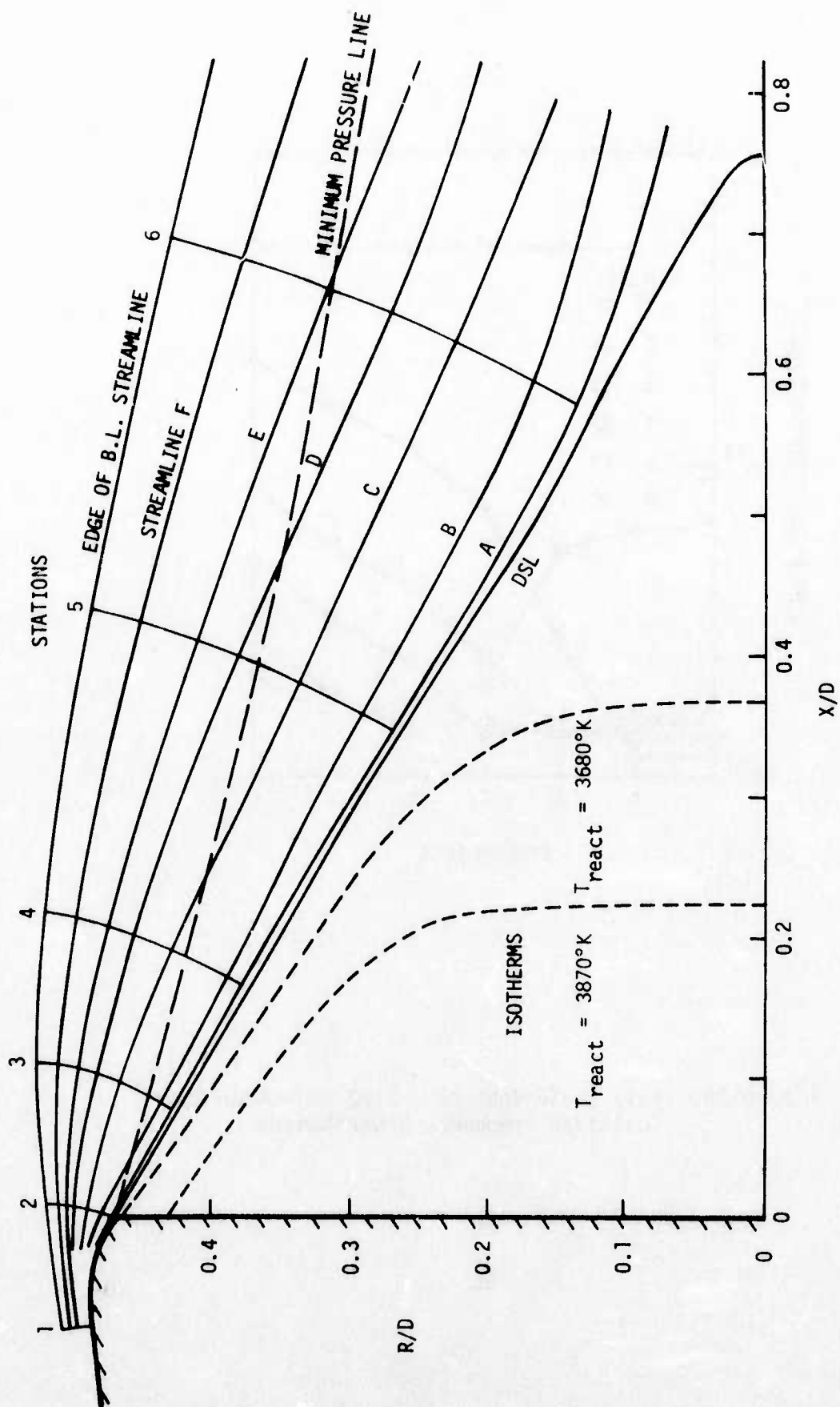


Figure 30. Full Scale Vehicle - 4.58 Km - Near Base Flowfield

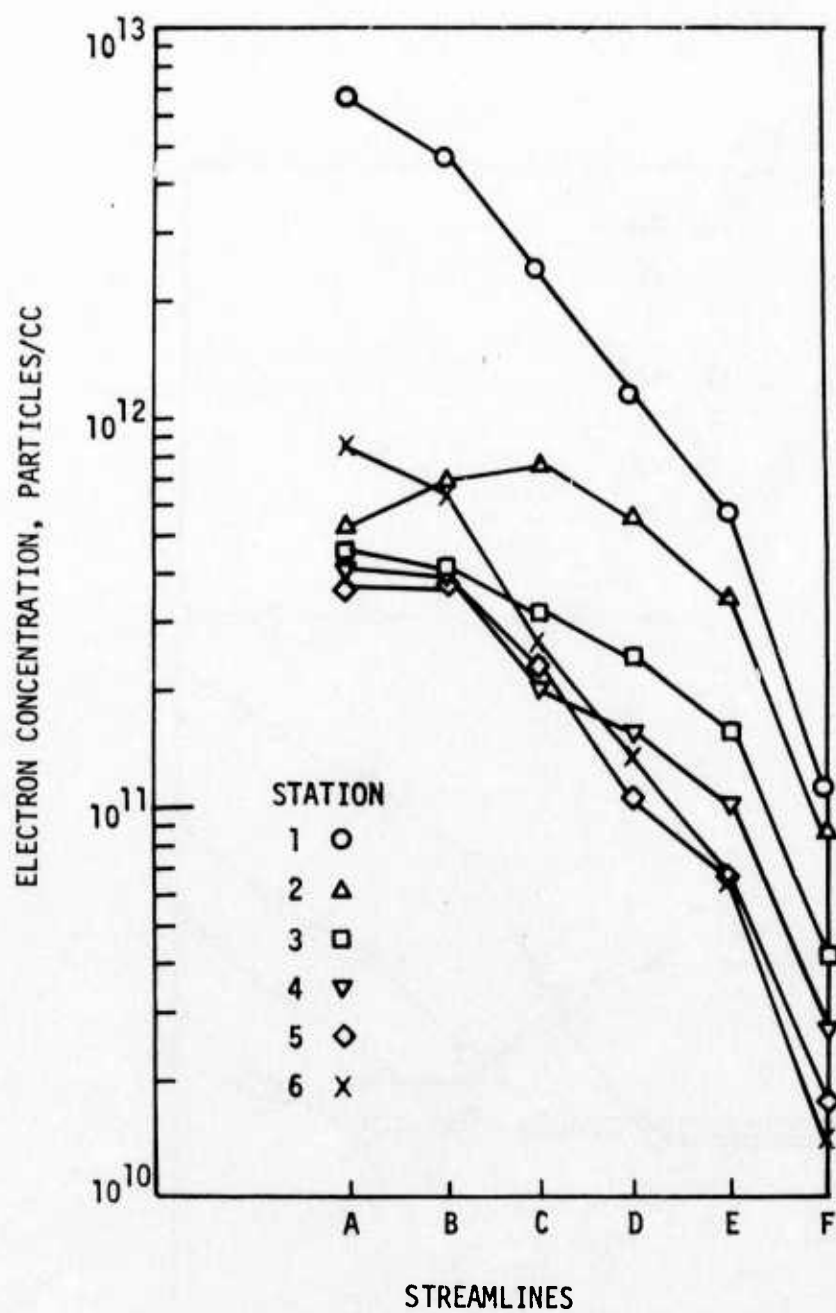


Figure 31. Full Scale Vehicle - 4.58 Km - Near Base
Electron Density Distributions -
Outer Flow Region

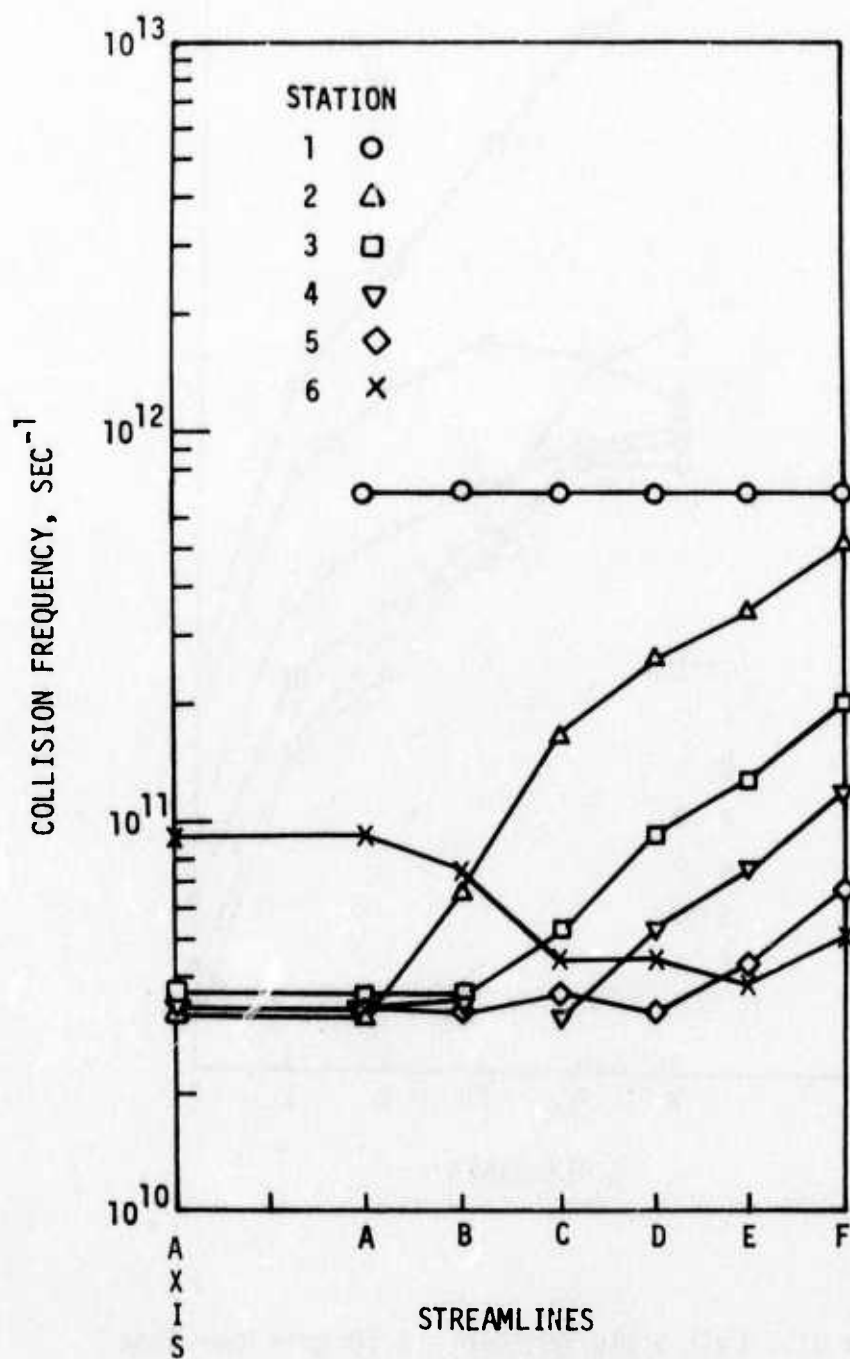


Figure 32. Full Scale Vehicle - 4.58 Km - Near Base Collision Frequency Distributions

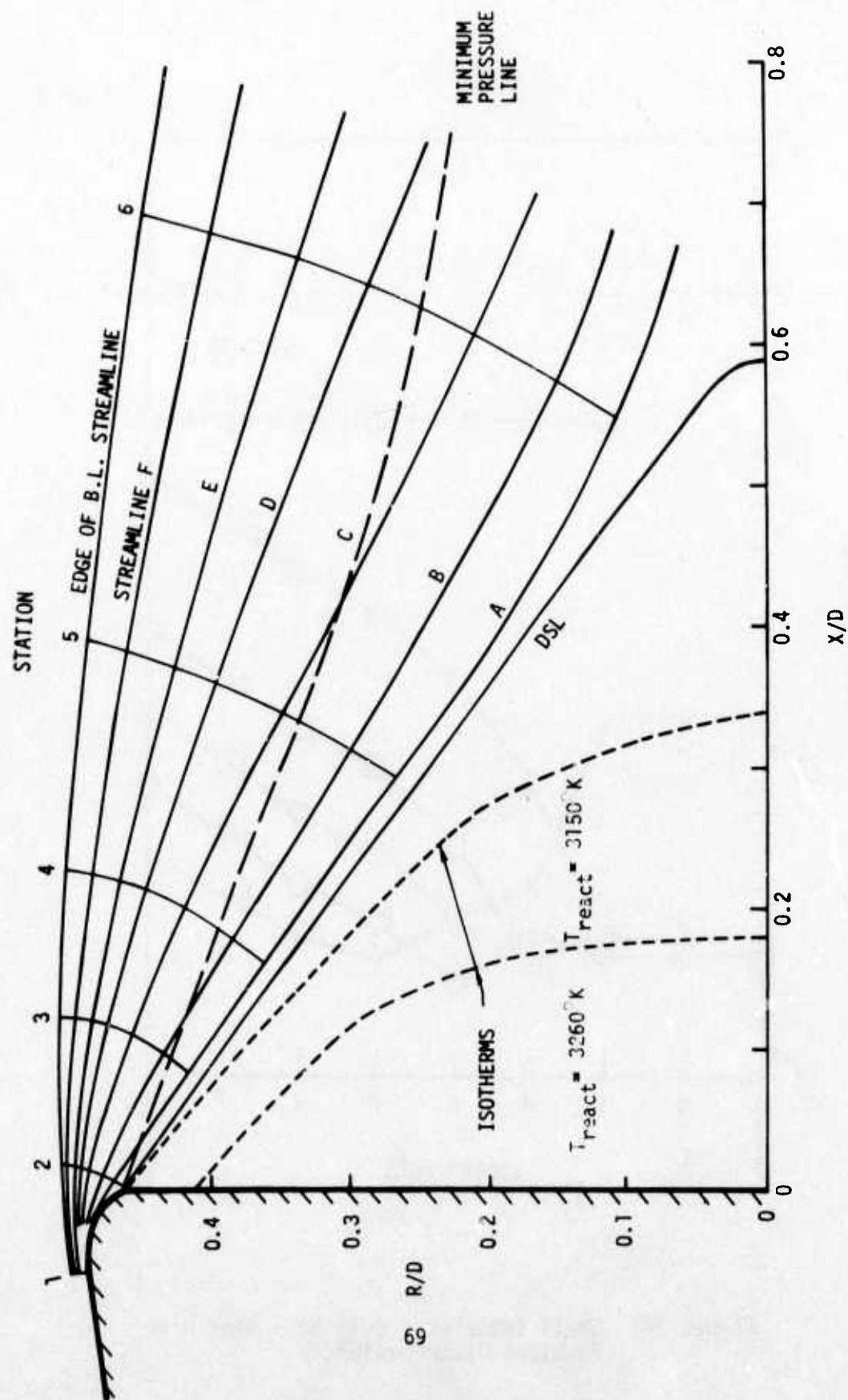


Figure 33. Small Vehicle - 6.16 km - Near Base Flowfields

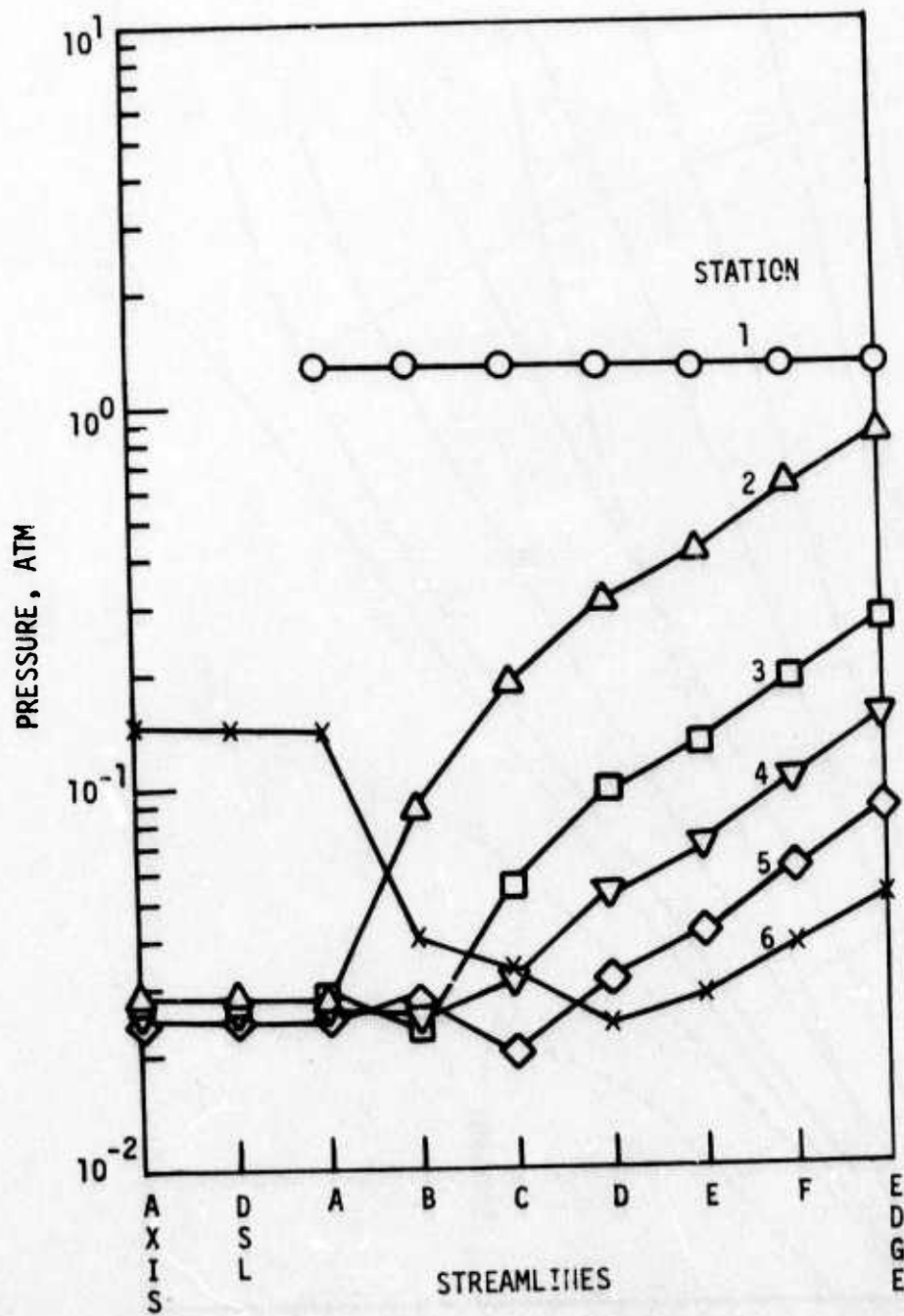


Figure 34: Small Vehicles - 6.16 km - Near Base Pressure Distributions

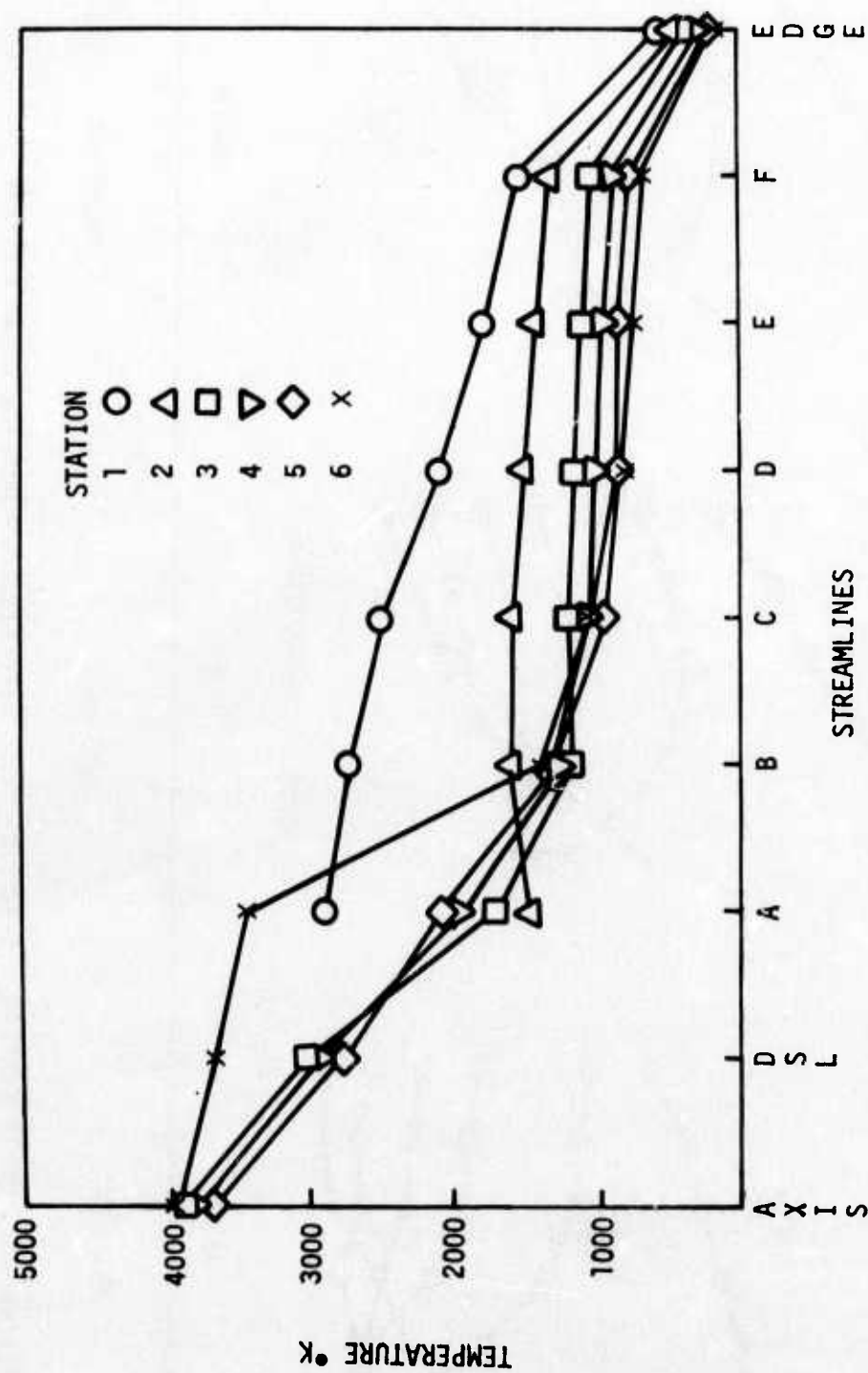


Figure 35: Small Vehicle - 6.16 km - Near Base Temperature Distributions

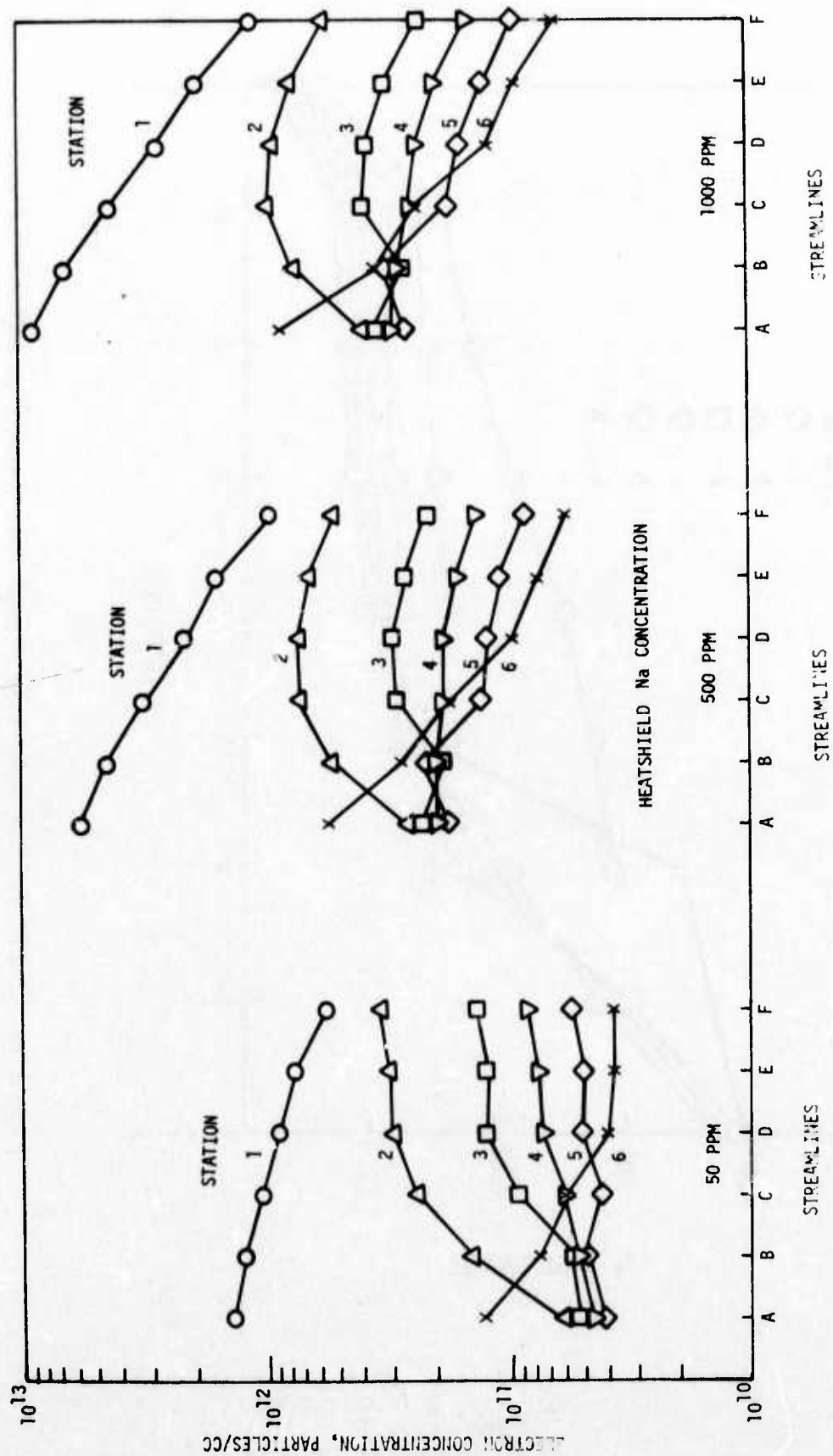


Figure 36: Small Vehicle - 6.16 km - Near Base Electron Density Distributions
Outer Flow Region

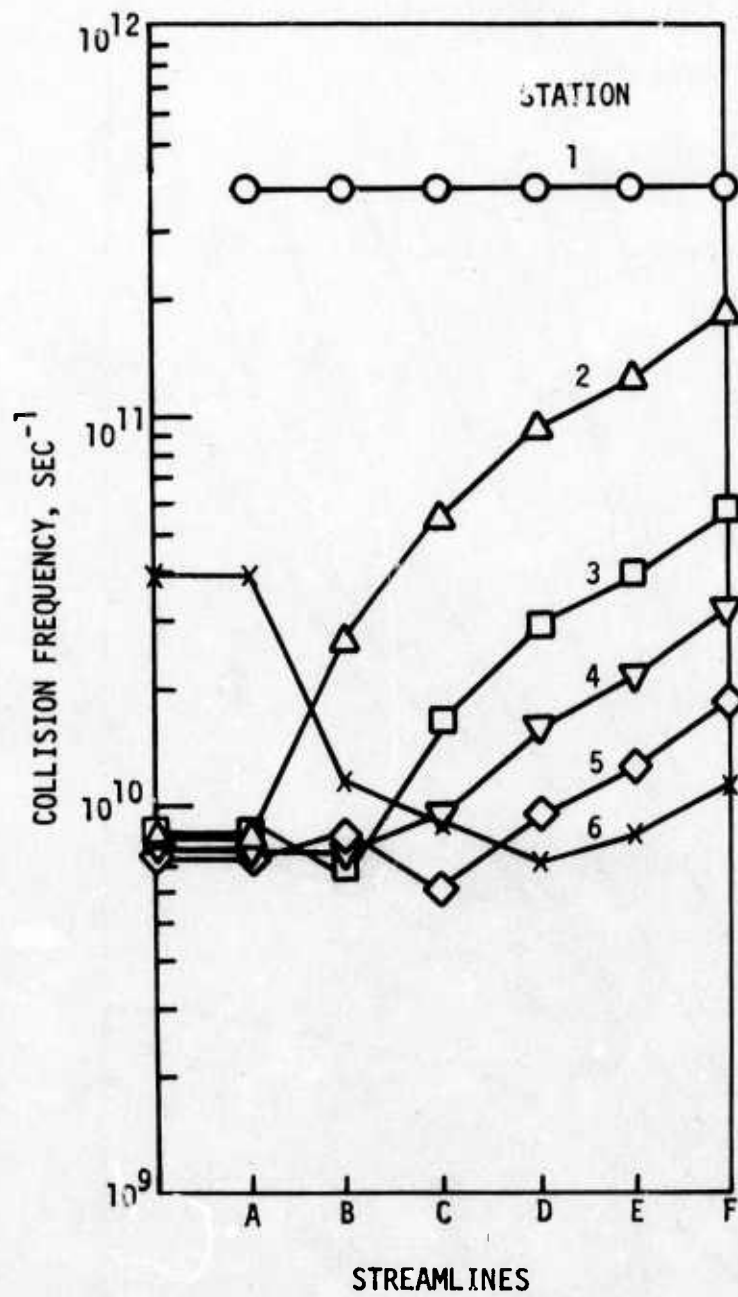


Figure 37: Small Vehicle - 6.16 km - Near Base Collision Frequency Distribution

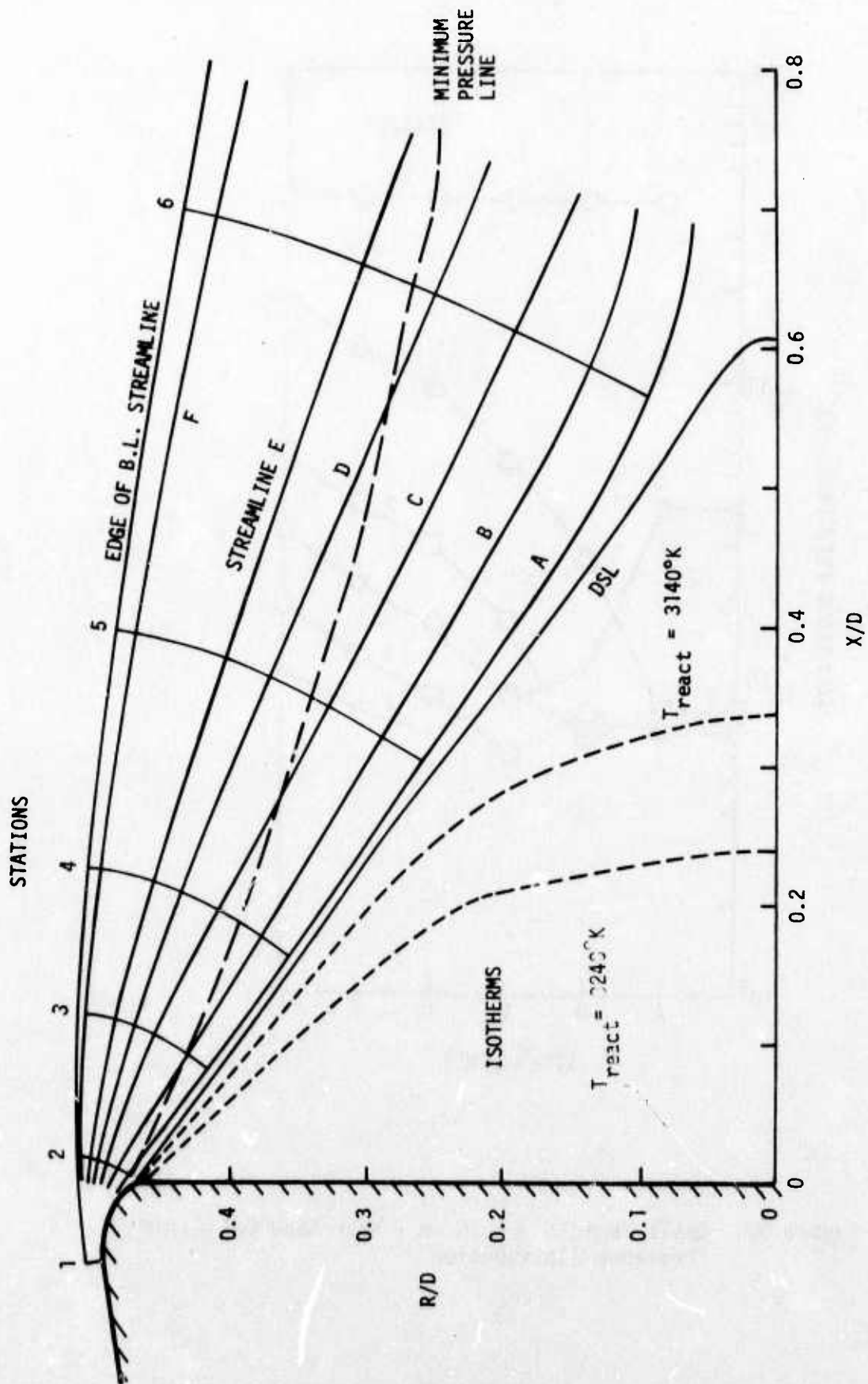


Figure 38: Small Vehicle - 4.54 km - Near Base Flowfield

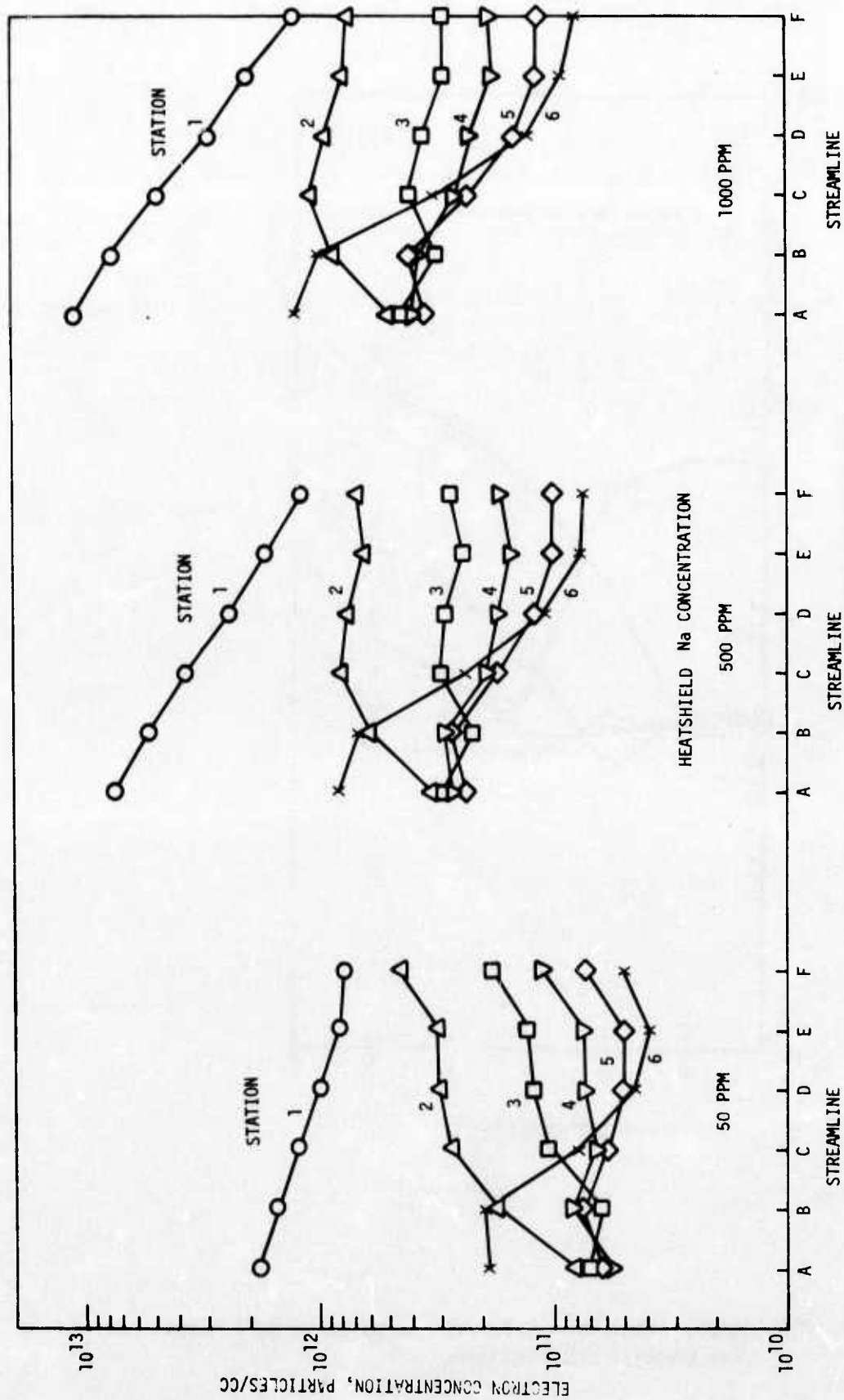


Figure 39: Small Vehicle - 4.54 km - Near Base Electron Density Distributions
Outer Flow Region

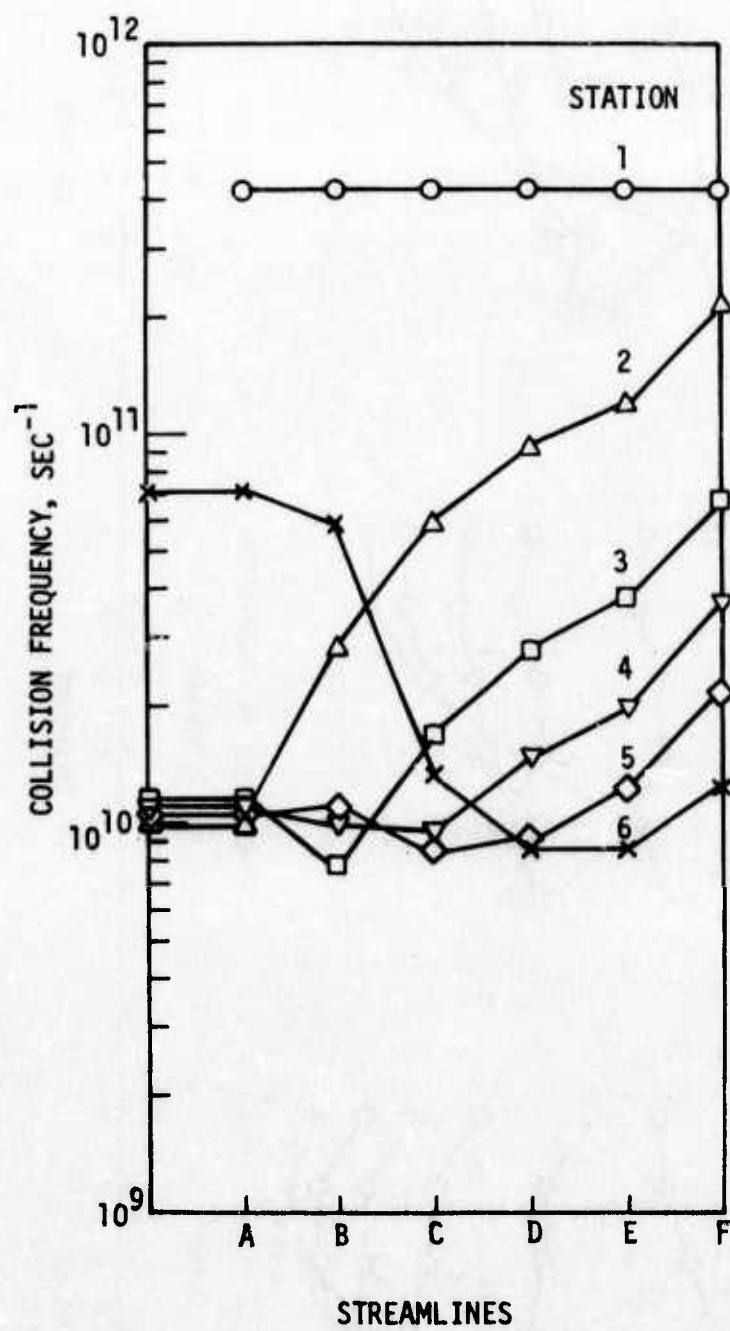


Figure 40: Small Vehicle - 4.54 km - Near Base Collision Frequency Distributions

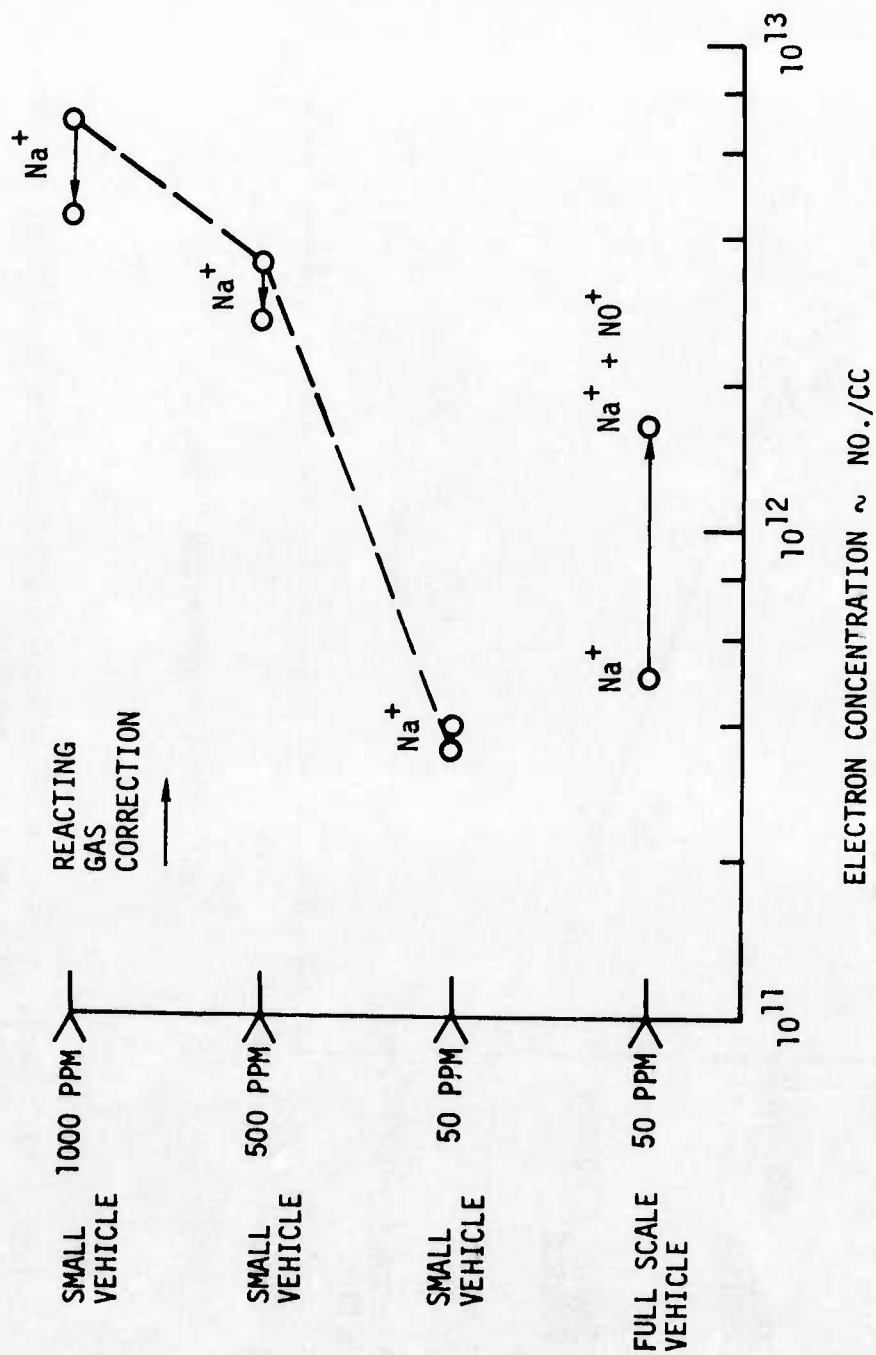


Figure 41. Recirculation Region Electron Density - 6 km Nominal Altitude - Full Scale and Small Vehicles

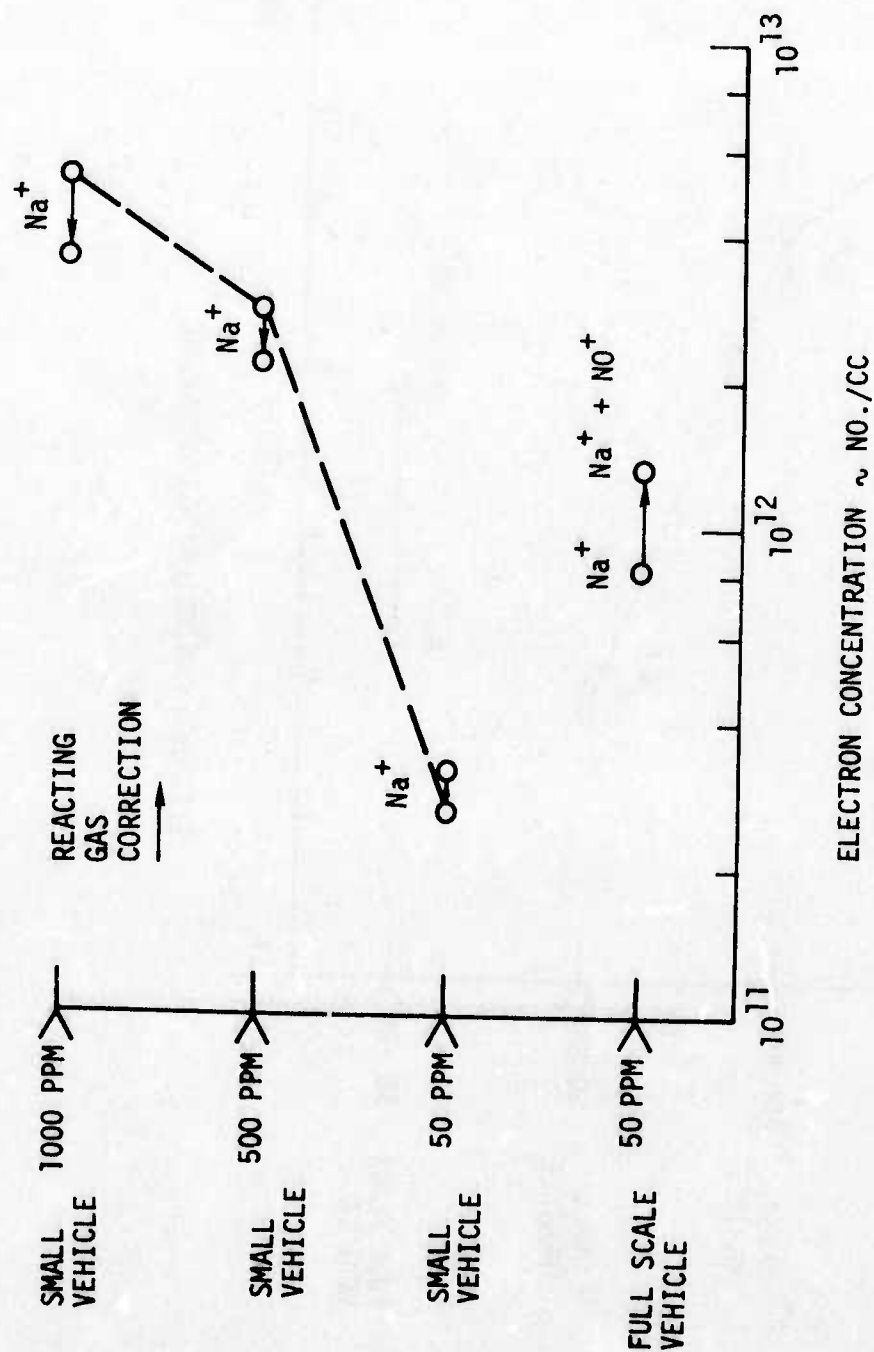


Figure 42. Recirculation Region Electron Density - 4.6 km Nominal Altitude - Full Scale and Small Vehicles

8. COMPARISONS WITH FLIGHT MEASUREMENTS

The purpose of analyzing the RMV-340 vehicle was to provide some basis for evaluating the accuracy of the analysis performed for the other vehicles. A series of RMV-340 vehicles were flown under the Reentry Measurements Program, Phase B (RMP-B) sponsored by the Advanced Ballistic Missile Defense Agency. These vehicles were highly instrumented to obtain a variety of in-flight data. The particular experiments of interest here are those in which measurements were obtained for the ion and electron densities in the vicinity of the base plate on the vehicle base. These densities were deduced from currents measured with two types of electrostatic probes placed on stings away from the base. Data were obtained on five flights, four of which maintained very small angle of attack histories. Vehicles were flown with Teflon, silica phenolic, and beryllium heatshields. Silica phenolic is most similar to carbon phenolic in its ablation characteristics and in the subsequent boundary layer combustion chemistry. For both the silica and carbon phenolic heatshields, the electron generation is due to ionization of contaminant "low ionization potential" metals and not to hydrocarbon combustion. The silica phenolic vehicle was thus chosen for analysis here. Valid data was obtained on one silica phenolic flight.

In addition to the base electrostatic probe experiment, the peak ion density in the boundary layer was deduced from an electrostatic probe located on the frustum near the aft end of the vehicle. A comparison of the predicted ion density from the reacting boundary layer analysis will be made with the flight deduced value. The base pressure was also measured throughout the flight and will provide a basis for evaluating the fluid mechanics solution.

8.1 WAKE RESULTS FOR THE RMV-340 VEHICLES

The flowfield map, and pressure, temperature, electron density and collision frequency distributions calculated for the RMV-340 vehicle at 25 km altitude are presented in Figures 43 through 47 respectively. Because of the relatively larger velocity of this vehicle, recirculation region

temperatures are considerably larger than for the full scale and small vehicles presented earlier. The non-reacting recirculation region temperature is 6560°K and with reaction is reduced to 4460°K. Under these conditions the ionization of atomic silicon dominates completely over that of sodium. The predicted electron density for silicon ionization is $n_{Si^+} = 2.2 \times 10^{13}$ electrons/cc and the contribution from sodium is $n_{Na^+} = 6.5 \times 10^{11}$ electrons/cc and from NO^+ is $n_{NO^+} = 9.0 \times 10^8$ electrons/cc.

The predicted base pressure is 0.0079 ($\pm .0003$) atm. The base pressure to ambient pressure ratio is $p_b/p_\infty = 0.316 \pm .013$.

8.2 FLIGHT MEASUREMENTS

Seven electrostatic probes were located on the base plate of the silica phenolic vehicle. Three were spherical probes and four were long cylinder probes. Some geometrical specifics of the probes and their location on the base plate is shown in Figure 48. Also shown on separate plots are the electron concentration values deduced from the two types of probes in the altitude range from 35 to 20 km.⁽¹⁵⁾

It is apparent from Figure 48 that the cylindrical probes yielded positive ion densities that are over an order of magnitude larger than for the spherical probes at 25 km altitude. A reason for this discrepancy was not offered in the data evaluation report.⁽¹⁵⁾ However, the four cylindrical probes were in close agreement or displayed accountable differences throughout the entire flight. In contrast, some anomalous behavior for one of the sphere probes was noted during the flight. However, the other two spherical probes were in good agreement with one another throughout most of the flight. The predicted ion concentration level from the present analysis is shown on both data plots in Figure 48. The agreement with the cylindrical probe results is good.

Positive ion densities in the boundary layer deduced from electrostatic probe measurements are presented in Reference 16 for the RMV-340 vehicle with a silica phenolic heatshield. The value obtained at the 25 km altitude at a station just preceeding the aft shoulder is 4×10^{12} particles/cc. The present boundary layer analysis predicted an ion density of 1.7×10^{13} , attributable primarily to sodium ionization. Thus, the prediction is about a factor of 4 high. This comparison has no influence on the comparison of

the predicted and deduced base probe results discussed above. Ion levels in the recirculation region near the base are dominated by the ionization of silicon, and do not depend on the ion/electron concentration in the boundary layer at the shoulder. Boundary layer ionization does influence the outer region ion/electron densities, and if the predicted boundary layer values are high, then so will be the predicted outer flow values (Figure 46).

A summary of base pressure data for these flights was presented by Batt.⁽¹⁷⁾ His results for the vehicle with a silica phenolic heatshield are repeated in Figure 49. The data were taken by several pressure gages whose range variation was 0.1, 1.0, and 2.0 psia. These gages were located at three radial positions on the base ($r/R_b = 0, 0.36, \text{ and } 0.46$). The Reynolds number based on vehicle length for the present calculation is $Re_{\infty,L} = 8 \times 10^7$ and the predicted base pressure of $P_b/P_{\infty} = 0.316 \pm .013$ has been included in Figure 49.

The predicted base pressure lies between the measured base pressures at $r/R_b = 0.36$ and $r/R_b = 0.46$. The present wake theory assumes a constant "average" base pressure, whose value must correspond to the actual base pressure at radii well removed from the axis. The agreement of the prediction with the flight measurement appears to be very good.

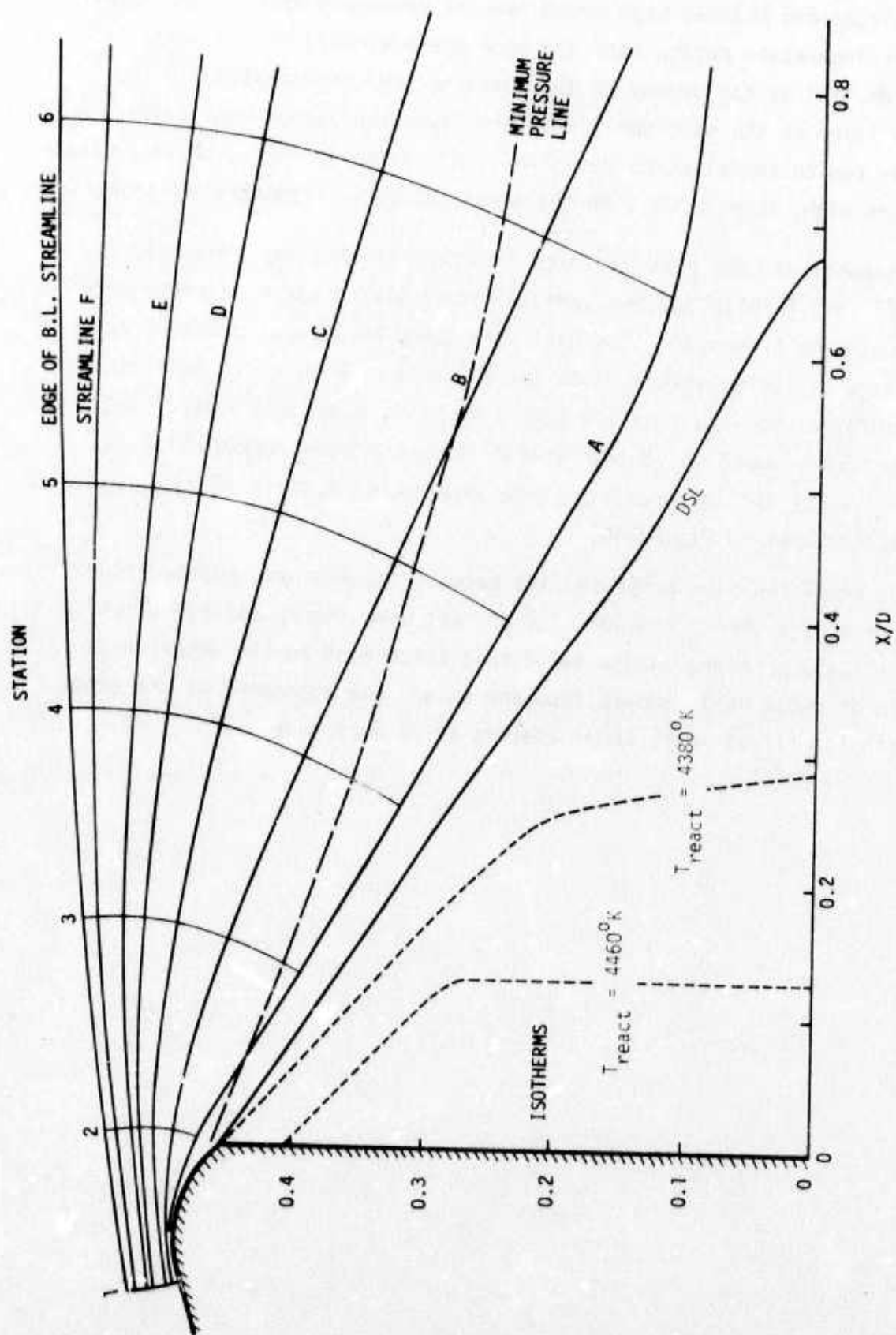


Figure 43. RMV-340 Vehicle - 25 km - Near Base Flowfield

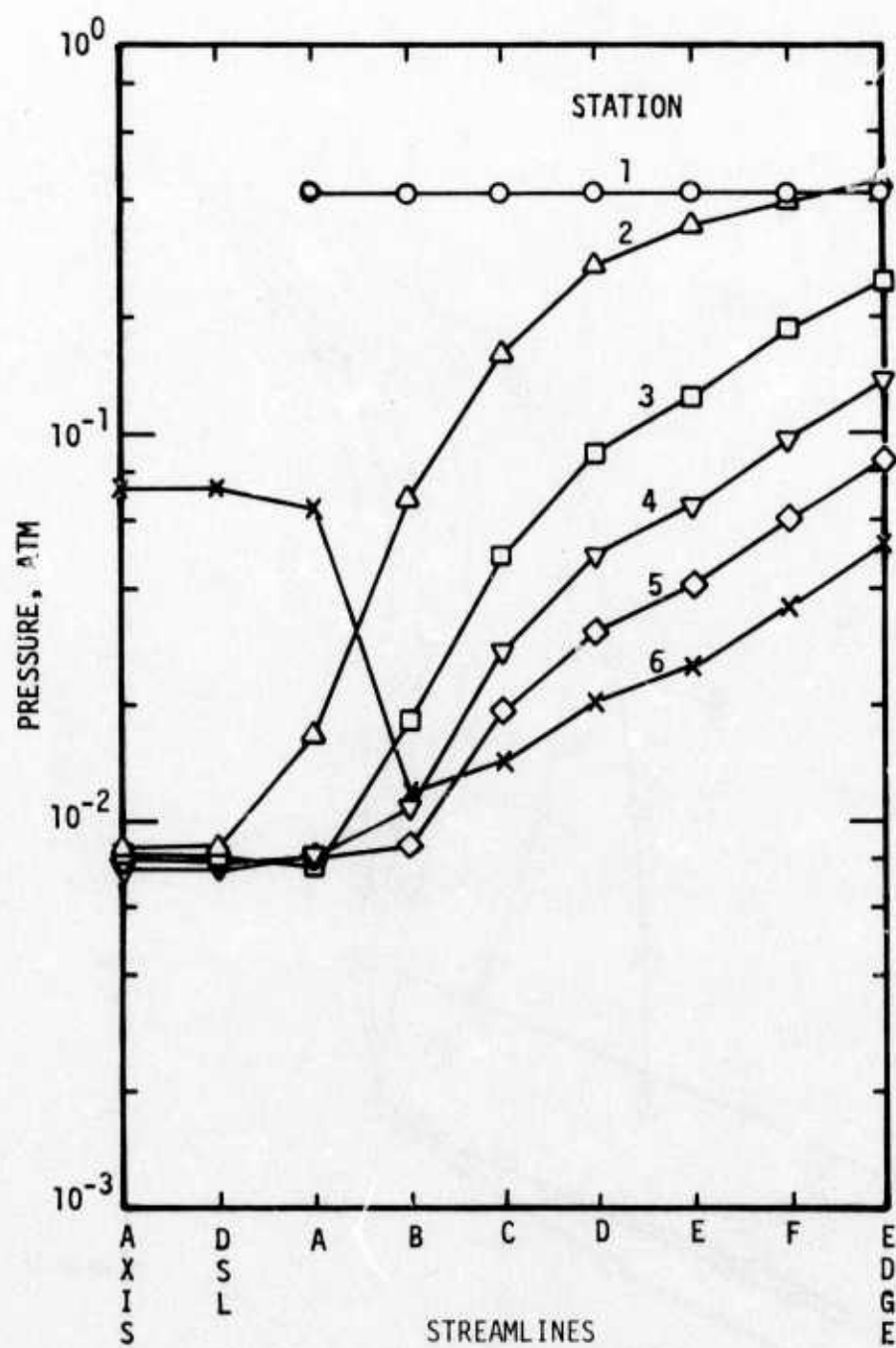


Figure 44. RMV-340 Vehicle - 25 km - Near Base Pressure Distributions

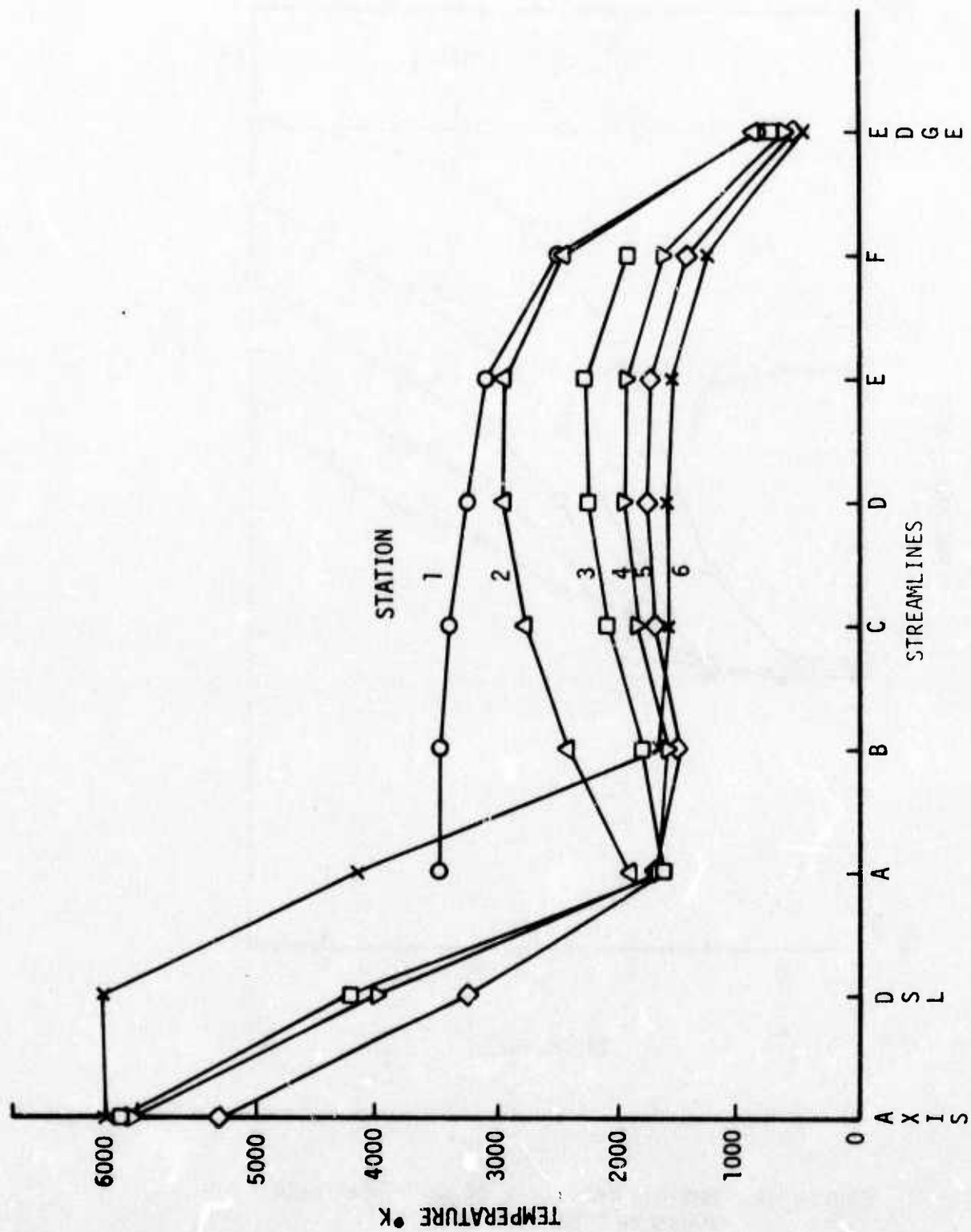


Figure 45. RMV-340 Vehicle - 25 km - Near Base Temperature Distributions

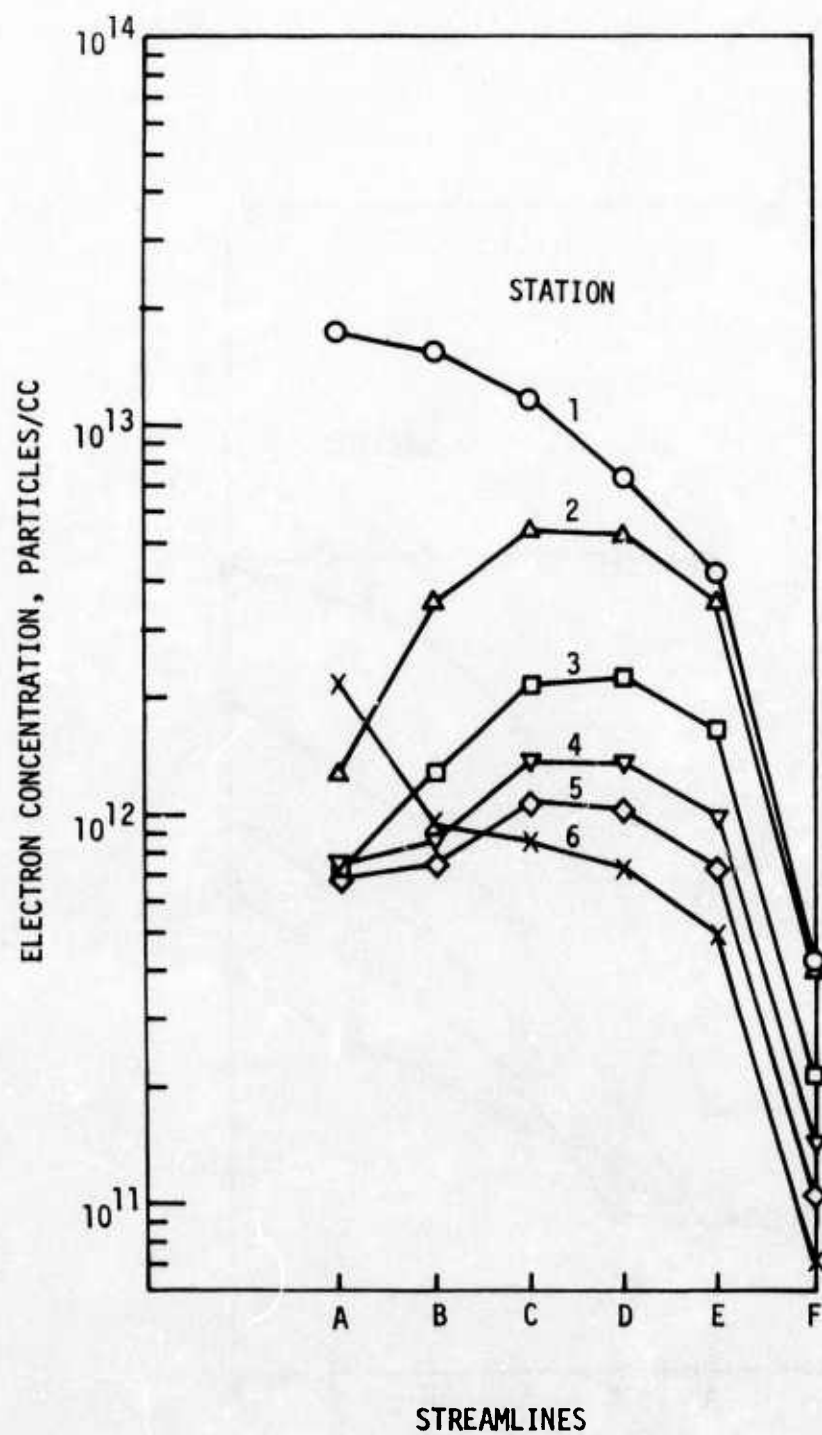


Figure 46: RMV-340 - 25 km - Near Base Electron Density Distribution - Outer Flow Region

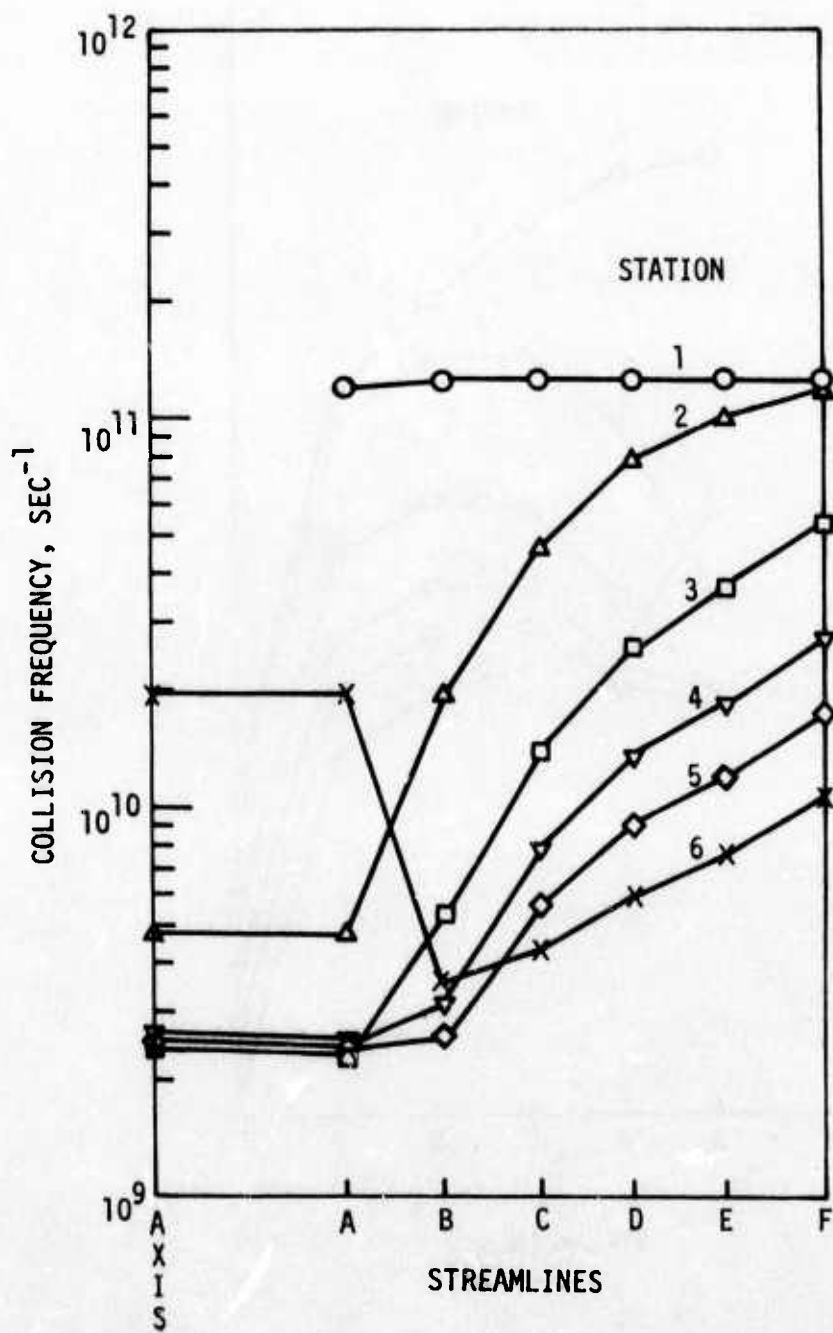


Figure 47: RMV-340 - 25 km - Near Base Collision Frequency Distributions

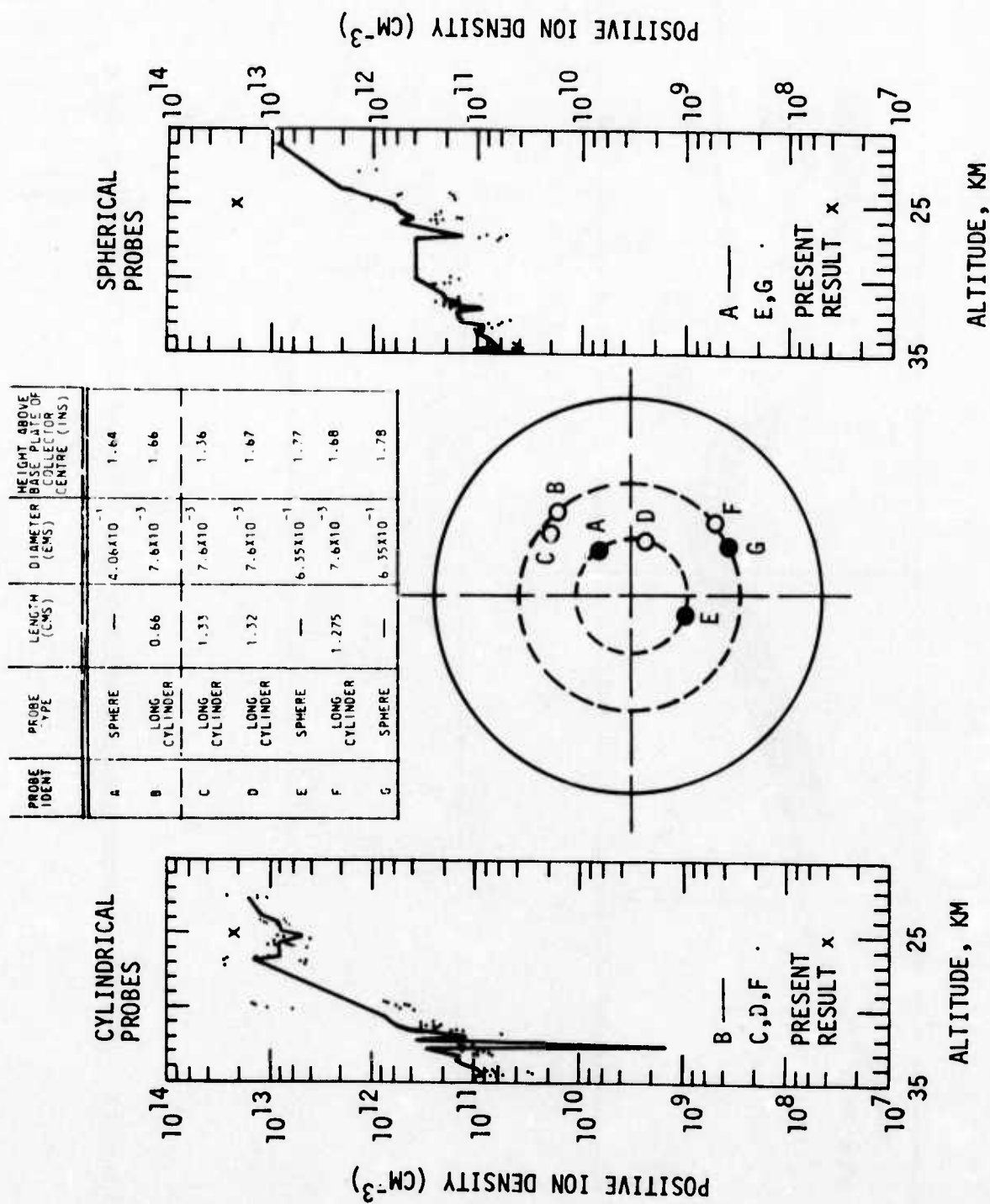
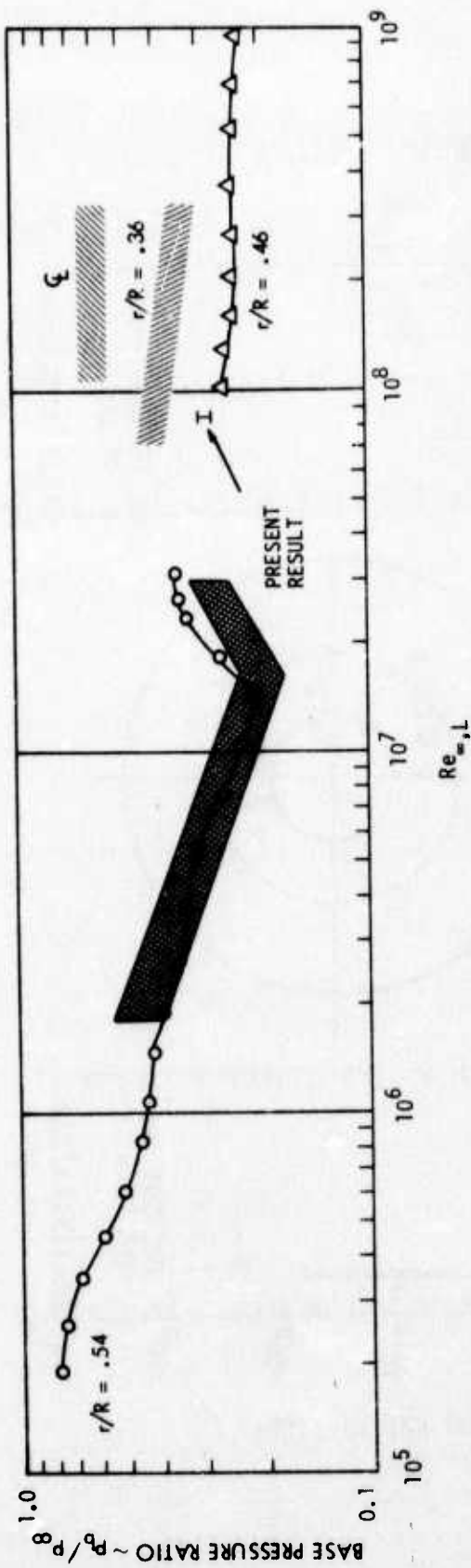


Figure 48. RMV-340 Recirculation Region Ion Concentration -- Comparison of Prediction with Values Deduced from Flight Measurements



LEGEND:

\circ	$r/R = .54$	$P_{MAX} = .01, .05 \text{ psia}$	FULL SCALE
Δ	.46	1.0	
	.0 (ζ)	2.0	
	.36	2.0	
	.0, .36	.1	

Figure 49. RMV-340 -- Comparison of Predicted Base Pressure with Flight Measurements

9. CONCLUSIONS

It is difficult to assess the degree of accuracy of an analysis of so many complex phenomena each of which is not fully understood. Uncertainties exist in the modeling of the ablation processes involving pyrolysis and char removal. Chemical processes in the boundary layer leading to the formation of charged species is assumptive. Finally, the accuracy of the modeling of turbulent diffusion models under the extreme environment of hypersonic reentry is unknown. The calculations and results presented here can, never-the-less, be useful provided the user recognizes them as representative of the best estimates that can be made in the spirit of engineering, and not scientific study.

The comparisons made with flight data were encouraging. The good agreement with measured base pressure suggests that the boundary layer profiles and diffusivity modeling are reasonable. Past experience with laminar flow has shown base pressure to be very sensitive to the boundary layer profiles before separation. The electrostatic probe experiments yield data which must be used in analytical models to deduce the ion and electron density levels, and uncertainties are thereby introduced. The fact that the predictions of ion concentration came to at the very least, an order-of-magnitude of the deduced values, and at the very best, agreed with the deduced values is acceptable and impressive.

The predictions for the full scale and small vehicles suggested that sources other than contaminant, low-ionization-potential materials may produce significant contributions to the electron density in the recirculation region. This effect appears to be very sensitive to temperature. Only in the case of the full scale vehicle did the predominance of $\text{NO}^+ - \text{e}^-$ emerge as important charged species in the recirculation region. This result makes the attempted simulation of the flow properties of the full scale vehicle by a small vehicle more complex. At lower velocities, the effect of NO ionization in the recirculation region diminishes suggesting that the electron density is eventually controlled by the seeding level.

The present results show that a lower seeding level is required for simulation in the recirculation region than in the outer wake above the recirculation region. However, reasonable simulation (factor of about 2 in electron density) may be achieved for a seeding level (≈ 500 ppm) which lies between that necessary for precise simulation of the recirculation region and outer flow regions, respectively.

REFERENCES

1. Shackleford, W. L., "Analysis of RMIP 9 Optical Reentry Data, I. Silica Phenolic Ablation and Flowfield Chemistry (U)," TRW Report No. 06488-6520-R3-00 (Secret), August 1971.
2. Fross, R. W., "Reentry Measurements Program Flight Test Evaluation Report (U)," (Flight KX-114), Philco-Ford Corp., Space and Reentry Systems Div., Report No. SG-4823 (SAMSO-TR-70-242) (Secret), May 1970.
3. Martellucci, A., Maguire, B. L., and Neff, R. S., "Analysis of Flight Test Transition and Turbulent Heating Data: Part I - Boundary Layer Transition Results," NASA CR 129045, GE TIS 72SD253, November 1972.
4. Ziemer, R. W., "Analysis and Correlation of Reentry Boundary Layer Transition Data (U)," TRW Systems Report No. 06488-6519-Re-00 (Secret), September 1971.
5. Levinsky, E. S. and Fernandez, F. L., "Approximate Nonequilibrium Air Ionization in Hypersonic Flows over Sharp Cones," AIAA Journal, Vol. 2, No. 3, p. 565, March 1964.
6. Hollander, T. J., Kalff, P. J., and Alkemade, C.T.J., "Ionization Rate Constants of Alkali Metals in CO Flames," Journal of Chemical Physics, Vol. 39, p. 2558, 1963.
7. Crocco, L. and Lees, L., "A Mixing Theory for the Interaction Between Dissipative Flows and Nearly Isentropic Streams," Journal of the Aeronautical Sciences, Vol. 19, No. 10, pp. 649-676, October 1972.
8. Ohrenberger, J. T. and Baum, E., "A Theoretical Model of the Near Wake of a Slender Body in Supersonic Flow, AIAA Paper No. 70-792, presented at AIAA 3rd Fluid and Plasma Dynamics Conference, Los Angeles, Calif., June 1970; also, AIAA Journal, Vol. 10, No. 5, May 1972.
9. Ohrenberger, J. T. and Baum, E., "Theoretical Modeling of the Base Flow Region of Supersonic Bodies: A Steady State Method," Published in Aerodynamics of Base Combustion - Progress in Astronautics and Aeronautics, Vol. 40, Murthy, editor, The MIT Press, 1976.
10. Bradshaw, P., Ferriss, D. H., and Atwell, N. P., "Calculation of Boundary Layer Development Using the Turbulent Energy Equation," Journal of Fluid Mechanics, Vol. 28, Part 3, pp. 593-616, 1967.
11. "ROPE Project Final Technical Report, Vol. II, Reentry Observables," TRW Report No. 18586-6047-R0-00, November 1972.
12. "ROPE Project Semi-Annual Technical Report," TRW Report No. 18586-6051-RU-00, July 1972.
13. Jensen, D. E. and Padley, P. J., "Kinetic Studies of Ionization and Recombination Processes of Metallic Additives to Flames," 11th Symposium (International) on Combustion, Berkeley, California p. 351, 1966.

REFERENCES (Continued)

14. Baskett, John, General Motors Corp., Delco Electronics, Santa Barbara, California ... private communication.
15. Kiel, R. E., Huggins, R. W., and Coston, W. P., "RMP-B Base-Mounted Electrostatic Probe Measurements (Flights 1, 6, 9, 10; KX-108, KX-115, KX-114, KX-116) (U)," Bell Telephone Laboratory, Reentry Physics Studies Report 71-17 (Secret), September 1971.
16. Huggins, R. W., Kiel, R. E., and Coston, W. P., "Examination of Boundary Layer Electrostatic Probe Data from RMP-B Flight 9 (KX-114) (U)," Bell Telephone Laboratories, Reentry Physics Studies Report 71-15 (Secret), September 1971.
17. Batt, R. G., "Flight Test Base Pressure Results for Sharp 8° Cones," AIAA Journal, Vol. 12, No. 4, p. 555, April 1974.

APPENDIX I
AEROHEATING, ABLATION, AND BOUNDARY LAYER ANALYSIS

I.1 Non-blowing/Non-ablating Aerodynamic Heating Calculation

The analytical procedure that has been incorporated into TRW's Aerodynamic Surface Heating Program (AEROHT)¹ is based on boundary layer convective heating and skin friction correlations obtained from published analyses so that the direct solution of the boundary layer conservation equations is avoided. Also, the air properties behind the leading edge or bow shock wave and the properties at the outer edge of the boundary layer are calculated by interpolation on the computer program built-in tables and/or input tables. In this manner a very fast and efficient utilization of the computer for obtaining solutions of sufficient accuracy for most engineering purposes is attained. The shock curvature effect on the convective heating rate distribution on the body is calculated by an approximate, mass balance, iterative technique; thus, the vorticity interaction between the inviscid outer flow (i.e., the shock layer) and the boundary layer are included in the calculations. The equilibrium radiation heat transfer rates from the shock-heated air to the vehicle surface are also calculated by interpolation on built-in tables.

The flight regimes for which the analysis is applicable include: wind tunnel test, ascent or launch, normal reentry, and reentry at super satellite speeds. These regimes are distinguished by the degree of dissociation or ionization of air present at the outer edge of the boundary layer. The heating rate analyses incorporated in the program that are applicable to the above mentioned regimes include: the stagnation point convective heating correlations of Fay and Riddell², and Hoshizaki³, and the similarity solutions of C. B. Cohen and Reshotko⁴, Beckwith and N. B. Cohen⁵, Kemp, Rose, and Detra⁶, and N. B. Cohen⁷ for laminar boundary layer heating and skin friction distributions. The equilibrium air thermodynamic properties built-in tables in the program are those reported by Curtis and Wohlwill^{8,9} which correspond closely with the air tables of Moeckel and Weston.¹⁰ A curve fit to real gas data is used to find empirical relations of state between density, viscosity, pressure, and enthalpy. The Moeckel and Weston¹⁰ and NBS¹¹ equilibrium air tables, together with the viscosity data of Hansen¹², are employed for this purpose. The partial Prandtl and Lewis numbers as a function of enthalpy

built-in tables are derived from NBS¹¹ and Hansen¹² data. The heat of reactions for calculating the dissociation enthalpies are obtained from Lees.¹³ For calculating the shock heated air radiation heat transfer rate to the vehicle surface the equilibrium radiation air emissivity coefficient table of Kivel and Bailey¹⁴ is employed. The correlations for turbulent boundary layer flow that are used in the program were derived by TRW¹⁵ using incompressible flat plate turbulent boundary layer solutions together with Eckert's reference properties method¹⁶ for accounting for compressibility effects. The convective heating is calculated from the skin friction solutions using Rubesin's modified Reynolds analog (MRA) method.¹⁷ The technique used in the derivation of the turbulent correlation equations is similar to the analytical procedure of Rose, Probstein, and Adams.¹⁸

In performing the analysis, the free stream ambient conditions (V_∞ , p_∞ , and T_∞), the radius of curvature (nose radius) of the stagnation point, and the pressure distribution normalized by the stagnation point pressure are prescribed as independent input variables. To calculate the shock shape that is needed to determine the entropy layer effects, the shock shape correlations of Love, Woods and Rainey¹⁹ are used. Boundary layer transition from laminar to turbulent flow is determined from a transition criterion defined via input.

I.2 Wall Interface and In-Depth Response

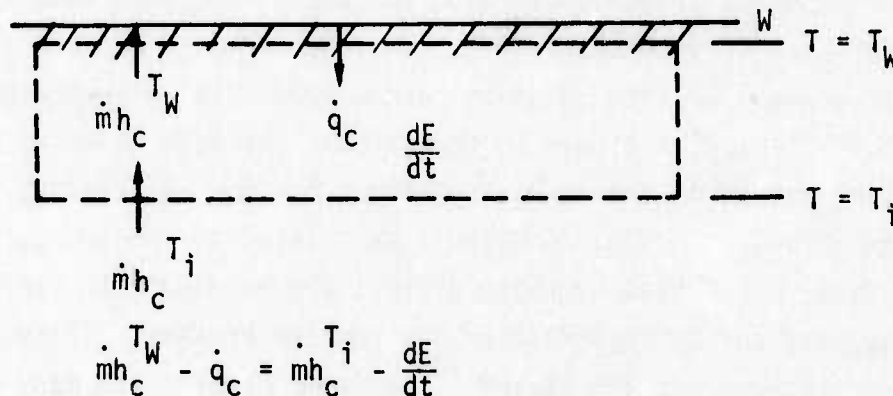
A description of the wall interface and in-depth response analysis applied to the present cases through the CARE²⁰ computer program is now discussed. The present heatshield materials, carbon phenolic and silica phenolic, are of a class of so called charring ablators. Here, the original virgin material decomposes by pyrolysis when the temperature reaches a sufficiently large value. Gases are formed which percolate away from the pyrolysis zone, leaving behind a porous residue or char. The analysis assumes that the decomposition process is temperature dependent through an Arrhenius-type relation. Removal of the char is assumed to occur by the basic ablation processes which include sublimation of the char material and removal by chemical reactions with the adjacent boundary layer fluid. Here, the wall interface chemistry is described by two parameters, namely, the heat-of-fusion (or sublimation) of the char and the heat-of-reaction (or oxidation).

Using a one dimensional transient formulation, an in-depth energy balance differential equation is written in terms of moving coordinates, i.e., the independent coordinate is tied to the receding char surface. The solution is by finite differences. Nodal positions are specified in the input by specifying successive node thicknesses. All the physical properties needed, to obtain solutions are specified as input tables that may be a function of one or more independent variables, e.g., temperature and pressure. Any surface recession causes the nodal spacing to shrink.

I.3. Steady-State Ablation Analysis (Program SAANT)

The problem modeled by the Aerotherm Steady State Analysis of Ablating Nostips (SAANT) computer code²¹ is that of determining the instantaneous profile of an ablating axisymmetric nosetip re-entering the atmosphere at zero degrees angle of attack. The basic environment information required by the code is the freestream state (pressure and density) and velocity. Given this information the code performs real gas calculations for air to find the stagnation conditions.

The in-depth thermal response is handled by the following energy balance:



where: \dot{m} ablation mass loss rate

$h_c^{T_W}$ enthalpy of the ablation material (before chemical reactions) evaluated at the wall temperature

$h_c^{T_i}$ the enthalpy of the material before exposure, $T_i \sim 536^\circ R$

\dot{q}_c conduction heat flux into the control volume

$\frac{dE}{dt}$ time-rate of change of energy stored

The steady state assumption implies that dE/dt is zero and corresponds to the physical situation when the temperature profile relative to the moving wall-interface surface is invariant with time. The assumption is accurate for low conductivity ablators and for high ablation rate situations. By considering $dE/dt = 0$, the calculation of $\dot{m}h_c^w - \dot{q}_c$ is simplified since the quantity is independent of the ablation material thermal properties or response history.

The analytical treatment of the wall interface mass and energy balances is modeled to account for the strong coupling which exists between convective heating, chemistry, diffusion, and blowing. The diffusion of edge (air) molecular species to the wall and ablation products species moving away from the wall are modeled together with the chemical reaction events taking place at the wall interface. The effect of heat blocking due to foreign species injection is also included. The program utilizes an equilibrium chemistry computer code, i.e., Aerotherm's ACE code.²² Surface state or mass balance solutions are parametrically generated. These solutions (tables) are used to reconstruct the mass balances at particular time points of the entry trajectory and for calculating the chemistry and molecular diffusion effects as related to the energy balances at the wall interface. Heat blocking effects are handled with various degrees of sophistication depending on the problem treated. These effects have been correlated using the KBLIMP²³ computer program and many other sources (see Reference 24). The methodology for calculating the boundary layer in the SAANT program is essentially the same as the procedure described in Appendix I.1. However, the SAANT program uses different correlations for calculating the non-blowing/non-ablating boundary layer and shock shape.²¹

I.4. Boundary Layer Analysis (Program TRW-KBLIMP)

The NASA equilibrium/non-equilibrium KBLIMP computer program was used to generate the detailed boundary layer solutions with chemical reactions and ablation to provide initial conditions for the shoulder separation and wake analysis. The KBLIMP program was originally developed

by Aerotherm for NASA-AMES for execution on a CDC-7600 computer, and has been subsequently modified at TRW. Basically, the program solves the compressible flow boundary layer equations with chemical reactions for both laminar and turbulent flows. A mixed set of equilibrium and non-equilibrium reactions can be treated. In the present application to the carbon- and silica-phenolic heatshields, approximately 32 to 37 species were considered, with all but Na and Na^+ ($+e^-$) determined by equilibrium chemistry. The boundary conditions for the wall interface applied here consisted of specification of the wall temperature and mass ablation under surface equilibrium conditions (including the sodium species which are treated as non-equilibrium species away from the wall).

The program uses a novel numerical solution procedure, termed as integral matrix approach, which is equivalent to a higher order finite difference approach (using spline fits), though the equations are solved in integral form. Thus, the program is capable within practical limits of obtaining accurate solutions to the governing differential equations with fewer chemistry calculations in comparison with other contemporary computer programs. Thermodynamic properties of the chemical species are obtained from JANAF tables^{25,26} and other sources,^{27,28,29} and used in the form of polynomial curve fits to the tabulated data. Constants appropriate to a lower and an upper temperature range (less or greater than 3000°K) are determined by a least squares curve-fit routine.

The transport properties for single components are based on correlations for single species self-diffusion binary coefficients.³⁰ The mixture viscosity follows the method of Buddenberg and Wilke.³¹ The mixture thermal conductivity is based on the method of Mason and Saxena with Eucken correction.³² The basic turbulent model adopted is specifically formulated for boundary layer flows with blowing.³³ Turbulence is described in the wall region by a mixing length equation, which approaches Prandtl's expression, $\ell = k_m y$, far from the wall. The mixing length distribution is changed for blown flows implicitly, by the influence of blowing on local shear stress, τ . The equation for mixing length is solved and used to find eddy viscosity from

$$\epsilon_m = \ell^2 \frac{\partial \bar{u}}{\partial y}$$

This wall region eddy viscosity is used from the wall on out into the boundary layer until it exceeds the wake region eddy viscosity given by

$$\epsilon_m = C u_e \delta_i^*$$

$C = 0.018$, the Clauser wake constant, which can be redefined via input. The eddy diffusivity and eddy conductivity are related to the body viscosity by the turbulent Schmidt and Prandtl numbers. A value of 0.75 for each of these is recommended unless otherwise specified by input.

I.4.1 Nonequilibrium Chemistry Procedure (Program KBLIMP)

Homogeneous Chemistry

Chemical reaction rates are calculated using the procedures described in Reference 23. The m -th stoichiometric chemical reaction is written as

$$\sum u_{jm}^R N_j = \sum u_{jm}^P N_j$$

and its reaction rate can be expressed generally by

$$\bar{R}_m = k_{Fm} \left[\prod p_j^{u_{jm}^R} - \frac{1}{K_{Pm}} \prod p_j^{u_{jm}^P} \right]$$

The equilibrium constant K_p can be determined from the standard state free energy change, and the forward reaction rate constant can be expressed in the Arrhenius form

$$k_{Fm} = B_m T^{A_m} \exp \left[- E_{am} / RT \right]$$

where	A_m	Temperature exponent in Arrhenius expression
	B_m	pre-exponential coefficient in Arrhenius expression
	E_{am}	activation energy in Arrhenius expression
	k_{Fm}	forward reaction rate
	K_p	equilibrium constant

N	chemical species label
p_j	partial pressure
R	universal gas constant
\bar{R}_m	net reaction rate
T	temperature
μ	stoichiometric coefficients

For the third body chemical reactions, the particular third body species influences the production rate however in many cases, only the probability coefficient B_m is different. In these cases, some reduction in the number of equations can be achieved by specifying a reference value of B_m and the relative efficiencies r_{m_i} of each third body. Then by omitting the third body from the stoichiometric reaction an effective reaction rate k_F^i can be specified in terms of the molar concentrations n_i of the third bodies, i.e., i.e.,

$$k_{F_m}^i = \left(\sum_i r_{m_i} n_i \right) B_{m_r} T_m^A \exp \left(-E_{a_m}/RT \right)$$

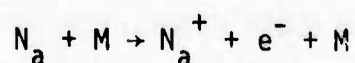
Mixed Equilibrium/Nonequilibrium

The prototype KBLIMP program (Aerotherm's) cannot analyze a mixed equilibrium/nonequilibrium chemical system with ions because of input variable built-in restrictions and the special treatment of the electron, i.e., ambipolar diffusion. Effectively the electron species is flagged and omitted from consideration in the diffusion transport equation. The concentration of electrons is determined from the molecular balance of ionized species so that the net charge at a spatial point is zero. This restriction represents a severe limitation for the current application where it is desired to consider a large number of species to be in chemical equilibrium including ionized species such as NO^+ , CHO^+ , etc., simultaneously with the nonequilibrium reaction for $N_a \rightarrow N_a^+ + e^-$. By virtue of the fact that only two molecular species N_a and N_a^+ are involved it was possible to alter the logic of the program to consider the $N_a \rightarrow N_a^+ + e^-$ reaction without altering the chemically equilibrated set that includes the remaining species. In essence the NA and Na^+ species are defined as

elemental species and the electrons associated with the reaction $N_a \rightarrow N_a^+ + e^-$ are considered only in the calculation for the backward reaction rate and omitted from the equilibrated chemical species set. The basis for the above procedure was inspired by the very general formulation of the chemical reactions treatment incorporated into the program which is described in detail in Reference 34.

Kinetic Rate Constants for Sodium Ionization

The reaction stoichiometric equation considered is



where M = third body, $M = N_2$ was used.

The corresponding kinetic rate constants used in the analysis are:

$$B_m = 1.20 \times 10^{16} \text{ GRAM-MOLE/cc-sec}$$

$$A_m = 0.50$$

$$E_a = 59400^\circ K$$

$$r_{N_2} = 1.0$$

APPENDIX I
REFERENCES

- I-1 Gomez, A. V. and Korb, G. M., "Aerodynamic Surface Heating Analysis Program (AEROHT) for Atmospheric Entry and Launch Vehicles, TRW Program Number HH041A/AH005H," Report 20029-H039-R0-00, TRW Systems, Houston, Texas, February 1972.
- I-2 Fay, J. A. and Riddell, F. R., "Theory of Stagnation Point Heat Transfer in Dissociated Air," J. Aero. Sciences, Vol. 25, Feb. 1958, pp. 73-85.
- I-3 Hoshizaki, H., "Heat Transfer in Planetary Atmospheres at Super-Satellite Speeds," ARS Journal, Vol. 32, October 1962, pp. 1544-1552.
- I-4 Cohen, C. B. and Reshotko, E., "Similar Solutions for the Compressible Laminar Boundary Layer with Heat Transfer and Pressure Gradient," Report 1293, 1956, NACA.
- I-5 Beckwith, I. E. and Cohen, N. B., "Application of Similar Solutions to Calculation of Laminar Heat Transfer on Bodies with Yaw and Large Pressure Gradient in High Speed Flow," TN D-625, 1961, NASA.
- I-6 Kemp, N. H., Rose, P. H., and Detra, R. W., "Laminar Heat Transfer Around Blunt Bodies in Dissociated Flow," J. Aero/Space Sciences, Vol. 26, No. 7, July 1959, pp. 421-430.
- I-7 Cohen, N. B., "Boundary-layer Similar Solutions and Correlation Equations for Laminar Heat-Transfer Distribution in Equilibrium Air at Velocities up to 41,100 Feet Per Second," TR R-118, 1961, NASA.
- I-8 Curtjs, M. W., and Wohlwill, H. E., "Thermodynamic Properties of Air from 1000°K to 10,600°K along Contours of Constant Density, Enthalpy, and Entropy," Report 7102-0012-MU-000, March 1961, STL.
- I-9 Curtjs, M. W., and Wohlwill, H. E., "Thermodynamic Properties of Air from 9500°K to 14,800°K along Contours of Constant Density, Enthalpy, and Entropy," Report 7102-0012-MU-A01, June 1961, STL.
- I-10 Moeckel, W. E. and Weston, K. C., "Composition and Thermodynamic Properties of Air in Chemical Equilibrium," TN 4265, April 1958, NACA.
- I-11 Hilsenrath, J., "Table of Thermal Properties of Gases," NBS Circular No. 564, 1955.
- I-12 Hansen, C. F., "Approximations for the Thermodynamic and Transport Properties of High Temperature Air," TR-R-50, 1959, NASA.
- I-13 Lees, L., "Convective Heat Transfer with Mass Addition and Chemical Reactions," presented in Recent Advances in Heat and Mass Transfer, McGraw-Hill, 1961.
- I-14 Kivel, B. and Bailey, K., "Tables of Radiation from High Temperature Air," Report 21, December 1957, Avco Research.

- I-15 Wilkinson, H. R., "Turbulent Boundary Layer Analysis and Correlations for TRW's Aerodynamic Surface Heating Program AH005H," Unpublished Personal Notes, TRW Systems Inc., 1965.
- I-16 Eckert, E. R. G., "Engineering Relations for Friction and Heat Transfer to Surfaces in High Velocity Flow," Reader's Forum, J. Aero. Sciences, Vol. 22, No. 8, Aug. 1955, pp. 585-587.
- I-17 Rubesin, M. W., "A Modified Reynolds Analogy for the Compressible Turbulent Boundary Layer on a Flat Plate," TN-2917, March 1953, NACA.
- I-18 Rose, H. P., Probst, R. F., and Adams, Mac C., "Turbulent Heat Transfer Through a Highly Cooled, Partially Dissociated Boundary Layer," J. Aero/Space Sciences, Vol. 25, No. 12, Dec. 1958, pp. 751-760.
- I-19 Love, E. S., Woods, W. C., and Rainey, R. W., "Some Topics in Hypersonic Body Shaping," AIAA Paper No. 69-181, AIAA 7th Aerospace Sciences Meeting, New York, January 20-22, 1969.
- I-20 TRW Staff, "Coupled Conduction, Ablation, Reaction, and Erosion (CARE)," Miscellaneous Documentation: New Options, IOC 74.6411.30-5; Input Options, IOC 74.6411.30-6; Roughness Heating Augmentation, IOC's 74.6411.30-14 and -22; Erosion Option, IOC 74.6411.30-23; Control Cards, IOC 74.6411.30-32; Wall Enthalpy, IOC 74.6411.30-50; Revised Input, IOC 74.6411.30-62, TRW Systems, 1974.
- I-21 Aerotherm Staff, "Passive Nosedip Technology (PANT) Program, User's Manual: Steady-State Analysis of Ablating Nosedips (SAANT), Volume I: Program Description and Sample Problems," Report UM-73-38, Aerotherm Division, Acurex Corporation, October 1973.
- I-22 Powars, A. C., and Kendall, R. M., "User's Manual: Aerotherm Chemical Equilibrium (ACE) Computer Program," Aerotherm Report UM-69-70, Aerotherm Corp., Mountain View, California, May 1969.
- I-23 Tong, H., Buckingham, A. C., and Morse, H. L., "Non-Equilibrium Chemistry Boundary Layer Integral Matrix Procedure," Aerotherm Report UM-73-67, Aerotherm Division, Acurex Corp., July 1973.
- I-24 Gomez, A. V. and Mills, A. F., "Multi-Component, Foreign Species Injection, Heat Transfer, Skin Friction, and Mass Transfer Correlations for the Hypersonic, Laminar Boundary Layer in the Stagnation Region Including Chemical Reactions," TRW Report No. 11176-H0244-R0-00, June 30, 1969.
- I-25 Joint Army, Navy, Air Force Thermochemical Panel, JANAF Thermochemical Tables, USAF Contract F04611-67-C-0009, December 1964 and supplements to date.
- I-26 Dergazarian, E. T., et al., "JANAF Thermochemical Tables," Thermal Laboratory, The DOW Chemical Company, Midland, Michigan, December 1960 and supplements to date.

- I-27 D'Amur, I. and Mason, E. A., "Properties of Gases at Very High Temperatures," The Physics of Fluids, Vol. 1, No. 5, September-October 1958, pp. 370-383.
- I-28 Duff, R. E. and Bauer, S. H., "Equilibrium Composition of the C/H System at Elevated Temperatures," Journal Chem. Phys., Vol. 26, April 1962, p. 1754.
- I-29 Hochstim, A. R., "Equilibrium Compositions, Thermodynamic and Normal Shock Properties of Air with Additives," Vol. 1, Zph-122, 1961, General Dynamics, Convair.
- I-30 Deblaye, C. and Bartlett, E. P., "An Evaluation of Thermodynamic and Transport Properties for use in the BLIMP Nonsimilar Multicomponent Boundary-Layer Program," Report No. SC-CR-69-3271, Sandia Laboratories, Albuquerque, New Mexico, July 1969.
- I-31 Buddenberg, J. W., and Wilke, C. R., "Calculation of Gas Mixture Viscosities," Ind. and Eng. Chem., Vol. 41, 1949, pp. 1345-1347.
- I-32 Mason, E. A. and Saxena, S. C., "An Approximate Formula for the Thermal Conductivity of Multicomponent Gas Mixtures," Phys. Fluids, Vol. 1, 1958, pp. 361-369.
- I-33 Anderson, L. W. and Morse, H. L., "A Turbulent Model Study for the Multicomponent Nonsimilar Turbulent Boundary Layer Program," Aerotherm Report 71-28 (AFWL-TR-71-57), Aerotherm Corporation, Mountain View, Calif., June 1971.
- I-34 Kendall, R. M., "An Analysis of the Coupled Chemically Reacting Boundary Layer and Charring Ablator, Part V: A General Approach to the Thermochemical Solution of Mixed Equilibrium-Nonequilibrium, Homogeneous or Heterogeneous Systems," NASA CR-1064, 1968.

APPENDIX II: NEAR WAKE FLOW MODEL

The flowfield analysis applied here describes the boundary layer and wake regions downstream of the undisturbed boundary layer approaching the aft shoulder of the vehicle. This includes the separating boundary layer on the rounded aft shoulder. The formulation is classed as a viscous-inviscid interaction problem in which the pressure field is unknown and determined during the course of the calculations. However, as will be seen, the diffusion terms are included in the calculation throughout the flowfield. Hence, the inviscid regions emerge naturally from the calculation where diffusion is found to be unimportant.

The wake is divided into two regions which are, respectively, interior and exterior to a streamline which lies adjacent to the dividing streamline over the recirculation region and to the axis, downstream of the wake stagnation point. The inner region is described as an integral method in which the conservation equations are integrated from the axis to the "matching streamline" separating the two regions. The outer region is described by a finite difference method, using conservation equations which retain both the inviscid terms and boundary-layer-like viscous terms. A strict matching of essential flow properties is maintained between the two regions. The equations used to describe the outer wake region are also applied to the entire boundary layer, with the boundary conditions changed to the no slip conditions at the wall.

7.2.1 Outer Flow Description

A natural or intrinsic coordinate system formed by streamlines and normals to streamlines is used to describe the outer flow. If s and n represent distances along, and normal to, streamlines, respectively, then orthogonal independent variables ψ , S , and ϕ can be formed where $d\psi = \rho U r^\alpha dn$, $dS = ds/h_s$, and $\phi = \text{azimuthal angle (when } \alpha = 1)$. The metrics are $h_\psi = 1/(\rho U r^\alpha)$, $h_\phi = r^\alpha$ and h_s (to be determined later). This coordinate system and set of independent variables has a number of advantages in the present problem. Dropping the streamwise second derivatives yields a single

set of governing equations which are applicable to the flow on the body (including the rounded shoulder), as well as the wake flow above the dividing streamline. These equations are inclusive of the classical boundary-layer-like equations used to describe the body boundary layer, the shear layer, and the downstream viscous wake. In addition, they contain the complete inviscid formalism even in the viscous regions of the flow. They are therefore well-suited for describing the expansion of the boundary layer about the rounded shoulder, where viscous effects become important in a progressively thinner region, and for describing the origins of the lip and wake shock waves as diffuse compressions well within the viscous regions. Since the cross-stream viscous terms are included throughout, it is unnecessary to distinguish between the viscous and inviscid regions of the flow in the formation; the inviscid regions will appear as a natural outcome of the analysis.

The Navier-Stokes and energy equations in this coordinate system are given in Reference II-1. Dropping all terms containing second derivatives with respect to S leads to the forms of the momentum and energy equations applied here:

$$\partial U / \partial S + (1/\rho U)(\partial P / \partial S) = (\partial / \partial \psi) [\mu h_s r^{2\alpha} \rho U (\partial U / \partial \psi)] \quad (1)$$

$$U(\partial \theta / \partial S) + h_s r^\alpha (\partial P / \partial \psi) = \frac{4}{3} (\partial / \partial \psi) [\mu h_s r^{2\alpha} \rho U^2 (\partial \theta / \partial \psi)] \quad (2)$$

$$\begin{aligned} \partial H / \partial S = (\partial / \partial \psi) [(\mu / \text{Pr}) h_s r^{2\alpha} \rho U (\partial H / \partial \psi)] + (\partial / \partial \psi) \\ [((\text{Pr} - 1) / \text{Pr}) \mu h_s r^{2\alpha} \rho U^2 (\partial U / \partial \psi)] \end{aligned} \quad (3)$$

θ is, here, the streamline inclination angle. By relating this coordinate system to the Cartesian system, two additional relations are obtained after eliminating, by cross-differentiation, derivatives with respect to r and x ; thus

$$\partial (\rho U r^\alpha)^{-1} / \partial S = h_s (\partial \theta / \partial \psi) \quad (4)$$

$$\partial h_s / \partial \psi = - (\rho U r^\alpha)^{-1} (\partial \theta / \partial S) \quad (5)$$

In addition, an equation of state and viscosity law are specified. The modeling of viscosity in the case of turbulent flow will be the subject of Section II-3.

The relationship of this coordinate system to the Cartesian system is

$$\begin{aligned} \partial x / \partial S &= h_s \cos \theta & \partial x / \partial \psi &= -\sin \theta / \rho U r^\alpha \\ \partial r / \partial S &= h_s \sin \theta & \partial r / \partial \psi &= \cos \theta / \rho U r^\alpha \end{aligned} \quad (6)$$

Implicit finite-difference approximations are used to represent the equations, and since they are mathematically parabolic in character, they are solved by marching in the streamwise direction beginning with specified initial profiles on the body upstream of the shoulder. The boundary conditions will be discussed below. Details of the differencing and of the method of solution of the difference equations can be found in Reference II-1.

The initial and boundary conditions imposed on this set of equations consist of a set of profiles for the dependent variables (velocity, pressure, flow angle, and enthalpy) along a normal to streamlines from the body to the bow shock wave upstream of the rounded shoulder. The no slip boundary conditions are imposed to calculate the separating boundary layer. After separation, the matching conditions between the inner and outer regions provide the necessary boundary conditions for the outer region. The lateral boundary of the calculation consists of the uniform flow upstream of the bow shock, or in the present application, the edge-of-boundary layer streamline.

II-2 INNER FLOW DESCRIPTION

The integral method is applied to the inner region primarily for reasons of compatibility with the outer flow. The inner region equations are ordinary differential equations with the axial coordinate as the independent variable. These equations may be integrated from the base in step with the finite differences marching solution for the outer flow, and a matching of essential flow properties can be maintained between the two regions at each computing step. A finite differences solution of the inner region, while

seemingly more accurate, is extremely difficult to match to the outer region, and is computationally time consuming. For practical computing times, the matching resolution would be so poor that the entire near wake solution would be seriously degraded.

The flowfield properties below the matching streamline are described approximately using radial profile shapes of specified r dependence. The x -dependent parameters in the profiles are then evaluated by requiring that the integrated conservation equations be satisfied, in addition to satisfying the requisite boundary conditions including profile and flux matching at the matching streamline. Finally, the remaining parameters are determined by satisfying integral moments of conservation equations or locally satisfying the conservation equations at a particularly important point in the profile (the centerline). The initial values of the parameters describing the profiles can all be determined at the separation point by matching to the outer profile and from geometric considerations, except for the one parameter representing the centerline enthalpy. As expected, the integral formulation, when integrated downstream using an arbitrary initial centerline enthalpy, encounters a saddlepoint singularity at the wake stagnation point, as illustrated in Figure 9. The value which is consistent with a closed recirculation region with no energy source or sink at the stagnation point is the one which permits the calculation to continue downstream into the wake in a physically meaningful way. The details of the formulation can be found in Reference II-1.

II.3 TURBULENCE MODELING EQUATIONS

The ability to predict the changing turbulence structure in the near wake lies within the framework of modern higher order theoretical analyses of non-homogeneous fully-developed turbulence which have appeared in the literature during the past several years. The turbulence is characterized by two independent variables often consisting of the turbulent kinetic energy due to the fluctuations, e , and a mean macroscopic or integral scale length of the turbulence, λ . The Reynolds stresses are usually represented

by the product of an eddy diffusivity, which from dimensional arguments is proportional to $e^{1/2} \ell$, and a mean flow strain rate. The turbulence variables, and hence the eddy viscosity, are treated as field variables whose distribution depends on the mean flow and whose values are obtained from the solution of two diffusion-type equations which represent the convection, growth, decay, and diffusion of turbulence in the flow. Beginning with known mean flow and turbulence properties in the boundary layer before separation, this modeling permits accounting for a variety of effects such as the changing turbulent structure in the boundary layer remnant during the expansion into the wake (including possible dissipative effects which have a tendency to relaminarize the remnant flow), the interaction of the remnant turbulence with the turbulence produced in the mixing layer and wake, the effect of the pressure rise across the shock waves on the turbulence, the influence of turbulence in the recirculation region, and the effect on the diffusivity of the strong pressure rise in the vicinity of the wake stagnation point.

The change in turbulent structure in the present analysis is based upon a model equation for the turbulent kinetic energy, e , and a second model equation for the dissipation rate of turbulence, $\epsilon_d = C_d e^{3/2} / \ell$ where C_d is a constant.

The form of these equations, written in streamfunction coordinates is represented below:

Turbulent Energy

convection production dissipation compressibility
effect

$$\frac{\rho U}{h_s} \frac{\partial e}{\partial s} = \mu_T \left(\rho U r^\alpha \right)^2 \left(\frac{\partial U}{\partial \psi} \right)^2 - \rho \epsilon_d \left(1 + K_1 / R_T \right) + \epsilon_1 \frac{e}{\gamma p} \frac{\rho U}{h_s} \frac{\partial p}{\partial s} \quad (7)$$

diffusion

$$+ \frac{\rho U}{h_s} \frac{\partial}{\partial \psi} \left[\left(\mu + \sigma^* \mu_T \right) U r^{2\alpha} h_s \frac{\partial e}{\partial \psi} \right]$$

Turbulent Dissipation Rate

$$\begin{aligned}
 &\text{convection} \quad \text{production} \quad \text{dissipation} \quad \text{compressibility effect} \\
 \frac{\rho U}{h_s} \frac{\partial \epsilon_d}{\partial s} = & C_1 \left(\rho U r^\alpha \right)^2 \frac{\epsilon_d}{e} \mu_T \left(\frac{\partial U}{\partial \psi} \right)^2 - \frac{\rho \epsilon_d^2}{e} \left(C_2 + K_2/R_T \right) + \epsilon_2 \frac{\epsilon_d}{\gamma p} \frac{\rho U}{h_s} \frac{\partial P}{\partial S} \\
 &\text{diffusion} \\
 &+ \frac{\rho U}{h_s} \frac{\partial}{\partial \psi} \left[\left(\mu + \sigma \mu_T \right) \rho^{-1/2} U r^{2\alpha} h_s \frac{\partial \rho^{3/2} \epsilon_d}{\partial \psi} \right]
 \end{aligned} \tag{8}$$

The turbulent viscosity and turbulent Reynolds number are defined as

$$\mu_T = \rho e^{1/2} \ell / (1 + K_3/R_T) \tag{9}$$

and

$$R_T = \rho e^{1/2} \ell / \mu . \tag{10}$$

The production term appearing in each equation results from the working of the Reynolds stress against the mean flow velocity gradients. The dissipation rate governed by turbulence in the macroscale regime comprises the first part of the dissipation term of each equation. Also included are factors which become important at low values of turbulent Reynolds number where the macroscale and microscale lengths become of the same order. These effects are important in the laminar sublayer of the turbulent boundary layer, and possibly in the expansion of the boundary layer remnant into the wake. The constants K_1 and K_2 appearing in these factors take on different values in these two regions due to the highly anisotropic character of the sublayer turbulence as compared with the more isotropic-like turbulence in the outer remnant of the boundary. Table I summarizes the constants used in the present analysis. They are chosen, for the boundary layer, so that the low Reynolds number dissipation term balances the laminar diffusion term to lowest order in the laminar sublayer and are determined for wake flows so that the equations yield the final decay of isotropic turbulence consistent with the rigorous solution of Batchelor. II-2

Table I. Low R_T Dissipation Constants

Dissipation Constants	Boundary Layers	Wakes *
K_1	$\frac{2 \kappa^2}{C_d^{1/2}}$	$5\pi \frac{C_d}{K_d^2}$
K_2	$\frac{2 \kappa^2}{C_d^{1/2}}$	$\frac{17\pi}{2} \frac{C_d}{K_d^2}$

* $K_d = 0.4$ from Finson II-5

The turbulent viscosity also contains a low Reynolds number term for boundary layer flows which serves the purpose of scaling the laminar sub-layer thickness. To maintain agreement with classical flat plate incompressible boundary layer profiles, $K_3 = 16.5$. This term is not required for wake flows.

The diffusion term appearing in both equations models the diffusion of turbulence (present in the fundamental form of the equations in the form of triple correlations). The density factors appearing in the diffusive flux terms $\rho^{-1} \partial \rho e / \partial \psi$ and $\rho^{-3/2} \partial \rho^{3/2} \epsilon_d / \partial \psi$ account for the effects of compressibility found in high Mach number flat plate boundary layers. These effects include the observed invariance with Mach number of the velocity profile under a Van Driest transformation $du^* = (\rho/\rho_w)^{1/2} du$, and of the integral scale length (see Maise and McDonald).^{II-3}

The compressibility term appearing in both equations is a consequence of density-velocity correlations and was modeled by Wilcox and Alber^{II-4} in the form presented here. It is a significant term during the expansion of the boundary layer into the wake, and through the compression zones associated with the formation of the lip and wake shock waves, as well as across the shock waves themselves. In the absence of production and dissipative effects, the turbulence behaves isentropically, according to the relations

$$e \sim p^{-\xi_1/\gamma}, \quad \epsilon_d \sim p^{-\xi_2/\gamma} \quad (11)$$

and hence

$$\ell \sim p^{(3/2 \xi_1 - \xi_2)/\gamma}, \quad \mu_T \sim p^{(1 + 2\xi_1 - \xi_2)/\gamma} \quad (12)$$

The parameters ξ_1 and ξ_2 are constants determined by comparison with experiment. In the case to be presented, $\xi_1 = 2/3$ and $\xi_2 = 4/3$, but there is uncertainty at this time as to the values which yield best agreement with experimental data and further comparisons must be made. In calculating the turbulence along a streamline expanding into the wake, Finson^{II-5} also used $\xi_1 = 2/3$ and $\xi_2 = 4/3$, consistent with the analysis of Pirri.^{II-6}

The turbulence equations contain other constants which are intended to be "universal" and which have been determined by comparison of solutions with measurements from other turbulent flows. By balancing production with dissipation in the e -equation, the relation $\tau/\rho e = \sqrt{C_d}$ is obtained from which C_d can be evaluated from measured values of $\tau (= -\rho \overline{u'v'})$ and e in shear layers and boundary layers; the value $C_d = 0.09$ was thereby obtained.

The decay of isotropic grid turbulence provides the value of the second dissipation constant, C_2 . The balance between convection and dissipation at large R_T yields the relation $\ell \sim e^{3/2 - C_2}$. Comparison with data yields a compatible value of $C_2 = 1.89$.

The equations contain two constants of order unity, σ and σ^* , which are analogous to the inverse of the Prandtl number of thermal diffusion. The value of σ^* , appearing in the turbulent energy equation, does not strongly affect the solution for order one values and so a value of unity is used. However, the production constant C_1 and σ in the ϵ_d -equation cannot be specified independently if the theory is to properly reduce the velocity slope in the law-of-the-wall region of a flat plate incompressible boundary layer. Assuming that $\ell = C_d^{1/4} \kappa y$, and e is constant in this region, the relation $(C_1 - C_2)C_d^{1/2} = \sigma \kappa^2$ must be satisfied, where κ is the Von Karman constant. Calculations at TRW^{II-7} produced good agreement with experiments for $C_1 = 1.41$ and $\sigma = 0.77$.

The boundary conditions imposed on e and ϵ_d reflect the dampening effect of a smooth wall on the fluctuations, leading to the conditions $e(s,0) = \epsilon_d(s,0) = 0$. For wake flows, the symmetry condition on the axis is imposed, i.e., $\partial e / \partial \psi = 0$, $\partial \epsilon_d / \partial \psi = 0$ at $\psi = 0$ for all s .

The description of the turbulence modeling for the boundary layer and wake external to the recirculation region is completed by including turbulent as well as laminar diffusion in the mean flow momentum and energy equations. According to the eddy viscosity assumption of the present analysis, the diffusion flux terms for shear and heat transfer in Equations 8 and 10 are written as

$$\tau_L + \tau_t = \rho r^\alpha U \left(\mu + \mu_t \right) \frac{\partial U}{\partial \psi}$$

(13)

$$q_L + q_t = -\rho r^\alpha U \left(\frac{\mu}{Pr} + \frac{\mu_t}{Pr_t} \right) \frac{\partial h}{\partial \psi}$$

and

where the specific heat is assumed constant. In addition, the laminar viscosity is replaced with the sum $\mu + \mu_t$ in Equation 2.

The analysis of the turbulent near wake requires the formulation of an integral theory for the turbulent properties within the recirculation region consistent with the integral theory describing the mean flow. Thus, integral forms of the turbulent energy and dissipation rate equations were developed for the region from the axis to the matching streamline, and profiles of the turbulence variables were assumed. These equations are solved in conjunction with the outer flow turbulence equations in a manner analogous to that used for the mean flow. Details of the integral analysis for the turbulence properties are presented in Reference II-8

APPENDIX II REFERENCES

- II-1 Ohrenberger, J. T. and Baum, E., "A Theoretical Model of the Near Wake of a Slender Body in Supersonic Flow," AIAA Paper No. 70-792, presented at AIAA 3rd Fluid and Plasma Dynamics Conference, Los Angeles, Calif., June 1970; also, AIAA Journal, Vol. 10, No. 5, May 1972.
- II-2 Batchelor, G. K. and Townsend, A. A., "Decay of Turbulence in the Final Period," Proceedings of the Royal Society of Lond, Series A., Vol. 194, pp. 527-543, November 1948.
- II-3 Maise, G. and McDonald, H., "Mixing Length and Kinematic Eddy Viscosity in a Compressible Boundary Layer," AIAA Paper No. 67-199, presented at AIAA 5th Aerospace Sciences Meeting, 1967.
- II-4 Wilcox, D. C. and Alber, I. E., "A Turbulence Model for High Speed Flows," Heat Transfer and Fluid Mechanics Institute Proceedings, June 1972.
- II-5 Finson, M. L., "Hypersonic Wake Aerodynamics at High Reynolds Numbers," AIAA Journal, Vol. 11, No. 8, pp. 1137-1145, August 1973.
- II-6 Pirri, A. N., "Decay of Boundary-Layer Turbulence in Near Wake of a Slender Body," AIAA Journal, Vol. 10, No. 5, pp. 657-663, May 1972.
- II-7 Ohrenberger, J. T., and Baum, E., "Theoretical Modeling of the Base Flow Region of Supersonic Bodies: A Steady State Method," Published in Aerodynamics of Base Combustion, Vol. 40, Progress In Astronautics and Aeronautics, The MIT Press, 1976
- II-8 "ROPE Project Semi-Annual Technical Report," TRW Report No. 18586-6051-RU-00, July 1972.

APPENDIX III - COLLISION FREQUENCY ESTIMATES

The purpose of this appendix is to make available estimates of electron-neutral collision frequencies. This is a part of the task required to specify the electromagnetic properties of the ionized region in the recirculation region immediately behind the base of a given reentry vehicle. The results are to be used to calculate propagation of radio frequency signals through the recirculation region.

1. A Simple Equation of Motion for Electrons in a Weakly Ionized Gas

The equation of motion of an electron acted on by an electric field, E_x (in the x-direction), can be written down as follows based on a simple model

$$\dot{\bar{v}}_x + \nu \bar{v}_x = \frac{e}{m} E_x \quad (1)$$

In this equation \bar{v}_x is the average drift velocity, ν is the collision frequency, and e, m are charge and mass of an electron, respectively. The collision term is written down by analogy with the derivation of the dc conductivity of free electrons in a metal, as shown in Reference III-1. (In Reference III-1 the average drift velocity between collisions is written down as $\bar{v}_x = \frac{1}{2} a \tau$, where a is acceleration, τ is average collision time. Acceleration $a = \frac{e}{m} E_x$. Thus, $\bar{v}_x = \frac{1}{2} \frac{e}{m} E_x \tau$. The collision frequency $\nu = \frac{1}{\tau}$, so that we can write $\nu \bar{v}_x = \frac{1}{2} \frac{e}{m} E_x$, which accounts for the collision term in equation (1) (except for the factor of 2). The average collision time $\tau = \Lambda / \bar{V}$, where Λ is the mean free path, \bar{V} is the average random electron speed. Since $\Lambda = \frac{1}{NQ}$ where N is the particle density, Q the collision cross-section, ^{III-2} the collision frequency ν can be calculated from

$$\nu = NQ\bar{V}$$

If the gas is a mixture we find

$$\nu = \sum_i N_i Q_i \quad (2)$$

where the subscript i identifies a constituent of the mixture. If the electric field E_x is sinusoidal, a steady state solution of equation (1) can be obtained simply, viz,

$$\bar{v}_x = \frac{1}{\nu + j\omega} \frac{e}{m} E_x, \quad (3)$$

where ω is the radian frequency of the electric field. The electrical conductivity σ is obtained by comparing Ohm's Law, $J_x = \sigma E_x$ with $J_x = ne\bar{v}_x$ as follows (J_x is current density, n is electron density)

$$\sigma = \frac{ne^2}{m} \frac{1}{\nu + j\omega}, \quad (4)$$

where $j = \sqrt{-1}$.

This expression for radio-frequency conductivity (σ) is used to calculate the propagation of a signal of frequency $\omega/2\pi$ through the given plasma. Although the above formulas are "derived" heuristically they have been used extensively in the analysis of propagation through hypersonic ionized flow fields.

2. A Formal Equation of Motion for Electrons in a Weakly Ionized Gas

A far more rigorous equation of motion can be derived on the basis of the Boltzmann transfer equation. Following Margenau^{III-3}, Altshuler^{III-4} used that approach to derive the following equation of motion:

$$\frac{d\bar{v}_x}{dt} + N \int f(\bar{v}, t) v_x V Q_0(V) d\bar{v} = \frac{e}{m} E_x \quad (5)$$

In this equation $f(\bar{v}, t)$ is the electron distribution function, \bar{v} is the vector velocity, t is time, Q_0 is the elastic cross-section (inelastic collisions, e.g. ionizing collisions, are neglected). Altshuler points out that in the case of gaseous constituents for which $V \cdot Q(V) = \text{constant}$, Equation (5) is identical with the simple form of Equation (1) since $\bar{v}_x = \int f(\bar{v}, t) v_x d\bar{v}$. However, since the energy dependence of Q can assume many different forms the simple equation (1) cannot reliably be used in general.

Molmud^{III-5} considered a generalized form of the equation of motion, i.e. the Langevin equation

$$\dot{\bar{v}}_x + g\bar{v}_x = \frac{e}{m} E_x \quad (6)$$

In this equation the term $g\bar{v}_x$ represents the effects of the collisions between electrons and neutrals. Again on the basis of the Boltzmann transfer equation Molmud relates g to ν in certain limiting cases. His results are reproduced in Table I, where g is allowed to be complex, $g = g_r + jg_i$. (Molmud's nota-

Table I. Evaluation of g_r and g_i for the low- and high-pressure cases (from Molmud^{III-5})

Gas species	$\nu/\omega < 1$		$\nu/\omega > 1$		Form of average collision frequency*
	g_r	g_i	g_r	g_i	
Q/V constant, air, nitrogen	$(5/3)\nu(1+4.22\nu^2/\omega^2)$	$(10/9)(\nu^2/\omega) \times (1+5\nu^2/\omega^2)$	$\nu[1+4.57(\omega/\nu)^2]$	$2\omega[1-2.29(\omega/\nu)^2 + 4.57(\omega/\nu)^4]$	$\nu = (3Q/V)\rho K T/m$
Q constant, helium	$\frac{1}{2}\nu(1-0.22\nu^2/\omega^2)$	$0.18(\nu^2/\omega) \times (1+2.14\nu^2/\omega^2)$	$(3\pi\nu/8)(1+0.28\omega^2/\nu^2)$	$0.18\omega(1-7.5\omega^2/\nu^2)$	$\nu = 2\rho Q(2KT/\pi m)^{1/2}$
QV constant, Maxwellian gas	ν	0	ν	0	$\nu = \rho QV$
QV^2 constant, H_2O , NH_3 ; molecules with permanent electric dipole moments	$\frac{3}{2}\nu(1-0.18\nu^2/\omega^2)$	$0.079(\nu^2/\omega) \times (1+0.60\nu^2/\omega^2)$	$(3\pi\nu/16)(1+0.30\omega^2/\nu^2)$	$0.11\omega(1-7.1\omega^2/\nu^2)$	$\nu = 2QV^2\rho(m/2\pi KT)^{1/2}$

* ν is rigorously defined as follows: $\nu = f\rho Q(V)V/dv$, where ρ is the neutral particle density, $Q(V)$ is the cross section with its correct functional dependence on V , f is the normalized velocity distribution function (assumed Maxwell-Boltzmann) and integration is over all of velocity space.

tion differs from that used here only in the use of ρ for particle density.) It is seen that at low ν/ω (i.e. low pressures) for air the effective collision frequency g_r is:

$$g_r \sim \frac{5}{3} \nu.$$

At high collision frequencies $g_r \sim \nu$. At intermediate values of $\nu/\omega \sim 1$ it is not possible to relate g simply to ν .

3. Numerical Values of Collision Cross-Section and Collision Frequency

It is necessary to obtain numerical values for the parameters that determine collision frequency, so that the results of the fluid mechanical calculations can be translated into electrical properties. Before actually writing down the recommended formula it is desirable to list the constituents generally found in hypersonic flow fields. This list is to be followed by a history of collision frequency formulas.

Molecular Nitrogen and Oxygen. N_2 and O_2 are found in appreciable quantities up to their respective dissociation temperatures. In the case of the base flow region significant concentrations of N_2 are expected. O_2 is present to a lesser extent. The collision cross-sections for these two components are relatively well known (by measurement).

Atomic Nitrogen and Oxygen. At the relatively low energies corresponding to hypersonic flow field temperatures (say 0.5 ev) it is difficult to measure the collision cross-sections for atomic nitrogen and oxygen. Early values were obtained theoretically. More recently experimental results have become available. In the case of the recirculation region these two atomic species probably play a minor role, even though their cross-sections are relatively high.

Carbon Monoxide. Relatively large mole fractions of CO are expected in our case. The cross-sections of CO are also high relative to clean, undissociated air, so the presence of CO has a significant effect on collision frequency. The cross-section has been calculated theoretically well as measured experimentally.^{III-7}

Hydrocarbons. Hydrocarbons have not usually been considered in the electromagnetic propagation problem. In the case of the vehicle treated here, however, hydrocarbons are expected, since the boundary layer is actually burning. The presence of the hydrocarbons may have an important effect on the effective collision frequency. Experimental (or theoretical) values for collision frequency of hydrocarbons were not found in the literature consulted in the preparation of this appendix. Their effects are included here, however, in reporting effective collision frequencies determined on the basis of direct microwave measurements through wakes of ablative vehicles, or through seeded flames.

Water Vapor, Hydroxyl. H_2O and OH have large collision cross-sections at low temperatures (say, $T < 5000^\circ K$). In the case of OH only theoretical results are available. If significant amounts of H_2O or OH are found in the base flow region it may be necessary to modify the recommended final formula to take into account the presence of these two constituents.

4. Functional Form of Collision Frequency

It is found that many of the important constituents of high temperature air exhibit collision frequencies per molecule that are proportional to energy. When multiplied by particle density, which is proportional to p/T , the collision frequency becomes proportional only to pressure p . In the following table all entries are found to have this functional form.

5. History of Collision Frequency Formulas

The following table lists in simple form the formulas resulting from theoretical estimates or experimental measurements in historical sequence. Each entry is discussed briefly below.

Table II. Collision Frequency Formulas

Author(s)	Year	Formula	
		$\nu = (\text{approx.})$ (sec ⁻¹)	$g_r = (\text{measured, approx.})$ (sec ⁻¹)
Robinson ^{III-8}	1957	$10^{11} p^*$	
Shkarofsky, et al ^{III-9}	1961	$10^{11} p$	
Sutton, et al ^{III-10}	1970	$10^{11} p$	
Guthart & Graf ^{III-11}	1970		$9 \times 10^{11} p$
Phelps ^{III-7}	1972	$0.7 \times 10^{11} p$	
Baskett ^{III-12}	1974		$(1-10) \times 10^{11} p \rightarrow 3 \times 10^{11} p$

*The pressure p is measured in sea-level atmospheres.

Discussion of Table Entries

A. Robinson. It became clear when the thermodynamic properties of flow fields around ICBM reentry vehicles were calculated that atomic nitrogen and oxygen would play an important role in the calculation of transmission through the plasma sheath. L. B. Robinson therefore set out to calculate

theoretically the values of the collision cross-sections and their energy dependence. Based on Robinson's results and an equilibrium composition of the high temperature air in the plasma sheath, in which N_2 , N, and O played a dominant role, typical results ended up with the given functional dependence.

B. Shkarofsky, et al. Shkarofsky, Bachynski and Johnston reviewed available information on collision frequency for high temperature air. They discuss some of the refinements due to the use of the Boltzmann equation rather than the Langevin equation. Convenient summary graphs and tables are provided that list collision frequency as a function of electron energy, gas temperature and density. If the electrons are assumed to have average kinetic energy corresponding to the gas temperature, the listed formula results.

C. Sutton, et al. Sutton, Cohen and Textoris again reviewed available information on collision frequency up to 1970. Because of the linear dependence of collision frequency per molecule on energy for the major constituents, again the collision frequency is found to be proportional to pressure.

D. Guthart and Graf. In carefully conducted experiments Guthart and Graf measured the forward and backscattering cross-sections in a seeded flame. The theory used to analyze the data takes into account attenuation of the beam traversing the flame due to collisions. Collision frequencies were therefore deduced in such a way as to produce agreement between theory and experiment. It should be noted that this is an indirect measurement, and also, that the collision frequency results represent only one pressure (6 torr). The fact that the deduced collision frequency is higher than the previous formulas is presumably due to the presence of combustion products, whose cross-sections may be higher than those of clean, dry air constituents.

E. Phelps. In a recent review of electron collision frequencies and radio signal transmission through plasmas for DNA, Phelps provided detailed tables and graphs for each of the important gas species. Numerous references are given including references containing measured CO cross-sections. For dry air Phelps also obtains a formula in which ν is proportional to p , the proportionality constant being slightly lower than that of the previous

entries in the ν column. Phelps mentions that some experimental data obtained in the ionosphere suggest a 10-20% higher collision frequency than that listed.

F. Baskett. In developing a wake scattering model (similar to that of Guthart and Graf, above) to analyze ballistic range data, Baskett undertook another review of available collision frequency information, going back about 20 years. Making some judgment as to the quality and applicability of the information at hand, a set of "best" values was obtained.^{III-13} Baskett concluded that collision frequencies could be calculated by the formula $3 \times 10^{11} p$ with an uncertainty in either direction of a factor of 3. The value $3 \times 10^{11} p$ also matches recent experimental results in the ballistic range. In these experiments the complex transmission coefficient through an ionized portion of a wake was measured directly. Knowing also the electron density profile from independent measurements it is possible to deduce collision frequency. This is a considerably more direct method than that employed by Guthart and Graf discussed above. The range of $(1-10) \times 10^{11} p$ covers many different heatshields; one would therefore expect that the effects of a burning boundary layer would at least be partly covered in that range of values.

6. Recommended Formula

For reasons discussed below, Baskett's formula in Table I is recommended here for the present application, viz

$$\nu_{\text{eff.}} = 3 \times 10^{11} p_{(\text{atm.})} (\text{sec}^{-1}) \quad (7)$$

As mentioned above there is an estimated uncertainty of a factor of 3 in either direction in this collision frequency formula. The subscript "eff" is meant to indicate that this collision frequency is an effective value obtained from a "direct" microwave transmission measurement and thus accounts for possible differences between g and ν (see Section 2 in this Appendix).

7. Discussion

The recommended formula uses a larger proportionality constant than that shown by the majority of entries in Table II. There are several reasons for this choice. The principal reason is the presence of combustion products

in the plasma region of interest. Hydrocarbons are likely to have collision cross-sections that are higher than those of clean air constituents. Small amounts of undissociated water vapor and/or OH will raise the total effective cross-section noticeably (see Reference III-7). These statements are qualitatively consistent with the high value obtained in a flame by Guthart and Graf (Table II). (It should be noted that the Guthart and Graf result is within the band of uncertainty associated with Equation (7)). Last, Table I suggests that effective collision frequencies, g , are generally higher than the conventional collision frequency, ν .

It is necessary to determine the ratio ν/ω in order to use the information contained in Table I. A typical pressure in the present application is 0.05 atm. Thus the effective collision frequency, according to Equation (7) is 1.5×10^{10} per second. If the antenna in the base region operates near S-band, for example, say 2 GHz, $\omega = 4\pi \times 10^9 = 1.3 \times 10^{10}$. Thus $\nu/\omega = 1.2$. Reference III-5 points out that under these conditions, the imaginary part g_i of the collision parameter, cannot be neglected. Results derived from the simple Langevin equation are then not valid. Thus, if it is required to predict ν_{eff} more accurately than the formula of Equation (7), special numerical techniques may be necessary to determine the microwave propagation constants. On the other hand, at much lower or higher frequencies, where g_i can be neglected, a more accurate formula than Equation (7) may be provided by a detailed consideration of the constituents in the base flow region. It would be necessary to gather data on the energy-dependent cross sections of the various combustion products. If the overall velocity dependence of the collision cross section (in the neighborhood of the thermal energy) can be represented reasonably well by one of the forms given in Table I, then the information contained in that table can be used directly. For other functional forms it may be possible to use tables developed by Molmud^{III-14} for the calculation of g . It should be noted that a review of transmission of radio signals through plasmas with particular application to rocket exhausts is available in Reference III-15. Experimental determinations of collision frequency as reported in that reference appear to agree with equation (7).

APPENDIX III
REFERENCES

- III-1. N. H. Frank, "Introduction to Electricity and Optics," McGraw-Hill N.Y. 1940, p. 196.
- III-2. J. Millman and S. Seely, "Electronics", McGraw-Hill, N.Y. 1941.
- III-3. H. Margenau, Phys. Rev. 69, 508 (1946).
- III-4. S. Altshuler, "Electromagnetic Propagation in Ionized Media," Ramo-Wooldridge Corp., Memorandum, June 23, 1955.
- III-5. P. Molmud, Phys. Rev. 114, 29 (1959).
- III-6. S. Altshuler, Phys. Rev. 107, 114 (1957).
- III-7. A. V. Phelps, "Electron Collision Frequencies and Radio Frequency Absorption," Chapter 21 of Defense Nuclear Agency "Reaction Rate Handbook," Second Edition, DNA 1948H, March 1972.
- III-8. L. B. Robinson, Phys. Rev. 105, 922 (1957).
- III-9. I. P. Shkarofsky, M. P. Bachynski and T. W. Johnston, "Collision Frequency Associated with High Temperature Air and Scattering Cross-Sections of the Constituents," in W. Rotman and G. Meltz, Ed., "Electromagnetic Effects of Reentry," Pergamon Press, N.Y. 1961.
- III-10. E. Sutton, A. Cohn and A. Textoris, "Radar Scattering from Wakes When the Born Approximation Holds: Characterizing the Medium (U)," in "Proceedings of the Workshop on Radar Scattering from Turbulent Media," Cornell Aeronautical Laboratory Report, ARPA-T10, 71-3, July 16-17, 1970 (Secret).
- III-11. H. Guthart and K. A. Graf, Radio Science 5, No. 7, 1099 (1970).
- III-12. "Reentry Physics and Hypervelocity Measurements Program (U)," Semi-annual Report, Delco Electronics Report R74-47 (SB0-74-0179-S) May 1974 (Secret) p. 3-34.
- III-13. J. Baskett, Private Communication, 1976.
- III-14. P. Molmud, Phys. Fluids, 7, 150 (1964).
- III-15. S. Altshuler, M. M. Moe, P. Molmud, "The Electromagnetics of the Rocket Exhaust," Space Technology Laboratories Report GM-TR-0165-00397, June 15, 1958.

MISSION of Rome Air Development Center

RADC plans and conducts research, exploratory and advanced development programs in command, control, and communications (C³) activities, and in the C³ areas of information sciences and intelligence. The principal technical mission areas are communications, electromagnetic guidance and control, surveillance of ground and aerospace objects, intelligence data collection and handling, information system technology, ionospheric propagation, solid state sciences, microwave physics and electronic reliability, maintainability and compatibility.



Printed by
United States Air Force
Hanscom AFB, Mass. 01731